P
2mic4

132795

STELLAR FIGURE SENSOR

William N. Peters
The Perkin-Elmer Corporation
Norwalk, Connecticut 06852

April 1973
Final Report for January 1972 to January 1973

Prepared for

GODDARD SPACE FLIGHT CENTER

Greenbelt, Maryland 20771

1. Report No.	2. Government Accession No.	3. Recipient's Catalog No.

4. Title and Subtitle	5. Report Date
STELLAR FIGURE SENSOR	April 1973
	6. Performing Organization Code
7. Author(s)	8. Performing Organization Report No.
William N. Peters	11455
9. Performing Organization Name and Address	10. Work Unit No.
The Perkin-Elmer Corporation Norwalk, Connecticut 60852	11. Contract or Grant No. NAS 5-23067
	13. Type of Report and Period Covered
12. Sponsoring Agency Name and Address	Final Report Jan. 1972 - Jan. 1973
Goddard Space Flight Center Greenbelt, Maryland 20771	14. Sponsoring Agency Code

15. Supplementary Notes Major Contributors were:
R. Arnold, S. Gowrinathan, J. Ivaldi, D. Rosenzweig, E. Roberts of the Perkin-Elmer Corporation, and John Mangus of NASA/GSFC.

16. Abstract This document is a compilation of the analytical and experimental data generated during the period of performance of Contract NAS 5-23067 The contract had three major objectives. First, an analytical model was to be derived for an interferometric device which is located in the focal plane of an orbiting Large Space Telescope (LST). This device is to perform interferometry on the optical wavefront of a single star after it has propagated through the LST. The second objective was to experimentally verify the concept of focal plane figure sensors by fabricating and testing an operating laboratory breadboard The experimental data obtained from the breadboard verified the accuracy of the analytical model and demonstrated the utility of the Stellar Figure Sensor design. Finally, a conceptual design phase of the contract was to consider the systems engineering constraints which must be considered when the focal plane figure sensor "black box" is integrated into the LST. A series of linear independent control equations were derived which define the operations required for utilizing a focal plane figure sensor in the control loop for the secondary mirror position and possibly active control of the primary mirror.

17. Key Words (Selected by Author(s))	18. Distribution Statement
Interferometry Telescopes Astronomy Image Processing Space Optics Coherence Measurements	

19. Security Classif. (of this report)	20. Security Classif. (of this page)	21. No. of Pages	22. Price*
Unclassified	Unclassified	106	

*For sale by the Clearinghouse for Federal Scientific and Technical Information, Springfield, Virginia 22151.

PREFACE

This document is a compilation of the analytical and experimental data generated during the period of performance of Contract NAS 5-23067. The contract had three major objectives. First, an analytical model was to be derived for an interferometric device which is located in the focal plane of an orbiting Large Space Telescope (LST). This device is to perform interferometry on the optical wavefront of a single star after it has propagated through the LST. The second objective was to experimentally verify the concept of focal plane figure sensors by fabricating and testing an operating laboratory breadboard. The experimental data obtained from the breadboard verified the accuracy of the analytical model and demonstrated the utility of the Stellar Figure Sensor design. Finally, a conceptual design phase of the contract was to consider the systems engineering constraints which must be considered when the focal plane figure sensor "black box" is integrated into the LST. A series of linear independant control equations were derived which define the operations required for utilizing a focal plane figure sensor in the control loop for the secondary mirror position and possibly active control of the primary mirror. A number of scientific experiments which could be performed with the interferometer were also defined.

The contract was monitored and guided by John Mangus and Joseph Alonzo of NASA Goddard Space Flight Center, Greenbelt, Maryland.

TABLE OF CONTENTS

LIST OF ILLUSTRATIONS

LIST OF ILLUSTRATIONS (Continued)

LIST OF TABLES

SECTION I

INTRODUCTION

During the coming decade NASA will launch a large, orbiting stellar telescope into orbit. To insure maximum utilization of the telescope, the optical performance of the instrument must be essentially equal to the theoretical optimum. In order to be assured of this, several questions must be asked:

(1) Is the simulation of the zero gravity on earth during the testing of the primary mirror adequate?

(2) Is the accuracy of the auxiliary test optics used in fabricating the primary mirror adequate?

(3) Was the mirror stressed during launch?

(4) Are the primary and secondary mirrors of the telescope properly aligned once the instrument is in orbit?

If the questions cannot be answered positively and with confidence, it will be necessary to place some diagnostic instrumentation in the orbiting telescope to verify the performance of the telescope optical system.

Let us now consider the "coherent" sources that may be used in space to interferometrically test the telescope in situ. The first source that comes to mind is the laser. However, in addition to the reduced reliability of the space telescope interferometer resulting from the laser, we must consider that most of the common interferometric techniques are severely limited when applied to highly aspheric mirrors such as are presently contemplated for the orbiting telescopes.

Above the earth's perturbing atmosphere, a non-resolvable star source is also a perfect coherent source for performing interferometry. According to the Zernike-Van Cittert theory (ref. 1), any star that cannot be resolved by the telescope optics (which in practice includes almost all single star images),

will generate a wavefront that has near perfect coherence across the aperture of the telescope. Thus, the star source is an obvious choice if a method of performing interferometry on the resultant stellar image in the telescope focal plane can be devised. Performing interferometry on the stellar wavefront that has propagated through the telescope optical system has a number of distinct advantages:

(1) The interferometry is performed on an exact replica of the wavefront entering the respective instruments.

(2) The interferometer has an ultra-highly reliable light source (the star).

(3) The telescope operator has the potential capability of detecting both figure errors intrinsic to the individual optical elements (such as bending of the primary) and errors resulting from misalignment between the optical elements (such as defocus).

(4) We are indeed guaranteed that a plane wavefront is incident on the telescope pupil, thus permitting us to define perfect system focus.

With proper data processing, the interferometric data obtained from the stellar figure sensor can be utilized (1) to correct for secondary mirror misalignment; (2) possibly, to correct for primary mirror errors using the Active Optics techniques that have been perfected (ref. 2); (3) to diagnose the system performance; and (4) as a basis for post-exposure processing of the experimental data obtained from the telescope experiment packages. (See Figure 1.)

This report presents a design and analysis of an interferometer specifically designed to operate in or near the focal plane of an orbiting telescope and to use light from a stellar source. The device is an interferometer utilizing a high radial shear whose output is modulated in such a manner as to give a signal that is linearly related to the wavefront error over an extent of several wavelengths. The analytical model has been used to determine the ultimate sensitivity of the interferometer and to optimize the performance of the

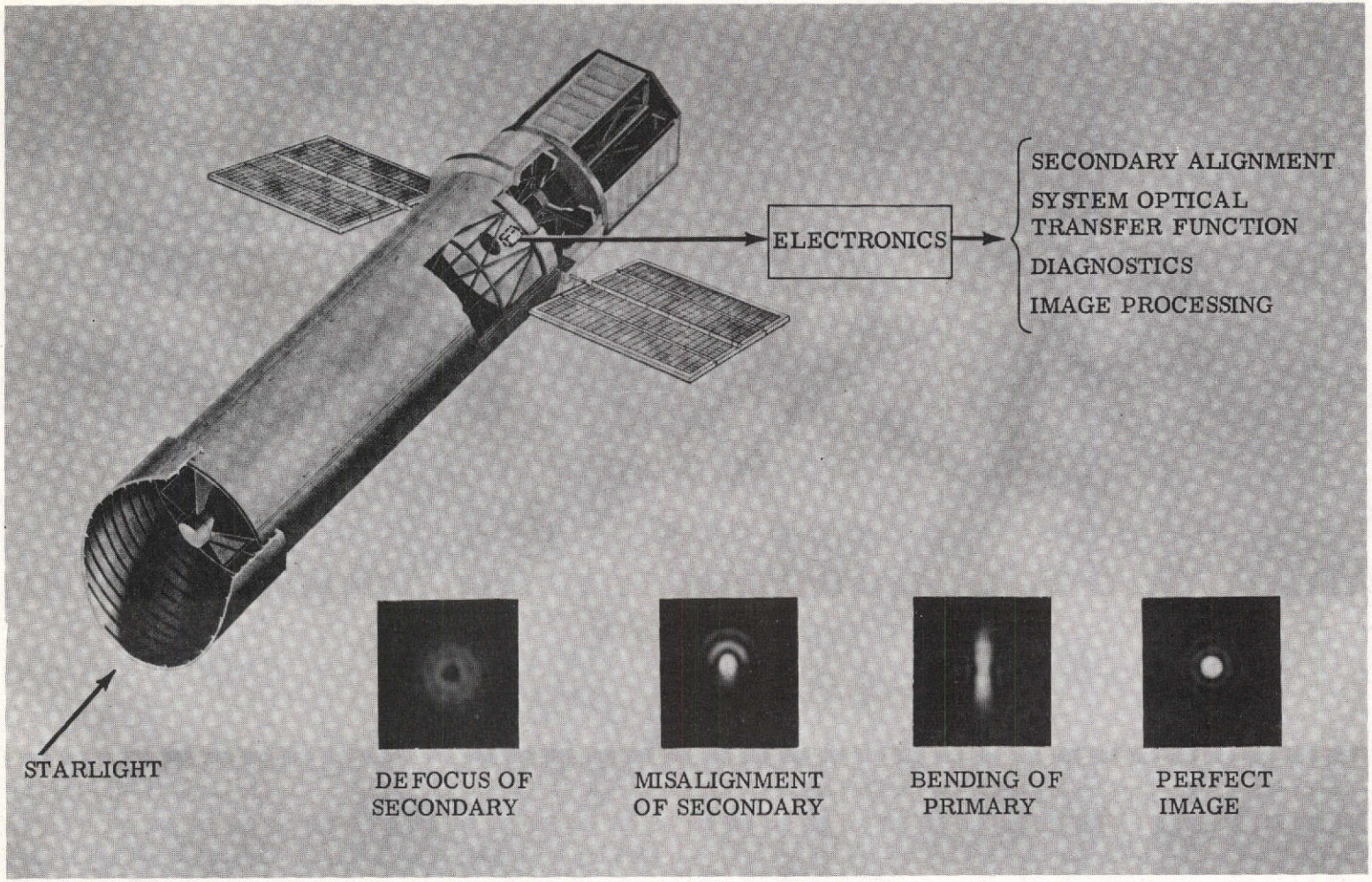

Figure 1. Stellar Figure Sensor Operating in LST Focal Plane

system by analytically determining the value of several parameters over which the optical designer has control. A laboratory breadboard of the interferometer was fabricated and the experimental results compared with the values predicted by the analytical model.

SECTION II

OPERATIONAL REQUIREMENTS OF A STELLAR FIGURE SENSOR

The functional requirements of a stellar figure sensor for an orbiting astronomical telescope are unique. The common laboratory or optical shop interferometer is designed under the constraint that it be sensitive to figure errors of a wide spectrum of spatial frequencies in the subject optical element (or more exactly, variations in the wavefront emanating from this element). Also, factors such as the illuminating source (usually a laser) and auxiliary test optics usually do not significantly limit the design of a laboratory interferometer. A review of the requirements for the figure sensor of an orbiting astronomical telescope reveals the opposite constraints. Namely, the figure errors induced into the telescope optical system will be primarily of low spatial frequencies and can be accounted for in large part by the Seidel aberrations. This relaxation of the operational requirements of the orbiting telescope figure sensor leads directly to the class of interferometers commonly referred to as shearing interferometers. These devices use a beamsplitter to divide the optical beam into two portions and introduce a physical displacement, change in scale, or reversal in one beam relative to the other before recombining the beams at a second beamsplitter to generate a fringe pattern. A typical example is the device built and analyzed by Bates (ref. 3). His interferometer placed a lateral shear in one of the beams before the recombination at the beamsplitter. Although very simple to implement, the data reduction of the resulting interferogram is difficult, thus limiting its use in applications that require data reduction in real time.

After consideration of the requirements placed on the figure sensor by the stellar source, weight limitations, and compatibility with the primary functions of the orbiting telescope, the design of the Stellar Figure Sensor* (SFS) evolved. An optical schematic of the SFS is given in Figure 2.

*Patent applied for.

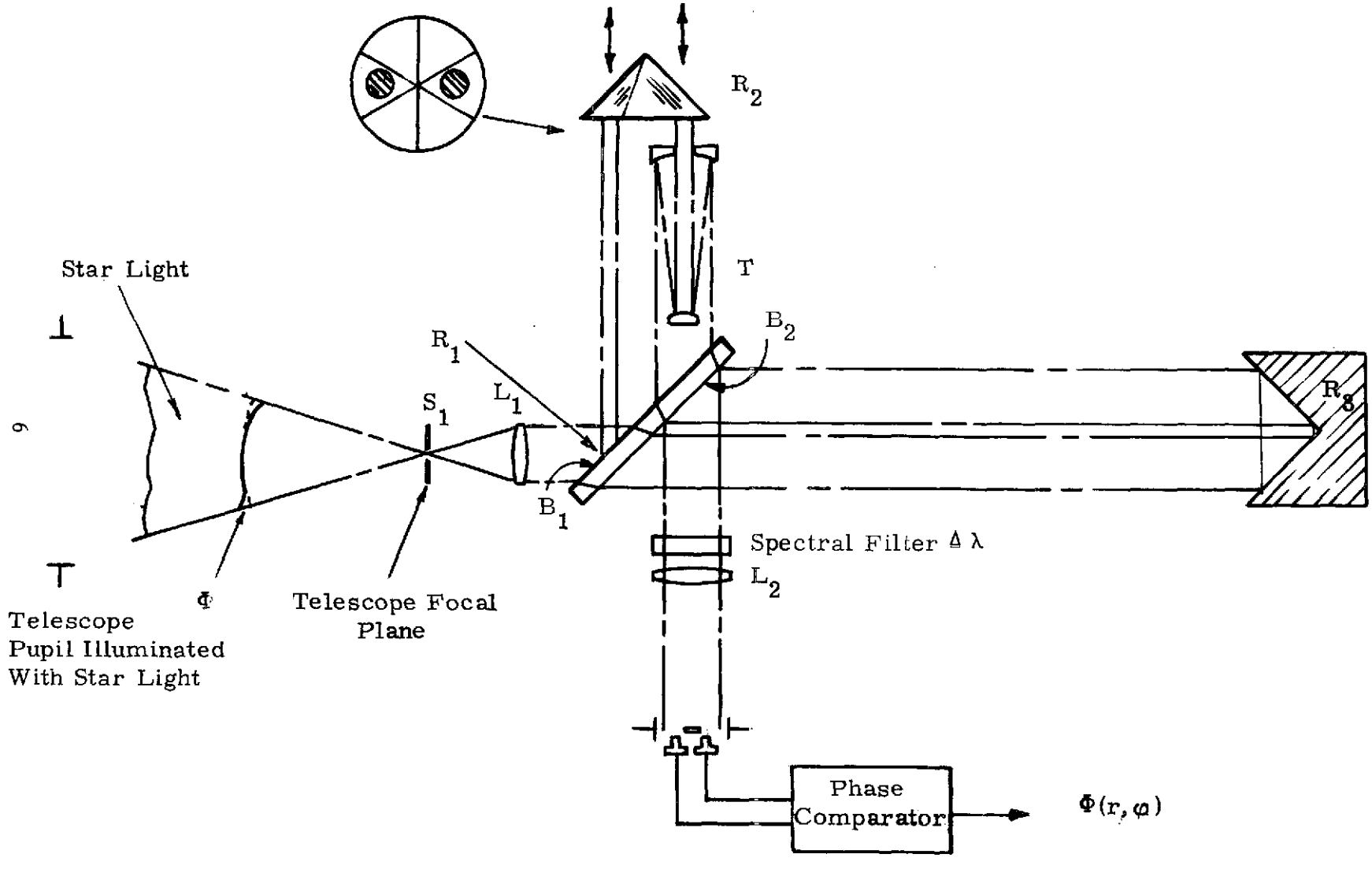

Figure 2. SFS Optical Schematic

It is assumed that the telescope entrance pupil is illuminated by starlight from an unresolvable star. A field stop, S_1, is placed in the telescope focal plane to eliminate light from other stars. The light from the source star is collimated by lens L_1. The relay telescope pupil (located behind the secondary in the Cassegrain telescope) is imaged at the front surface B_1 of the beamsplitter which has a reflective dot of diameter d located in an illuminated section of the pupil. (Note that in the Cassegrain form of telescope, the shadow of the secondary falls in the central zone of the relay pupil imaged at the beamsplitter.) Light reflected from the dot will become the reference wavefront for the interferometer. The maximum possible d is limited by the expected spatial frequency of the primary mirror figure errors and the minimum possible d is determined by photometry.

Two operations must be performed on the reference beam before it is recombined with the remaining beam, which we will subsequently refer to as the signal beam. First the reference beam must be modulated relative to the signal beam. This operation temporally encodes the photodetector electrical output signals. The placement of rotating quarter-wave plates in one arm of the interferometer or chirp modulation of the laser are techniques commonly used in laser illuminated interferometers. Unfortunately, these techniques do not have direct application to the SFS. The modulation technique chosen is to induce a frequency shift in the reference beam by utilizing the Doppler effect of a beam of light as it is reflected from a moving mirror. One of the problems in implementing such a device is that an inevitable (though possibly diminishingly small) tilt occurs as one translates a mirror. The SFS design replaced the commonly used plane mirror with an open trihedral cube corner (also known as hollow cube corner or triple mirror corner). Any tilt introduced by the drive mechanism is converted into a small lateral translation of the return beam with no change in the return angle. As will be discussed shortly, a small lateral translation of the reference beam does not affect the accuracy of the SFS. Care must be taken in white light interferometry to guarantee that the path length in glass is equal in both arms of the interferometer. Otherwise, the dispersion in the glass will significantly reduce the contrast of any resultant fringes. This is the motivation for using the open trihedral cube corner instead of the refractive prism corner cube.

The second operation that must be performed on the reference beam is the magnification of the beam such that it is of the same scale as the signal beam. This is performed by an all-reflective afocal telescope T. The telescope is of a conventional design using coaxial convex and concave parabolic elements. The angular magnification of a telescope, M, is (ref. 4)

$$M = \frac{\theta'}{\theta} = \frac{D}{d}$$

where θ' = Angular variation of afocal telescope input

θ = Angular variation of afocal telescope output

d = Reference beam diameter

D = Signal beam diameter.

Rotation of the afocal telescope about two orthogonal axes perpendicular to the telescope optic axis can correct interferometer misalignments resulting from wedge in the beamsplitter, angular fabrication errors in the retroreflector and Porro prism, or by a static error in the star trackers in the LST. If this correction is not made, the misalignments discussed above will introduce a tilt (i.e., straight line fringes) into the interferogram formed in the output of the SFS. This tilt term in the optical path difference map is easily deleted during the computer processing of the output data.

The signal beam is reflected and laterally displaced by a hollow Porro prism. Ideally, a corner cube should be used for this operation. However, the physical separation between the two beams in the signal arm of the interferometer would be excessive if the corner cube were to be illuminated as shown in the insert of Figure 2. This in turn would significantly increase the size of the SFS. The return beam from a hollow Porro is sensitive to rotational errors of the prism in only one axis. Thus, special care must be exercised in the design of the mount for the Porro prism in this degree of freedom. (In Figure 2 this rotational axis is vertical and in the plane of the paper.)

The reference and signal beams are recombined by a semitransparent metallic coating on the beamsplitter surface B_2. The optimum transmission of this beamsplitter is calculated in Section III. Note that both the signal and reference beams traverse the beamsplitter only once, thus eliminating the

requirement for compensating plates such as used in the Michelson interferometer (ref.5). If optical dispersion is to be compensated over a wide spectral range, the wedge of the beamsplitter must be accurately controlled.

Lens L_2 forms an image of the primary mirror in the plane containing the photodetectors. One of these detectors views a predefined portion of the primary, and the wavefront reflected from this area is arbitrarily chosen to be the reference. The signal emanating from every other point in the wavefront exiting the telescope is compared with the signal from the reference area by the phase comparator electronics. The difference in phase between the two signals is identically equal to pertuberations in the star wavefront as it traverses the telescope. This simple relationship between the detected signal and optical wavefront aberrations more than compensates for what may be considered the complexity of the optical system.

SECTION III

MATHEMATICAL MODEL

A signal flow diagram which is used as the basis of the mathematical model for the SFS is shown in Figure 3. All parameters required for the derivation are also defined. The numerator in the equation of Figure 3 is the term that reflects the signal power in the detection process utilized in the SFS. The first of three terms in the summation of the denominator reflects the signal shot noise. Since it is impossible to reduce the effect of signal shot noise by any technique other than by increasing the signal power, this term will be used in defining the ultimate sensitivity of the SFS. The second term in the denominator reflects the system degradation by unwanted background radiation (which could also include unwanted reflections and scatter from the true signal optical beams) and photodetector dark current as measured at the cathode in a photomultiplier. Proper design of the optical system including the insertion of field stops in the telescope focal plane should minimize the effect of stray light in the system. The dark current is controlled with the proper choice of photodetector and possibly cooling the photodetector, if required. The third term in the denominator reflects the thermal (Johnson) noise of the load resistor (ref. 6). The most common technique for minimizing the effect of this noise source is to increase the signal current above that which is generated by the load resistor.

The remaining, and sometimes very troublesome, noise source is mechanical vibration or air turbulence in the optical arms of the interferometer. This noise source has the effect of introducing a spurious modulation on the output of the photodetector in addition to the signal waveform resulting from the temporally modulated interferogram. This type of noise is very difficult to model since it usually has a relatively narrow spectrum and affects the system in different ways depending on where it is inserted. Good optical

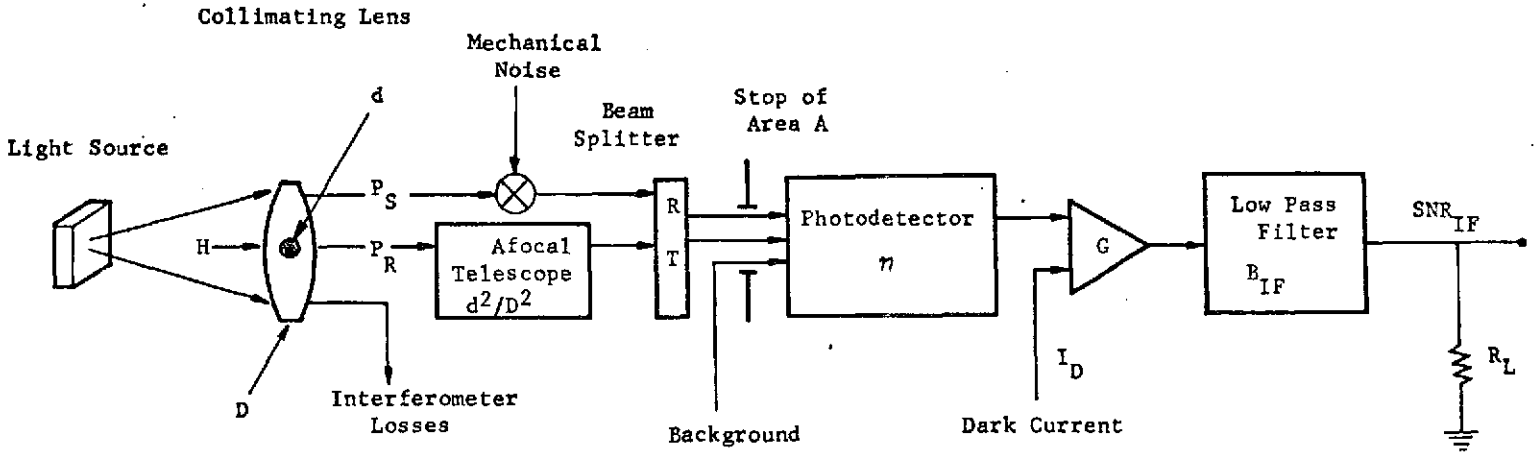

$$SNR_{IF} = \frac{\left[\frac{G\eta q\lambda}{hc}\right]^2 H^2 A^2 \frac{d^2}{D^2} TR\,\Gamma^2}{\frac{G^2 q B_{IF} \eta q H A \lambda}{hc}\left(R + \frac{d^2}{D^2}T\right) + G^2 q B_{IF}\left(\frac{4A}{\pi D^2}\frac{\eta q P_B \lambda}{hc} + I_D\right) + 2kT_R B_{IF}/R_L}$$

H = Irradiance (Watts/m^2)

d = Diameter of reference beam reflective dot viewed in object space (m)

D = Telescope pupil diameter (m)

P_S = Power in interferometer signal beam (watts)

P_R = Power in interferometer reference beam (watts)

R = Reflectance of beamsplitter

T = Transmission of beamsplitter

k = Boltzman's Constant

T_R = Temperature of load resistor (°K)

A = Area of stop preceding photodetector as viewed in object space

η = Photodetector quantum efficiency

G = Internal gain of photomultiplier

I_D = Cathode dark current

B_{IF} = Intermediate frequency zonal low pass filter bandwidth

R_L = Load resistor

q = Charge of electron (1.6×10^{-19})

h = Planck's constant (6.625×10^{-34})

c = Speed of light (3×10^8)

λ = Optical wavelength (m)

Γ = Coherence Function

Figure 3. Flow Diagram for the SFS

design engineering practices are usually sufficient to reduce this noise source to an acceptable level. A test program on the SFS breadboard experimentally determined the sensitivity of the interferometer to induced vibrations and the results indicated that mechanically induced errors were acceptably small.

The procedure for the rigorous derivation of the signal-to-noise equation will now be presented. The intensity of the wavefront exiting the telescope is

$$I = \left| A e^{i\Phi(x,y)} \right|^2 \tag{1}$$

where Φ = aberration function and it is assumed that the wavefront intersected by the telescope entrance pupil has a uniform intensity distribution (i.e., A = constant).

The reflective dot spatially divides the wavefront into two components, the reflected reference beam of intensity

$$I_R = \left| A_R e^{i\Phi(x,y)} \right|^2 \quad \text{over area of reflective dot} \tag{2}$$

$$= 0 \quad \text{elsewhere}$$

and the remaining signal beam

$$I_S = \left| A_S e^{i\Phi(x,y)} \right|^2 \quad \text{over pupil} \tag{3}$$

$$= 0 \quad \text{in reflective dot shadow, central obscuration}$$

As shown in Figure 2, the reference beam is operated upon by the afocal telescope of magnification M = D/d and the piezoelectrically driven retroflector which has a translation velocity of $\dot{L}_p$. Assuming that the center of the reflective dot is located at a point of coordinates Δx, Δy, and the total path length through the reference is L_R, the field from a single spectral line component of the composite white light reference beam immediately after being recombined with the other beam at the beamsplitter is

$$E_1(x,y) = \frac{A_R}{M} \sqrt{T} \exp\left[i\left\{ \omega t + \Phi\left[-M(x-\Delta x), -M(y-\Delta y) \right] + k(L_R + 2\dot{L}_p t) \right\} \right] \tag{4}$$

where
- T = Power transmittance of beamsplitter
- $\omega = 2\pi C/\lambda$
- C = Speed of light
- λ = Wavelength of light
- $k = 2\pi/\lambda$

The factor (-M) in the argument of Φ results from the magnification of the afocal telescope plus the reverse of the coordinate system that results as the reference beam propagates through the corner cube. The factor of 2 preceeding the piezoelectric drive retroreflector term $\dot{L}_p$ is calculated from the generalized Doppler shift equation (ref. 7) under the condition $\dot{L}_p \ll C$. Combining the first and last terms of the exponential argument, note that the piezoelectric drive retroreflector has effectively shifted the reference beam from frequency ω to frequency $\omega + 2k\dot{L}_p$.

If the xy coordinate system is chosen such that the x axis is parallel to the "roof line" of the Porro prism, the field of the signal beam reflected from the beamsplitter is

$$E_2(x,y) = A_S \sqrt{R} \exp\left[i\left\{\omega t + \Phi\ (x,-y) + k\ L_S\right\}\right] \tag{5}$$

where R = power reflectance of beamsplitter.

Coherently combining the monochromatic components of the reference and signal beams at the beamsplitter, the intensity distribution at a given point (x,y) is

$$I = \left|E_1(x,y) + E_2(x,y)\right|^2 \tag{6}$$

$$= \left|E_1(x,y)\right|^2 + \left|E_2(x,y)\right|^2 + 2E_1E_2 \cos\phi\ (x,y,t) \tag{7}$$

where
$$\phi\ (x,y,t) = \omega t + \Phi\left[-M(x-\Delta x),\ -M(y-\Delta y)\right] + k(L_R + 2\ \dot{L}_P t) - \omega t - \Phi\ (x,-y) - kL_S$$

As shown rigorously later in this section, a sufficiently large value of M forces the reference wavefront to be effectively plane (i.e., $\Phi[-M(x-\Delta x), -M(y-\Delta y)] \cong$ constant). The form of the phase term ϕ above is thus significantly simplified to

$$\phi(x,y,t) \simeq \Phi\ (x,-y) + 2k\ \dot{L}_P t + \text{unknown, but constant phase term for all x,y.} \tag{8}$$

By choosing some point x_o, y_o in the output pupil as our reference, we can disregard the unknown phase term by comparing all points in the pupil with one (arbitrarily chosen) reference point in the pupil. Since we know the value of k (effective wave number set by the system spectral response) it is easy to generate an OPD map of the wavefront aberration by the use of a simple phase comparator which operates on the outputs of two photodetectors, the reference being at x_o, y_o and the other unit at position x,y. Mathematically,

$$\Phi\ (x,-y) \;=\; \phi\ (x,y,t) \;-\; \phi\ (x_o,y_o,t). \tag{9}$$

Equation (7) is also revealing in that it states there is a constant bias current from the photodetectors in addition to the temporal signal. It is the photon shot noise of this current that we shall show is the ultimate limiting factor in any stellar interferometry.

The previously stated assumptions of coherence and spectral purity will be qualified for the conditions expected in the Stellar Figure Sensor. A rigorous derivation of the completely general model for partial coherence has been deferred, and special cases of the theory are presented as required. The measure of coherence (equivalent to the visibility of SFS fringe pattern) is affected by the optical bandwidth of the signal and the resolvability of the source by the relay optics. Although these two parameters are not strictly independent, we shall discuss each parameter separately for simplicity.

Under the assumption that $|E_1(x,y)|^2 = |E_2(x,y)|^2$, and that the light is suitably spatial coherent,* a rigorous derivation, similar to that which generated Equation (7) for polychromatic light, yields

$$I \;=\; |E_1(x,y)|^2 + |E_2(x,y)|^2 + 2E_1E_2\ \Gamma(\Delta L)\ \cos\left[\phi\ (x,y,t)\right] \tag{7a}$$

where $\Gamma(\Delta L)$ is the temporal coherence function.

The coherence function is dependent on both the spectral properties of the light and the path difference between the two arms of the interferometer, ΔL. To demonstrate this effect, $\Gamma(\Delta L)$ is plotted for several cases under

*This condition is met by nearly all stellar sources. However, this is a significant constraint on the choice of pinhole size for the laboratory simulation experiments.

the assumption that the interferometer is illuminated by spatially coherent light from a 3300°K blackbody source (typically a quartz halogen lamp) and that an RCA 31034 phototube is used as the detector. (See Figure 4.) This case was chosen since it corresponds to the laboratory simulation of the SFS. Note that, in Figure 5, in general, the temporal coherence is reduced as the optical bandwidth is increased. Thus, we see that we are faced with a very real trade-off: What is the largest bandwidth (and subsequently, largest detected power) we can use before the reduction of temporal coherence becomes excessive?

It is also interesting to note the situation in which either a very wide bandwidth (150nm) or no bandpass filter is used in a system having the spectral response of Figure 4. Obviously, this is the case for the maximum optical system throughput. Figure 6 shows the temporal form of the electronic waveform at the output of the photodetector as the corner cube is translated at a given constant velocity $L_p^{\cdot}$. Thus we are presented with an alternate detection technique — the measurement of the time delay between the pulses obtained from the two photodetectors — which is linearly related to the OPD of the wavefront. The optimum method for detecting this type of signal from both analytical and implementation considerations will probably be some variant of the pulse detection or cross correlation techniques commonly used in radar and communictaions.

The coherence function is also degraded by the "resolvability" of the light source by the optical system. The spatial coherence is a critical parameter in the design of the SFS since the magnification of the afocal telescope introduces shears on the order of half the pupil diameter between the reference and signal beams in the interferometer when the reference reflective dot is located in the center of the pupil. Nearly all stellar sources have a sufficiently small angular subtense to be spatially coherent across the entire telescope pupil. However, laboratory experiments utilizing a pinhole illuminated by a blackbody source require that for a spatial coherence of $\Gamma = 0.88$, the angular subtense of the pinhole as viewed through the lens L_1 (Figure 2) be

$$\theta = 0.64\lambda/D_1 \tag{10}$$

where D_1 is the diameter of lens L_1 (ref 1, page 511)

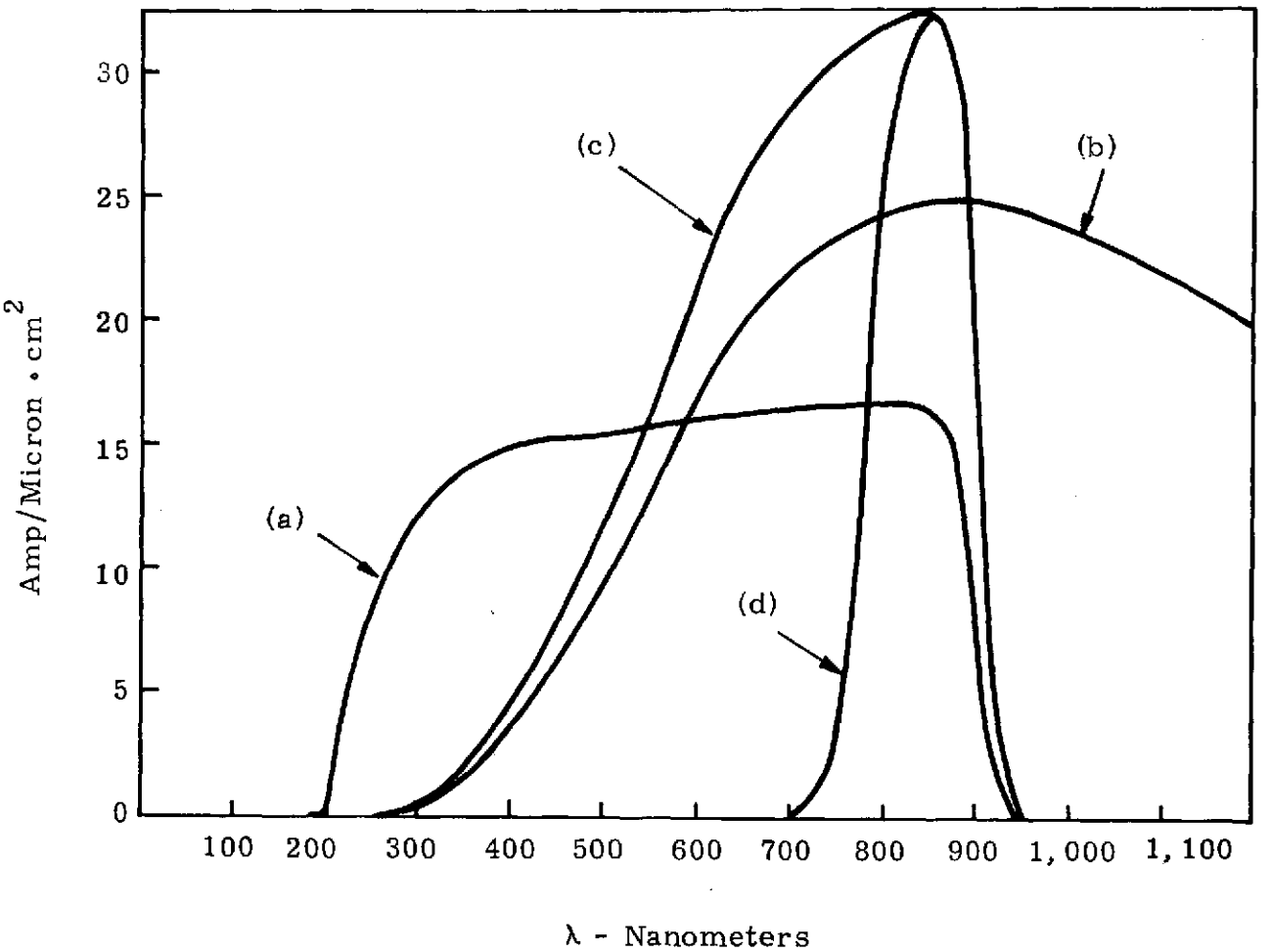

(a) Is The Spectral Response of the RCA 31034 Phototube. (b) Is the Spectral Emittance of a 3300°K Thermal Source (c) is the Spectral Response of the SFS Breadboard Operating in a "White Light" mode and (d) is the SFS Response with a Schott RG 780 Filter in the Optical System.

Figure 4. Spectral Response of the Laboratory Breadboard

Figure 5. Fringe Contrast as a Function of Number of Fringes From Zero Order Fringe for Various Optical Bandwidths

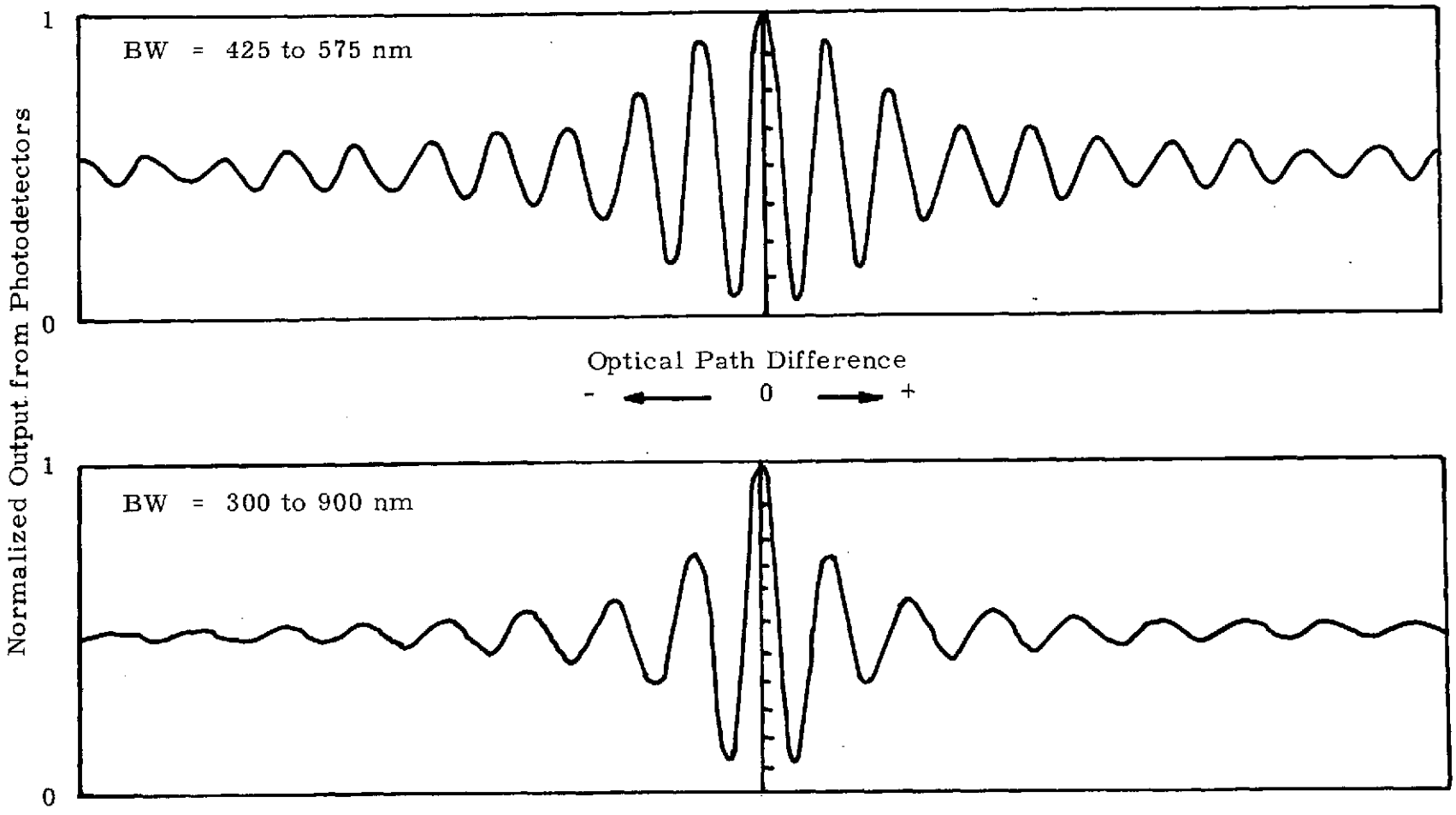

Figure 6. Effect of Spectral Bandwidth on Output Optical Waveform

We are now in a position to qualify Equation (7a) to include both temporal and spatial coherence effects by defining the coherence function Γ to be

$$\Gamma = \Gamma(\Delta L)\, \Gamma(D) \tag{11}$$

The above definition is not rigorously true since the two coherence functions are not independent. However, the definition will suffice for the purposes of this section.

The intensity incident on the phototube is thus

$$I = |E_1(x,y)|^2 + |E_2(x,y)|^2 + 2E_1E_2\, \Gamma \cos\left[\phi\,(x,y,t)\right] \tag{7b}$$

Referring to the flow diagram in Figure 3, the third term of Equation (7b) is converted to a signal current I_S by the phototube of quantum efficiency η and internal gain G.

$$I_S = \frac{G\eta q\lambda}{hc}\, 2E_1E_2\, \Gamma \cos\left[\phi\,(x,y,t)\right] \tag{12}$$

The first two terms of Equation (7b) produce a dc current which contributes nothing to the signal, but generates a shot noise power which can be derived from the Schottky formula to be

$$N_S = \frac{2qG^2\eta\lambda}{hc}\, B_{IF} \left\{|E_1(x,y)|^2 + |E_2(x,y)|^2\right\} R_L \tag{13}$$

In a similar procedure, the shot noise resulting from a uniform background of P_B illuminating the entire pupil plane is

$$N_B = \frac{2qG^2\eta\lambda B_{IF}}{hc}\, \frac{4A}{\pi D^2}\, P_B\, R_L \tag{14}$$

where $\frac{4A}{\pi D^2}$ = portion of pupil plane of diameter D viewed by detector of area A.

The shot noise resulting from the dark current is

$$N_D = 2qG^2 B_{IF}\, I_D\, R_L \tag{15}$$

The last source of noise considered in the model is the thermal noise in the load resistor R_L,

$$N_L = 4KTB_{IF} \tag{16}$$

Thus, the power signal-to-noise ratio is determined by calculating the signal and noise powers as measured across a load resistor of R_L as follows

$$SNR_{IF} = \frac{\langle I_S^2 \rangle R_L}{N_S + N_B + N_D + N_L} \tag{17}$$

where the brackets denote a time average. The amplitude of the field in the two arms of the interferometer is related to the irradiance H at the telescope entrance pupil (usually the primary mirror) from either the star or pinhole. Also, the detectors must spatially sample the exit pupil in order to generate the data points for the OPD map. If the detector views an area of A of the exit pupil as viewed in object space, the relationship between the optical electric fields A_R and A_S and the incident light flux is given by

$$|A_R|^2 = |A_S|^2 = HA\,\tau_{OPT} \tag{18}$$

where τ_{OPT} = optical transmission of optics

An algebraically tedious, but straightforward substitution of Equations (7), (8), (14), (15), (16), (18), (9) and (5) into Equation (17) results in the signal-to-noise equation as given in Figure 3.

An estimate of the ultimate sensitivity of the SFS to a given rms wavefront error is obtained by the following limiting case for the measurement of phase in white Gaussian noise (which incidentally results from all the noise sources of Equation (17)), rms phase error = $\frac{1}{2(SNR)}$. This is the phase error resulting from the comparison of a noisy signal with its noise-free basis. However, the SFS obtains the detected phase error by the comparison between two noisy signals. Assuming that the errors add on an rms basis, the rms phase error = $\frac{\sqrt{2}}{2(SNR)}$.

Remembering that a figure error of 1λ generates a phase error of 4π in the SFS, the ultimate performance capability of the SFS is

$$\Delta\lambda_{rms} = \frac{\sqrt{2}\lambda}{8\pi\ (SNR)} \tag{19}$$

For analytical purposes, the parameters of the SNR equation are redefined as follows

$$SNR_{IF} = \frac{K_1 \frac{d^2}{D^2}\ T\ R}{K_2\left(R+\frac{d^2}{D^2}\ T\right)+K_3} \tag{20}$$

where $$K_1 = \left[\frac{G\eta q\lambda HA\Gamma}{hc}\right]^{-2}$$

$$K_2 = \frac{G^2 q\ B_{IF}\ \eta qHA\lambda}{hc}$$

$$K_3 = G^2 q\ B_{IF}\left(\frac{4\ A\ \eta q\ P_B\ \lambda}{\pi D^2\ hc} + I_D\right) + 2KT_R\ B_{IF}/R_L$$

The parameters over which the optical designer has latitude in specifying are T, the transmission of the beamsplitting surface; R, the reflectivity of the beamsplitting surface; and d, the reference spot size. However, T and R are functionally related.

The relationship between T and R, representing the transmission and reflection of the beamsplitter B_2 in Figure 2, can be expressed mathematically for many possible models. To assist in selecting an appropriate model, experimental data was obtained from available samples of beamsplitter coatings. It is observed that an Inconel beamsplitter coating of the type selected for use in the SFS has a significant absorption coefficient in addition to the transmission and reflection coefficients. In practice, the transmission coefficient for the coating can be made any value between zero and one, while the reflectivity can be made to vary only between zero and some maximum value less than one. A linear functional relationship was approximated for the reflectivity and transmission as follows:

$$R = R_o(1-T),\ 0 \leq T \leq 1,\ 0 \leq R_o < 1 \qquad (21)$$

With this model, R will be zero when T equals one and R_o when T equals zero.

Substituting the relation between R and T into the above SNR equation yields (Figure 7):

$$SNR_{IF} = \frac{K_1 \frac{d^2}{D^2}\ T\ (1-T)\ R_o}{K_2\left[R_o(1-T) + \frac{d^2}{D^2}\ T + K_3\right]} \qquad (22)$$

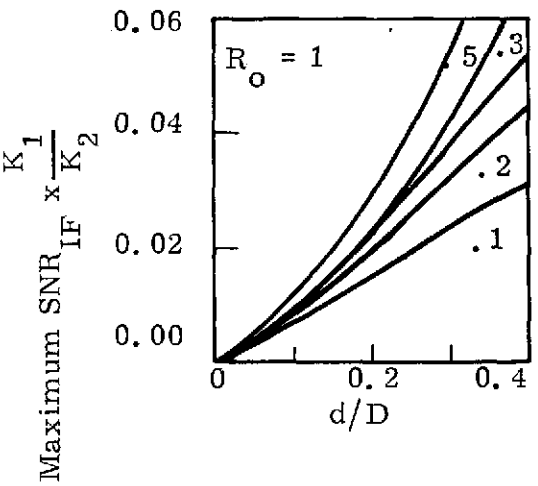

Figure 7. Maximum SNR as a Function of Normalized Reference Dot Diameter and Beamsplitter Parameters R_o for Signal Shot Noise Limited Operation

In this equation the two variable parameters are d/D and T. To determine the optimum value of T as a function of d/D in terms of maximizing the SNR, the following procedure was followed:

$$\frac{d\ SNR_{IF}}{dT} = \left(R_o - \frac{d^2}{D^2}\right) T^2 + \left(-2\ R_o - 2\ \frac{K_3}{K_2}\right) T + R_o + \frac{K_3}{K_2} = 0$$

The solution of this quadratic equation yields for the optimum transmission of the beamsplitter:

$$T_{Max\ SNR} = \frac{R_o + \frac{K_3}{K_2} - \sqrt{\left(R_o + \frac{K_3}{K_2}\right)\left(\frac{d^2}{D^2} + \frac{K_3}{K_2}\right)}}{R_o - \frac{d^2}{D^2}} \qquad (23)$$

Note that this optimum value is a function of the expected background radiation, photodetector dark current, and Johnson noise. A significant simplification results if we assume that the background, dark current, and Johnson noise components are negligible. Substituting $K_3 = 0$, the optimum beamsplitter transmission for signal-shot-noise-limited operation becomes a simple relation,

$$T = \left(1 + \frac{d}{D}\ \frac{1}{\sqrt{R_o}}\right)^{-1} \qquad (24)$$

Resubstituting this value for T into the SNR and plotting the result, we obtain the relationship between the SNR and the reference dot to signal beam diameter ratio (Figure 7). It is anticipated that a value for d will range between 0.2 D and 0.35 D for presently considered systems. Large values of d are not desirable since the reference wavefront becomes increasingly aberrated and the obscuration caused by the reference reflective dot becomes unacceptably large.

It is interesting to note that the condition for maximum SNR does not occur when we have maximum fringe contrast. The maximum fringe contrast occurs when the two beams incident on the photodetector have equal-intensity,

$$P_o = P_c \qquad (25)$$

which infers that

$$HA\ \left(\frac{d}{D}\right)^2 T = HAR \quad (R_o = 1\ \text{assumed}) \qquad (26)$$

$$T = \left(1 + \frac{d^2}{D^2}\right)^{-1}$$

The SFS uses a greatly magnified portion of the subject wavefront as the reference. We will now examine the sources of wavefront error in this reference beam and estimate their effect on the system performance. The reference wavefront contains errors resulting from (1) residual errors in the figuring of the primary/secondary mirrors, (2) errors intrinsic to the design of the telescope, (3) errors resulting from misalignment of the telescope optics, and (4) possibly residual errors from the Active Optics correction of the primary mirror.

From all present indications, the residual figuring errors of the LST should be sufficiently small — on the order of $\lambda/50$ rms. Any errors that do occur will probably result from errors in the zero gravity simulation of the primary and thus will occur as astigmatism or spherical aberration. As we shall see shortly, these lower order Seidel aberrations do not greatly influence the operation of the SFS. Likewise, the design errors in the system will be diminishingly small over the fine fields presently being considered for LST. As previously discussed, the errors resulting from misalignment are predominantly coma, astigmatism, and defocus. The effect of these Seidel aberrations on the purity of the reference wavefront will now be analyzed.

As shown by Equation (7), the numerical value of the phase as detected by the electronic phase detector is related in the following manner

$$\phi(x,y,t) = \Phi(x,-y) - \Phi(-Mx,-My) \tag{27}$$

when, for simplicity, it is assumed that the reference dot on the beamsplitter is placed in the center of the pupil.

The error in system performance resulting from the aberration component in the reference beam can be calculated by inserting each of the Seidel aberrations into Equation (27) and noting the resulting error terms. The general aberration equation is written in the form

$$\Phi = \sum_{n,m} A_{nm} \rho^n \cos^m (\theta + \Xi) \tag{28}$$

where Ξ = orientation of aberration relative to SFS coordinate system

A_{nm} = magnitude of introduced aberration in waves, λ.

Substitution of Equation (28) into Equation (27) indicates that, in general, the detected magnitude of the aberration is changed by a factor $1+M^{-n}$ with the possibility of additional aberrations of a much smaller magnitude being introduced. Table I gives the detected wavefront error as compared to the input wavefront error for several important aberrations. These errors should not be considered as a serious limitation to the SFS for several reasons. First, the typical value of M will be 3 to 5, thus reducing the incremental error of the term $1+M^{-n}$. Second, the calculated error factors allow for a proper weighting of the coefficients in any subsequent mathematical operations. Lastly, the entire optical system using an SFS has the property of "boot strapping" itself to a properly aligned system. That is, as the sources for wavefront error are corrected in the optical system, the quality of the reference beam in the interferometer is subsequently improved. This allows for the perfect alignment of the optical system if several iterations are allowed in the alignment sequence.

Note that the residual aberrations of Table I are of a form that the error may be reduced by properly orienting the SFS relative to the axes of symmetry for the aberrations. In the case of aberrations intrinsic to the design of the telescope, this is always possible by orienting the roof prism intersection parallel to the diameter of the field (i.e., $\Xi = 0$). If some other error source predominates and the angular orientation of this error source is known a priori, some other value of Ξ may be optimum.

One final potential error source will be discussed. In an effort to maximize the detected energy, the detector acceptance aperture A is typically chosen to be a significant portion of the entire pupil. Thus, the system is not interrogating a point in the pupil, but rather is taking an ensemble average of a number of points around the position ρ, θ (Figure 8). Thus the relative phase of the signal output is

TABLE I. ANALYSIS OF OUTPUT INTERFEROGRAM WHEN THE INPUT ABERRATION IS $A_{nm}\,\rho^n \cos^m(\theta + \Xi)$

Input Aberration	n	m	SFS Detection Coefficient of Input Aberration	Additional Aberrations
X-coma	3	1	$A_{31}\,(1+M^{-3})\cos\Xi$	$-A_{31}(1-M^{-3})\,\rho^3 \sin\theta \sin\Xi$ (y-coma)
Defocus	2	0	$A_{20}\,(1+M^{-2})$	
Spherical	4	0	$A_{40}\,(1+M^{-4})$	
X-astigmatism	2	2	$A_{22}\,(1+M^{-2})\cos^2(\theta+\Xi)$	$\frac{\rho^2}{M^2}\sin 2\theta \sin 2\Xi$
Tilt	1	1	$A_{11}\,(1+M^{-1})\cos\Xi$	$-A_{11}(1-M^{-1})\sin\theta \sin\Xi$ (y-tilt)

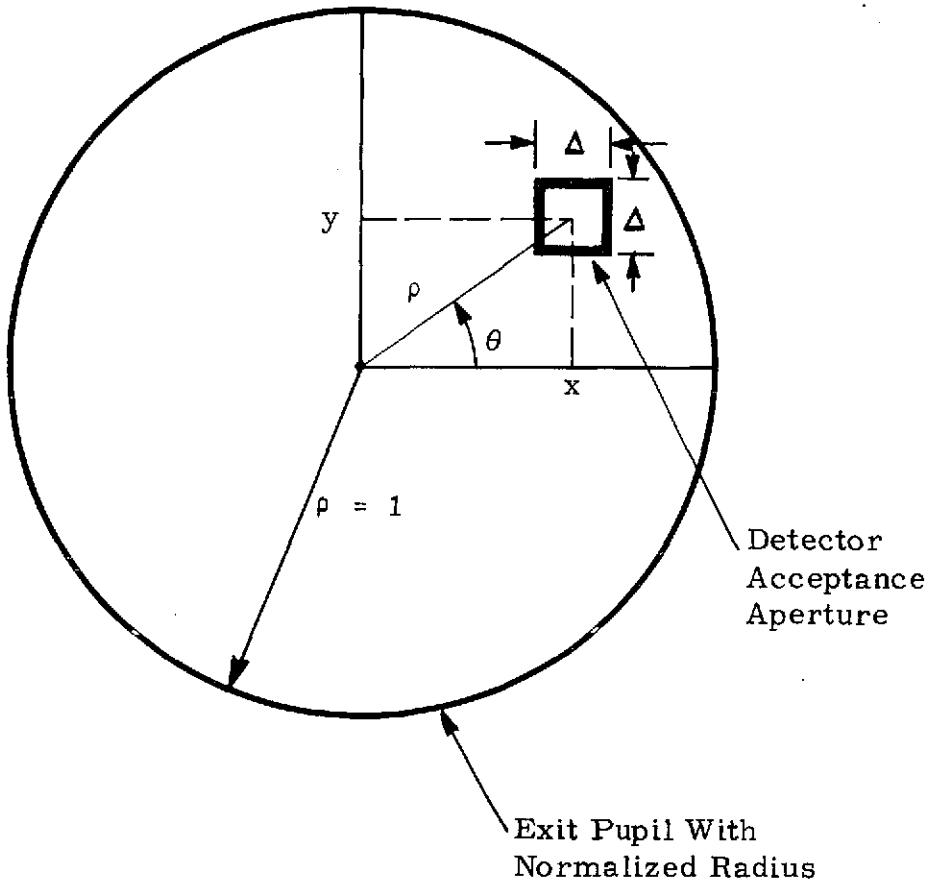

Figure 8. Geometry for Calculating the Error Resulting From Finite Detector Size

$$\phi = \frac{1}{\Delta^2} \int_{y-\Delta/2}^{y+\Delta/2} \int_{x-\Delta/2}^{x+\Delta/2} \Phi(x,y)\, dxdy$$

$$= \frac{1}{\Delta^2} \int_{y-\Delta/2}^{y+\Delta/2} \int_{x-\Delta/2}^{x+\Delta/2} \sum_{nm} A_{nm}\, \rho^n \cos^m(\theta)$$

The decomposition of the wavefront error Φ into an infinite series follows from Equation (28). In practice, the numerical value of A_{nm} for aberrations with a value m significantly larger than 2 is small. This permits the following significant simplification

$$\phi \cong \frac{1}{\Delta} \sum_{n,m} A_{nm} \cos^m(\theta) \int_{\rho-\Delta/2}^{\rho+\Delta/2} \rho^n\, d\rho$$

$$= \sum_{n,m} A_{nm} \cos^m\theta \left\{\rho^n + \frac{n(n-1)}{24}\, \rho^{n-2}\, \Delta^2 + \ldots\right\}$$

The expression in the braces is the sum of the first four terms in the expansion of the integral. The percentage error resulting by superimposing the pupil on a 10 x 10 square grid (i.e., $\Delta = 0.2$ when $\rho_{max} = 1$) is given in Figure 9. The error from tilt was not indicated since it is identically zero for all values of ρ. Note that the resultant error is acceptable, and can be eliminated from the signal with suitable processing.

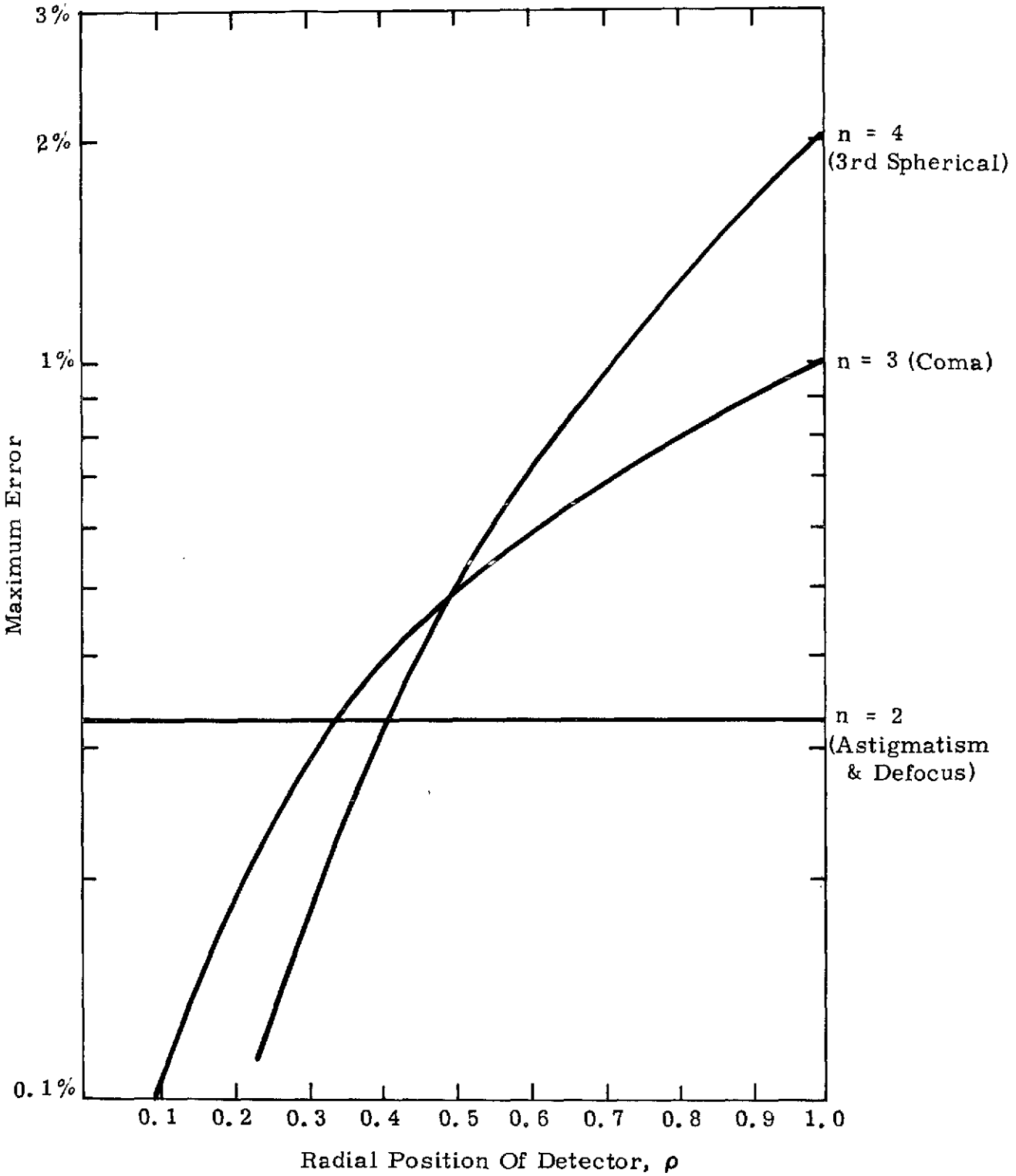

Figure 9. Maximum Error Resulting From Detector Size $\Delta = 0.2\rho$

SECTION IV

PHOTOMETRY REQUIREMENTS

The photometry requirements of the laboratory breadboard and LST Figure Sensors are limited by markedly different considerations. As demonstrated by Equation (10), the angular subtense of the source (i.e., the back illuminated pinhole for the laboratory breadboard and the source star for the LST Figure Sensor) must satisfy the inequality $\theta \lesssim \lambda/D_1$, where D_1 is the diameter of the imaging optics. This condition is satisfied in the case of the LST for all stars with the possible exception of three of the red giant stars, α Orionis, 0 Ceti, and α Scorpii which are of an angular size such that they will be nearly resolvable by a 3-meter aperture in space. Thus, the problem facing the LST operator is not that of finding a star of adequate angular size, but rather of locating a star with a spectral irradiance that satisfies the photometry requirements of the Stellar Figure Sensor. For the case of the laboratory breadboard, we have control over the source angular size by suitable choice of relay optics and pinhole diameter. As will be demonstrated in this section, the best performance of the breadboard is obtained by utilizing an illuminating source with the highest color temperature and emissivity available.

The design of a properly baffled optical system and the choice of low noise high internal gain photomultipliers should permit operation of the SFS in the signal shot noise limited domain by adequately reducing the effect of background, dark current, and Johnson noise sources. Combining the signal-to-noise ratio equation of Figure 3 (with $P_B = I_D = T_R = 0$) with Equation (19) yields the equation for the shot noise limited sensitivity of the SFS,

$$\frac{\Delta\lambda_{rms}}{\lambda} = \frac{\sqrt{2}\ hc\ B_{IF}\ (R + T\ d^2/D^2)}{8\pi\eta\lambda\ HA\ \tau_{OPT}\ TR\ \Gamma\ d^2/D^2} \tag{29}$$

$$= \frac{\sqrt{2}\ hc\ B_{IF}\ (1 + d/D)^2}{8\pi\eta\lambda\ HA\ \tau_{OPT}\ \Gamma\ (d/D)^2} \tag{30}$$

where $R_o = 1$ (i.e., lossless beamsplitter), T and R are defined by Equations (24) and (21), and all remaining terms are defined in Figure 3.

The single most important parameter in the calculation of the photometry for the SFS operating in the LST is the spectral irradiance of the source star. Unfortunately there is no simple linear relationship between this parameter and the visual magnitude and color class parameters, which are often used by astronomers. For the purpose of calculation, it is assumed that a class A_o star is being viewed by a SFS containing a 400Å filter whose center wavelength is 5,000Å. The star Sirius (whose visual magnitude is -1.6) is a typical member of the A_o class and has an effective temperature of 11,200°K. The irradiance of Sirius is $H = 4 \times 10^{-13}$ watt/cm^2.

Substituting the parameters of Table II into Equation (29), the theoretical maximum signal shot noise limited performance is obtained, and the results are plotted in Figure 10 with signal bandwidth as the parameter. If one considers a discrete system that sequentially dwells on each element in the exit pupil for an integration period of τ, the parametric curves of Figure 10 can be utilized by using the approximation:

$$\tau \cong 2/B_{IF}.$$

A question now arises: What is the chance of obtaining a suitable star in or near the LST field of view? Figure 11 gives the average number of stars per square degree for various angles relative to the galactic plane. Considering both Figures 10 and 11 note that the probability of having a suitable source star within the fine field is small.

The geometry for the photometry calculation of the laboratory breadboard is shown in Figure 12. Assuming a Lambertian source, the power detected by the photodetector is

$$HA = \left(W_\lambda \, \Delta\lambda \, \frac{\varepsilon}{\pi}\right) \left(\frac{\pi \mathcal{D}^2}{4}\right) \left(\frac{A}{f^2}\right) \tag{31}$$

where W_λ is the spectral radiant emittance and ε is the emissivity of the blackbody source. The first bracket represents the radiant emittance of the source near normal incidence and the second and third terms present the source

TABLE II. PARAMETERS FOR DERIVATION OF FIGURE 10

31034 Photodetector Quantum Efficiency $\eta = 0.25$

Wavelength $= 5 \times 10^{-7}$m

B_{IF} = IF bandwidth

A = 7×10^{-2} m^2 (assuming 100 sample points in pupil of 3-meter telescope)

d/D = 0.2 (ratio of reference spot diameter to pupil diameter)

Γ = 0.8 coherence function

τ_{OPT} = 0.7 transmission of optics

$\Delta\lambda$ = 400Å

λ = 5000Å

---

area and detection solid angle, respectively. Inserting the constraint listed in Equation (10), the above functional relationship is reduced to

$$HA = 8 \times 10^{-2} W_\lambda \Delta\lambda\varepsilon\lambda^2 \left[\frac{A}{\pi D^2/4}\right]$$

Note that the brackets contain a dimensionless quantity, which is the ratio of the detector area to the area of the acceptance aperture. Thus, we see that the only method for maximizing the breadboard detected energy is by maximizing εW_λ, i.e., using a source with the highest color temperature. To this end, a General Electric DZB 2-inch quartz halogen lamp was chosen since its color temperature is rated at 3300°K. The lamp filament is imaged upon the pinhole to obtain an effective high temperature "point source".

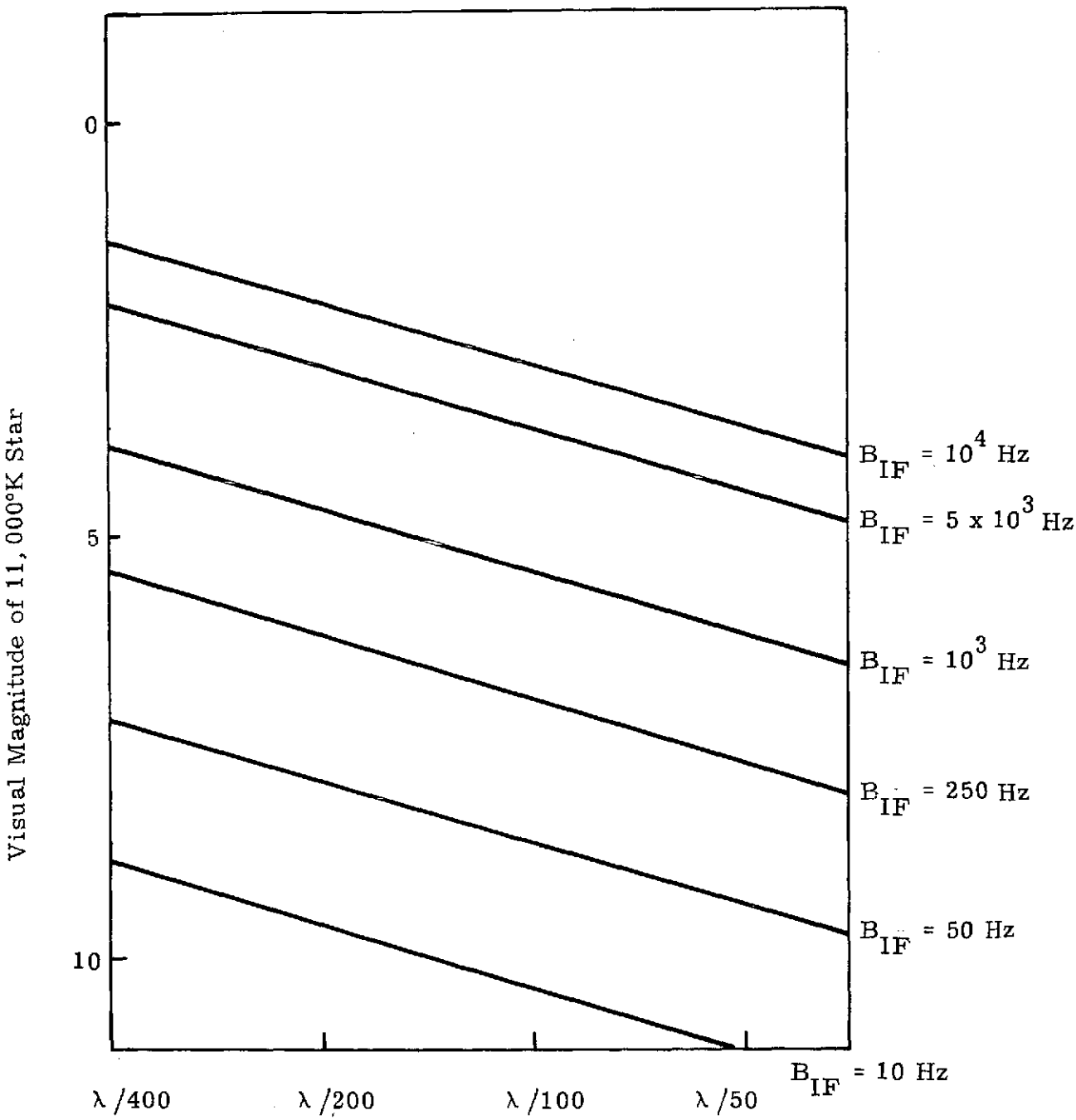

Figure 10. Shot Noise Limited Performance of SFS for Parameters in Table II

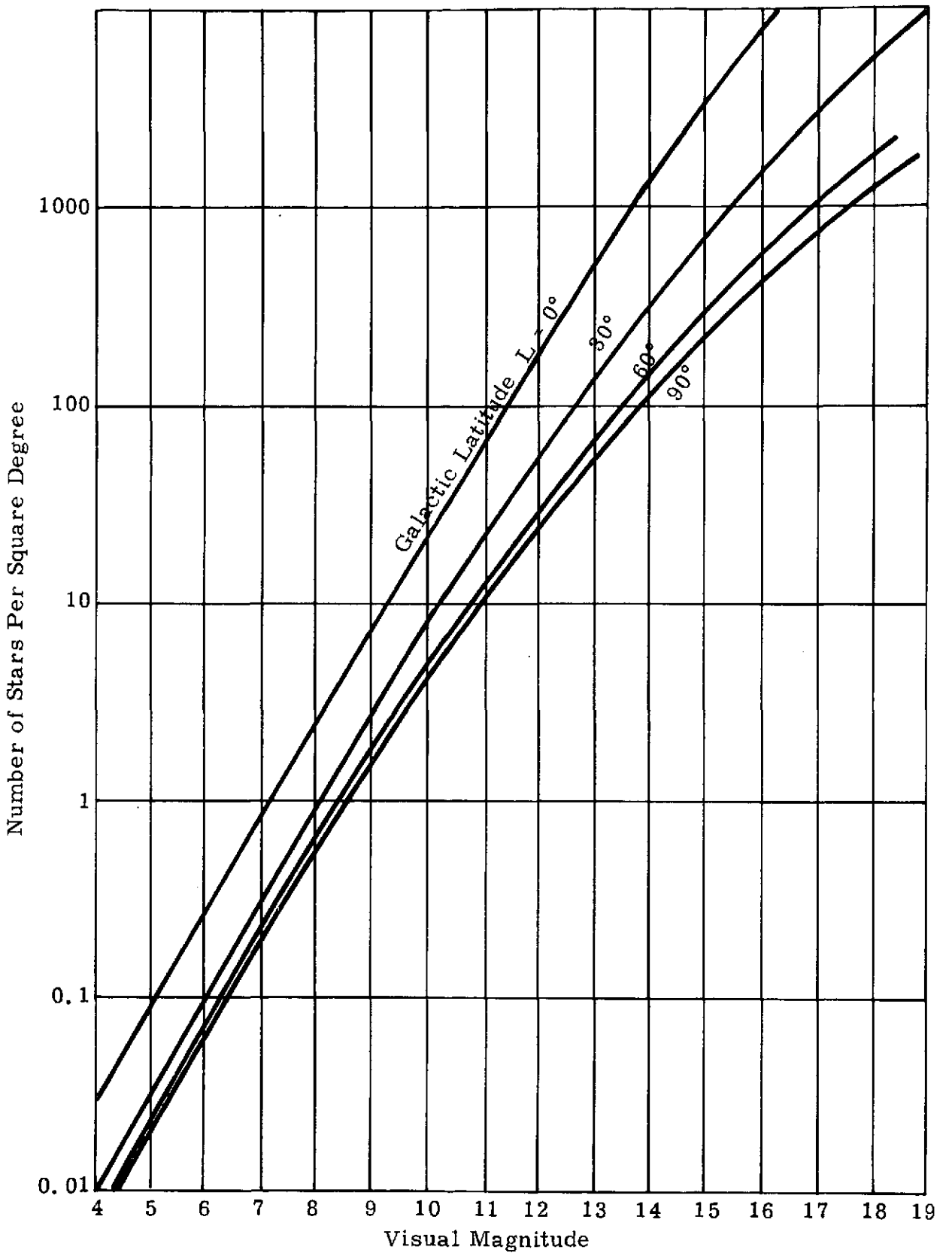

Figure 11. Available Source Star Density

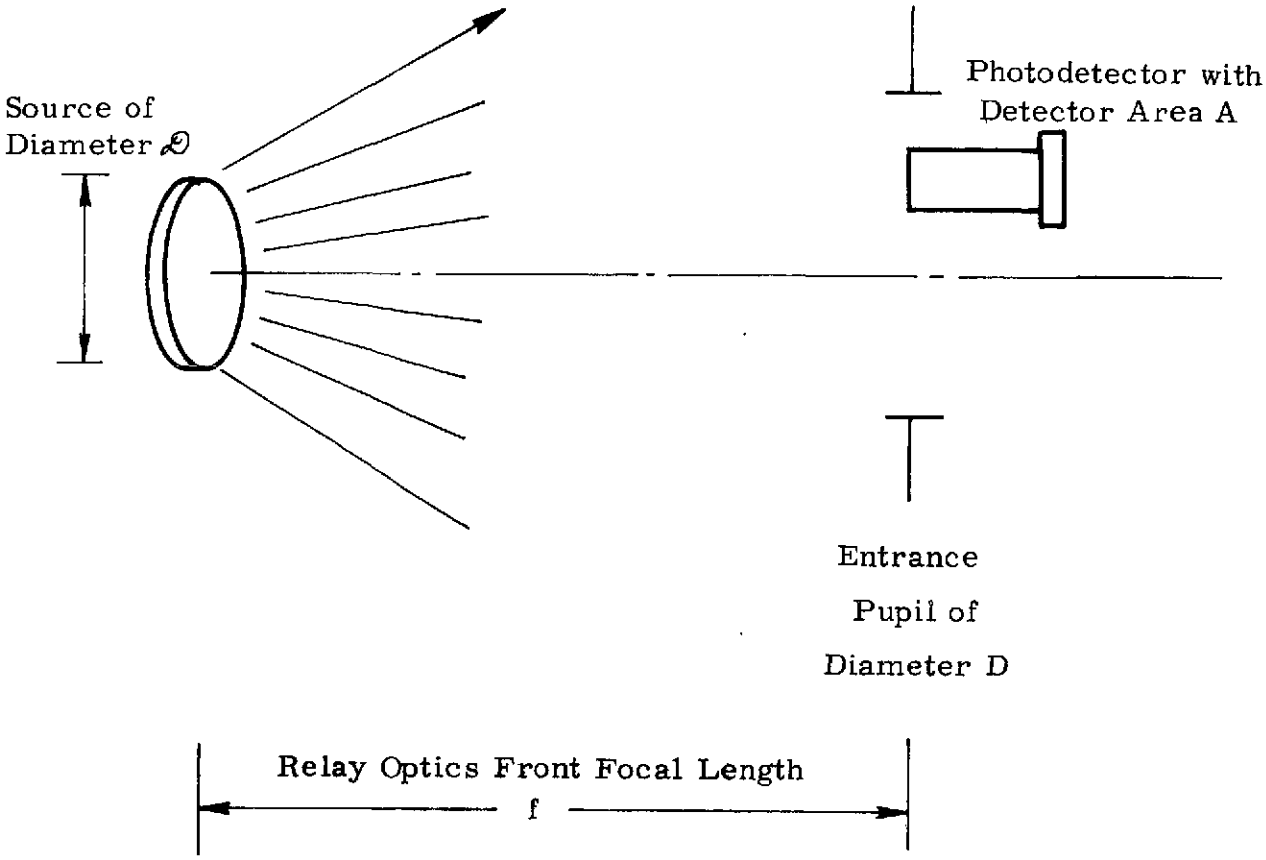

Figure 12. Geometry for Pinhole Photometry Calculations

SECTION V

ELECTRONICS

The objective of the electronics in the interferometer is to measure the phase difference between two sine waves. (See Figure 13.)

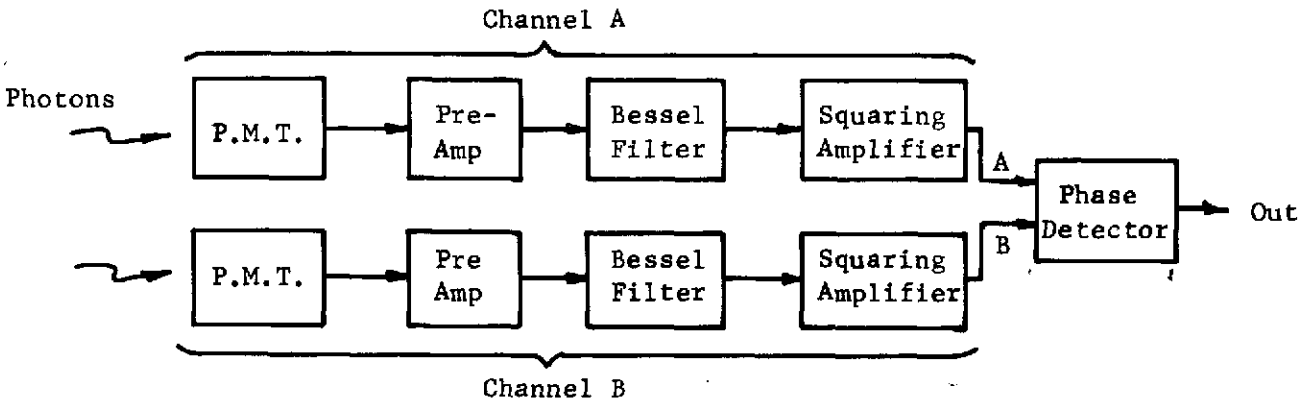

Figure 13. Electronic Detection Block Diagram

The output of the photodetector is amplified and filtered as shown in Figure 13. The filter used is a Bessel filter, which provides minimum phase distortion with no overshoot. It is important to have such a filter since the phases of Channels A and B reverse every time the piezoelectric sweep reverses and such discontinuities in phase would produce ringing or overshoot in the filters. The squaring amplifier, which provides a square wave, makes phase detection easier because detection of zero crossings determines phase difference. (See Figure 14.)

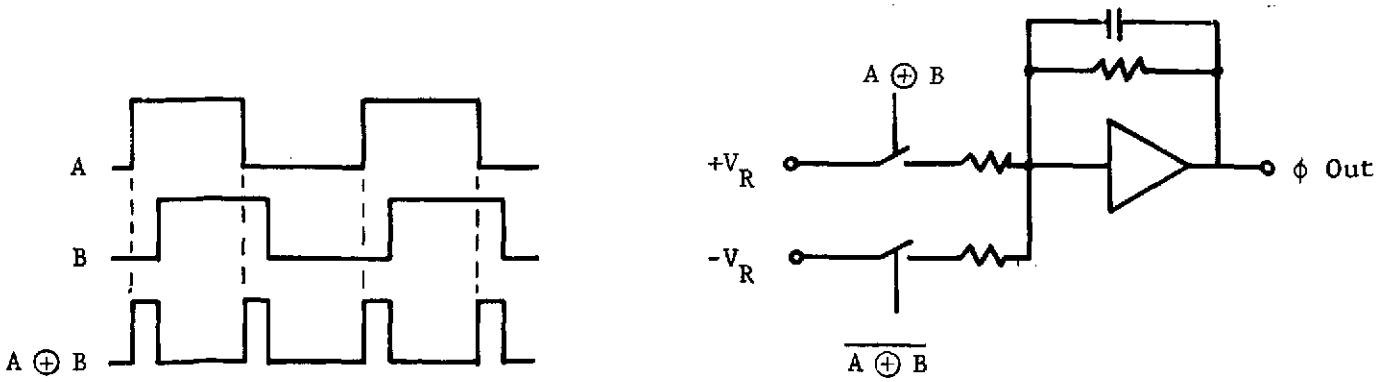

Figure 14. Phase Detector

$A \oplus B$ controls a solid state switch that allows $+V_R$ to be gated to the amplifier input whereas $\overline{A \oplus B}$ controls a switch that allows $-V_R$ to be gated to the amplifier input. Depending on the duty cycle of the switches, there is a certain dc output proportional to the phase difference between A and B. However, it should be noted that to obtain lead or lag information it is necessary to measure the difference between A $\lfloor 90°$, and B. (A $\lfloor 90°$ refers to A shifted by 90° to the original waveform A.) When such a phase detector is used, zero output is present when A and B are in phase, and the A $\lfloor 90°$ wave is compared with B in a manner similar to that shown in Figure 10. The phase differences between A and B, and A $\lfloor 90°$ and B are detected and provided as outputs.

The interface of the major electronic subassemblies is shown in Figure 15. The schematics for the subassemblies designed and fabricated at Perkin-Elmer are contained in Figures 16, 17, 18, 19, and 20. The remaining subassemblies were commercially purchased units.

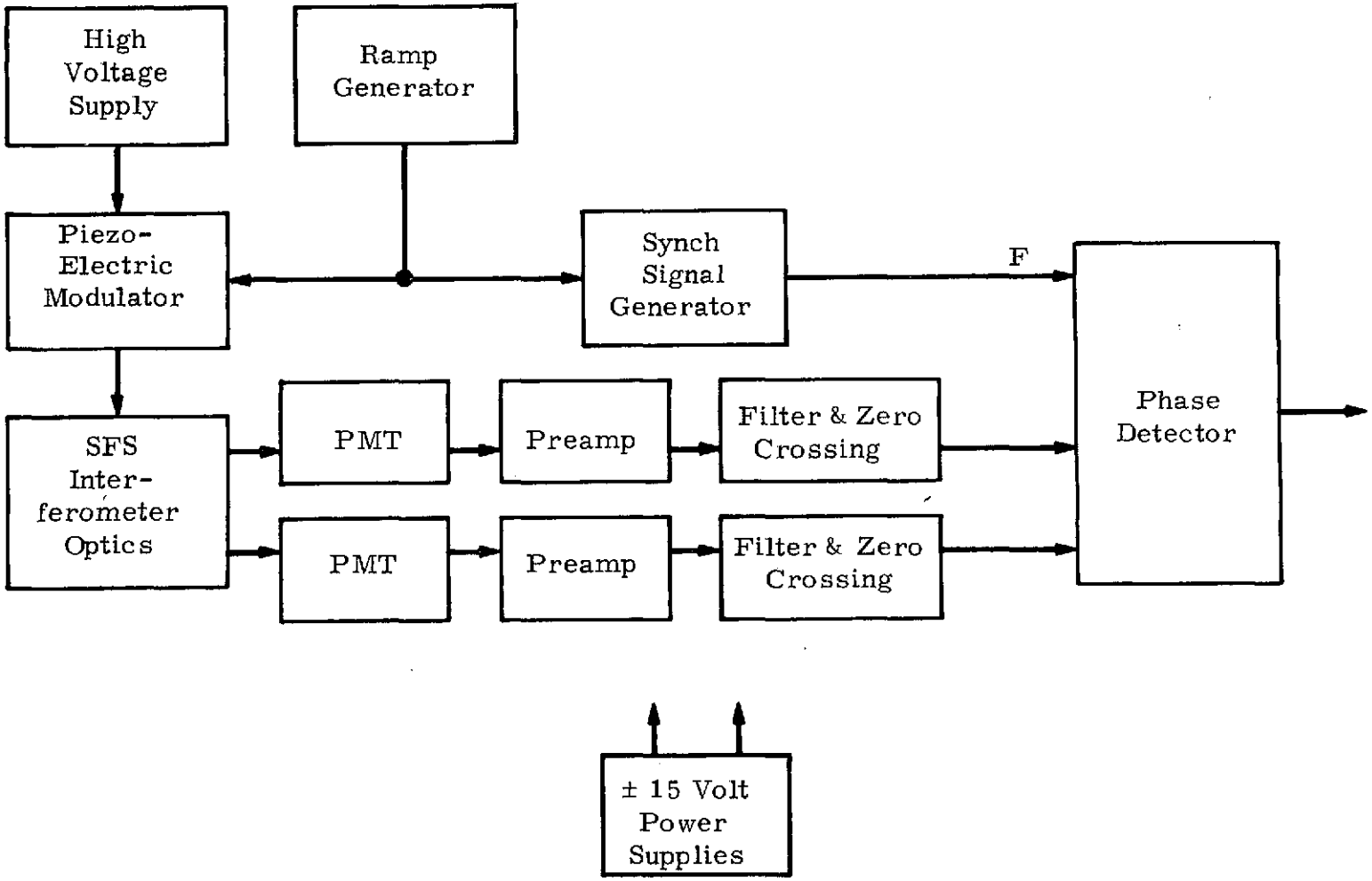

Figure 15. Electronic Subsystems Block Diagram

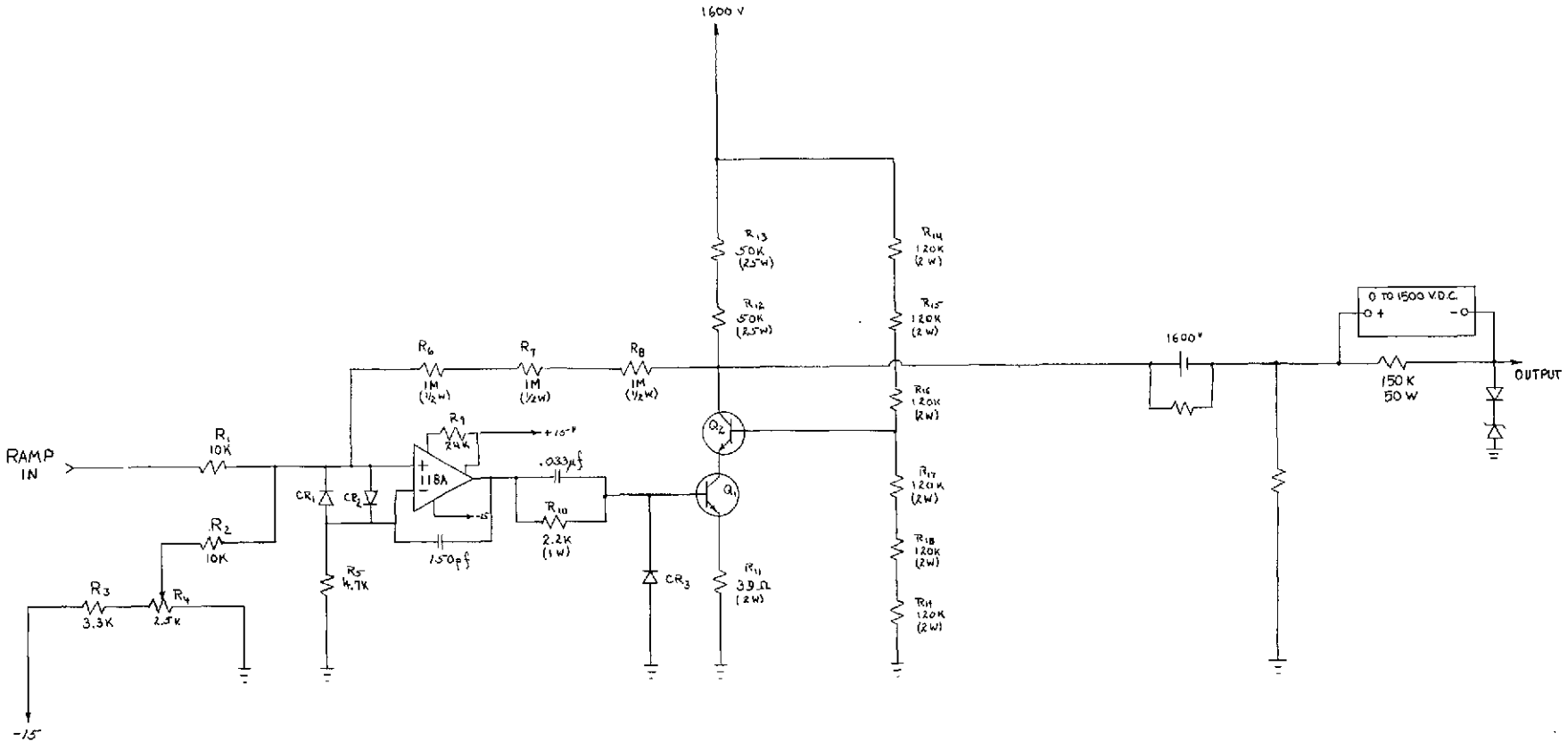

NOTES
1. Q_1 DTS-702
   Q_2 DTS-702
2. CR1 1N914
   CR2 1N914
   CR3 1N914

Figure 16. Piezoelectric Drive Circuit

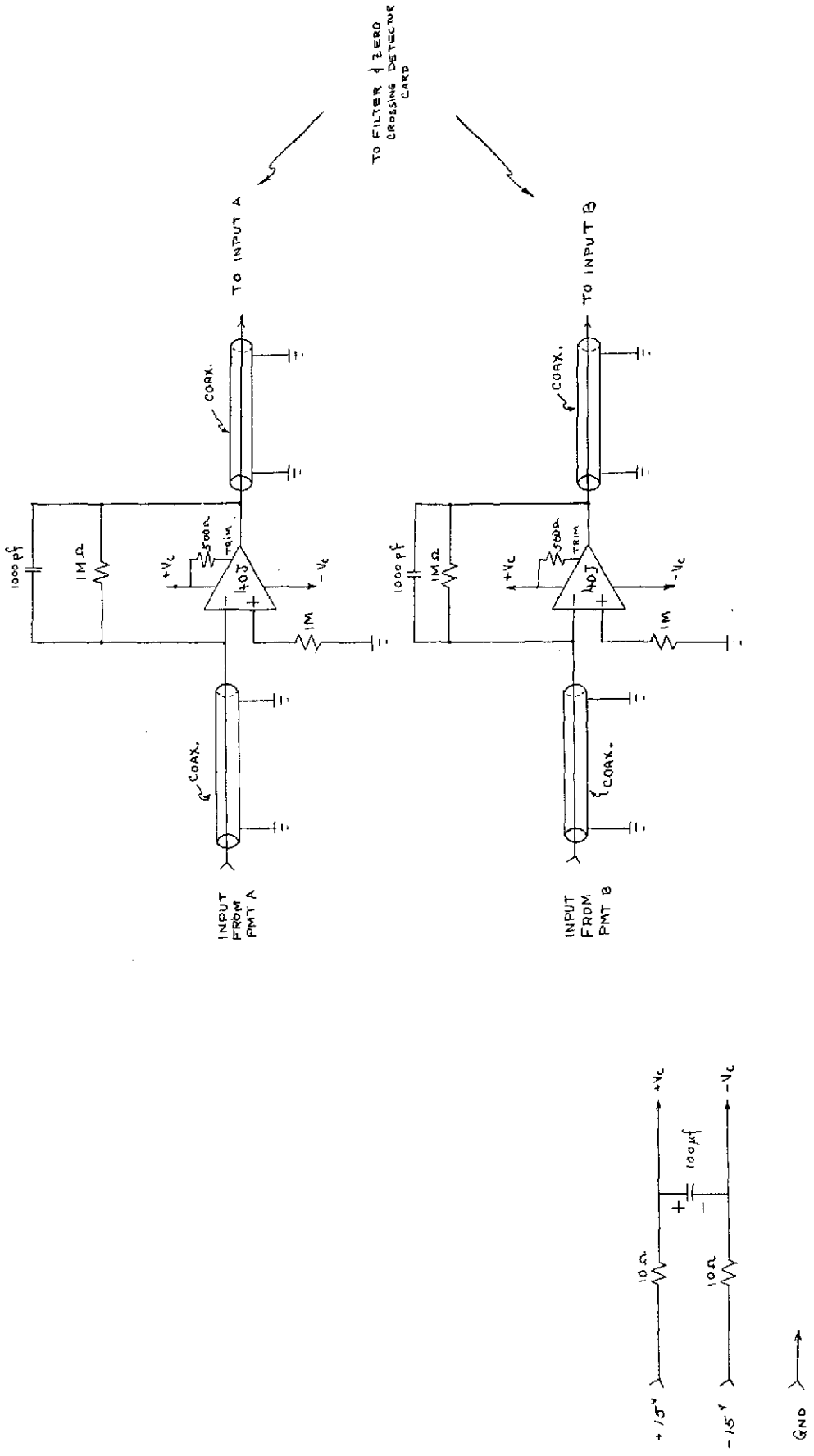

Figure 17. Preamplifier for A and B

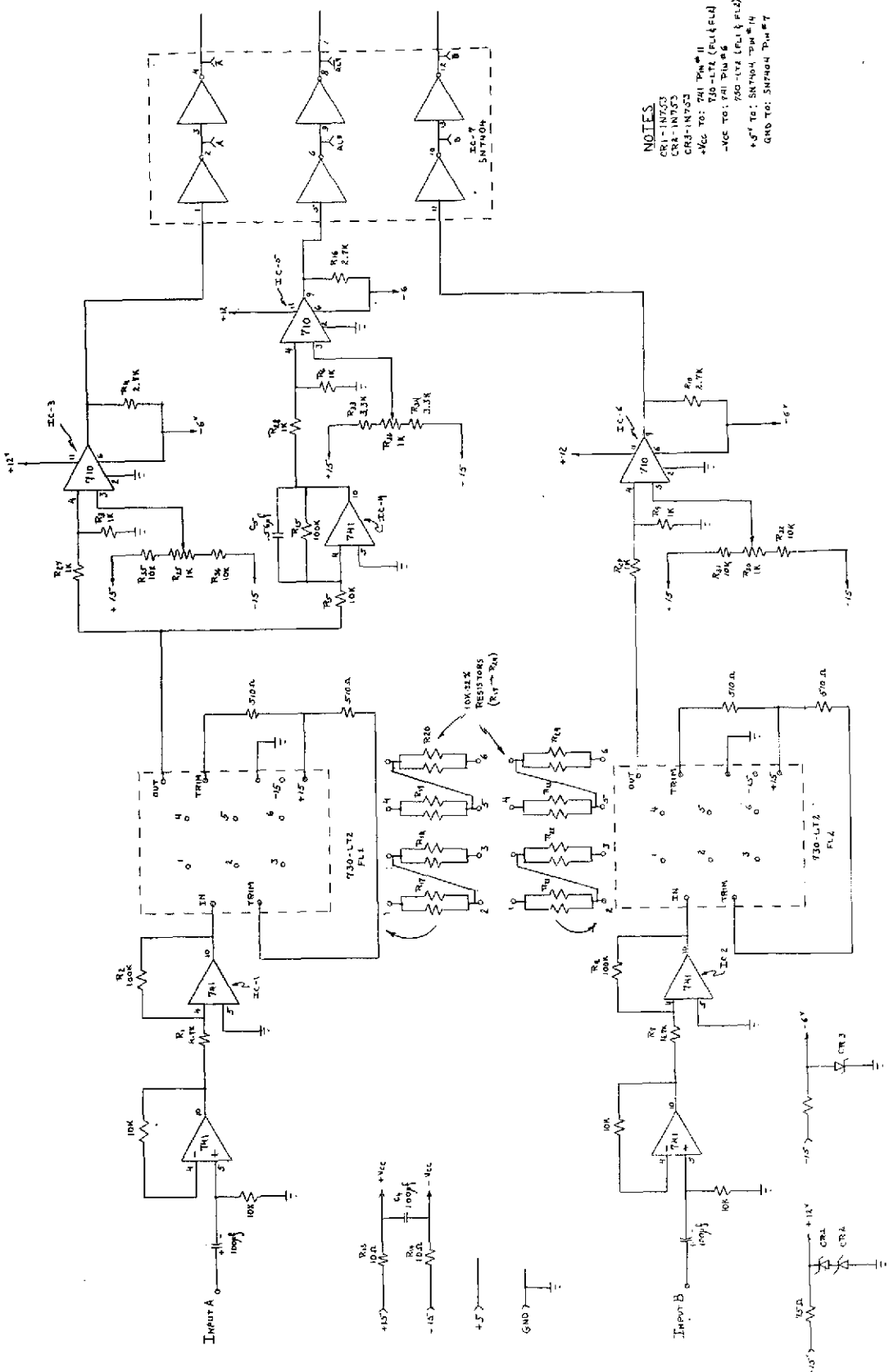

Figure 18. Filter and Zero Crossing Detector

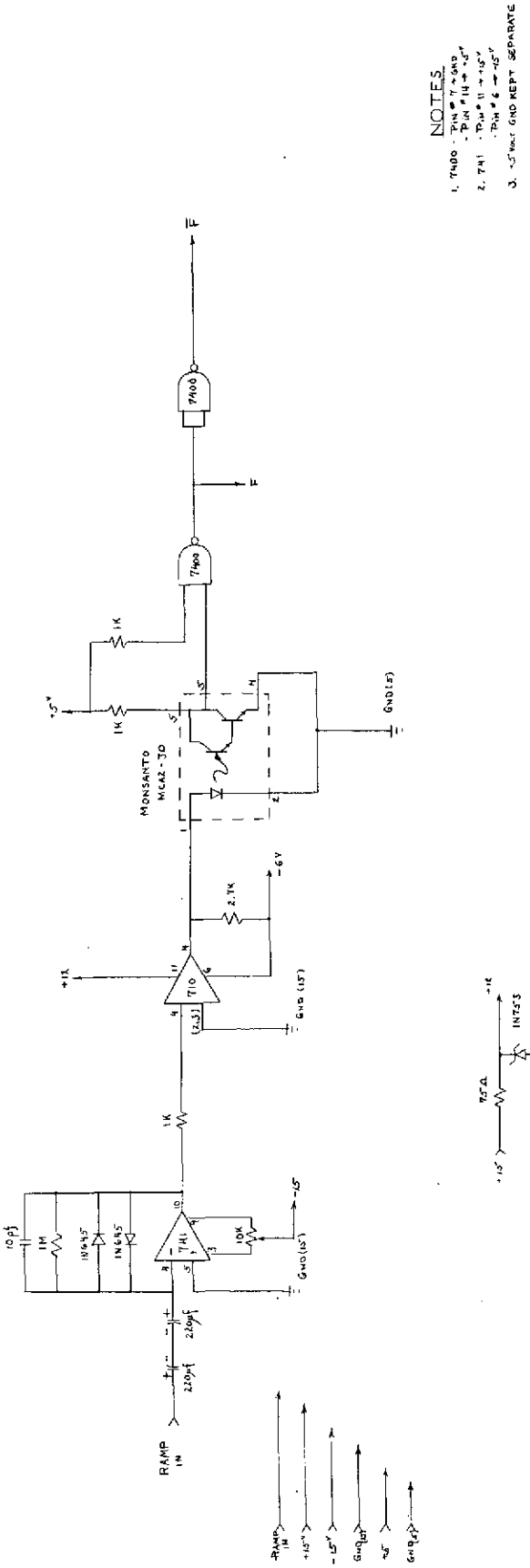

Figure 19. The F and $\overline{F}$ Generators

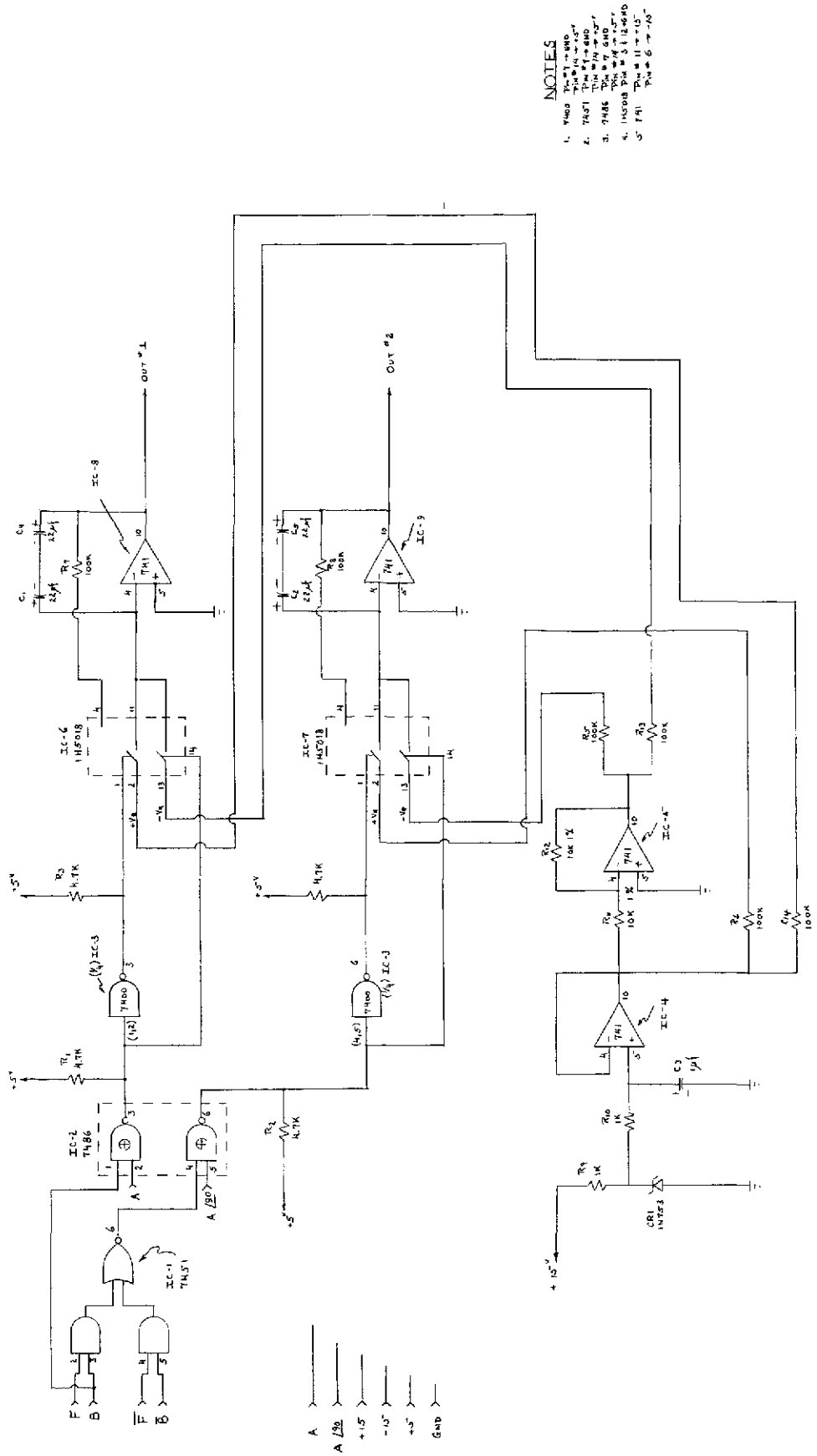

Figure 20. Phase Detector

SECTION VI

LABORATORY BREADBOARD

A laboratory breadboard was designed, fabricated, assembled, and utilized to verify the mathematical model previously presented. Also, the unit allows us to obtain practical experience with stellar figure sensors that will be valuable in the conceptual design of a flight unit. Views of the assembled hardware are contained in Figures 21, 22, and 23. An indication of the size of the breadboard is obtained by noting that the distance between bolt centers on the iron table is 5.08 cm. An overlay on Figure 21 traces the path of the light rays originating at the light source and propagating through the system. Although the picture indicates that the optical filter is placed between the light source and the pinhole, dual filters were placed immediately preceding each PMT to reduce the detected background radiation. The eyepiece of a microscope images the lamp filament on the pinhole. The objective of this microscope forms a demagnified image of the pinhole at the focus of an off-axis collimating parabolic mirror. The use of these relay optics permits the experimenter to satisfy the requirements of Equation (10) with relatively fast optics and feasible pinhole sizes. The 2.54 cm diameter collimated light is divided into two portions at the beamsplitter, the reference beam (solid line in Figure 21) being reflected from the aluminized dot of 5.08 mm diameter and the remaining (dashed line) signal beam transmitted through the beamsplitter. The reference beam is retroreflected and laterally displaced by the all-reflective corner cube. The cube was fabricated by optically contacting three blocks of polished fused silica as shown in Figure 23. The mount for the cube is mated with a cylindrical piezeolectric pusher, shown on the left of Figure 23. The return beam is expanded by an afocal telescope which consists of two confocal parabolas. The expanded 2.54 cm diameter output of the telescope is combined at the beamsplitter with the signal beam which is returned from the reflective Porro prism. The resultant fringe pattern is sampled by a stationary pick-off mirror (for the A reference channel) and by a translatable pick-off mirror for the B channel. The

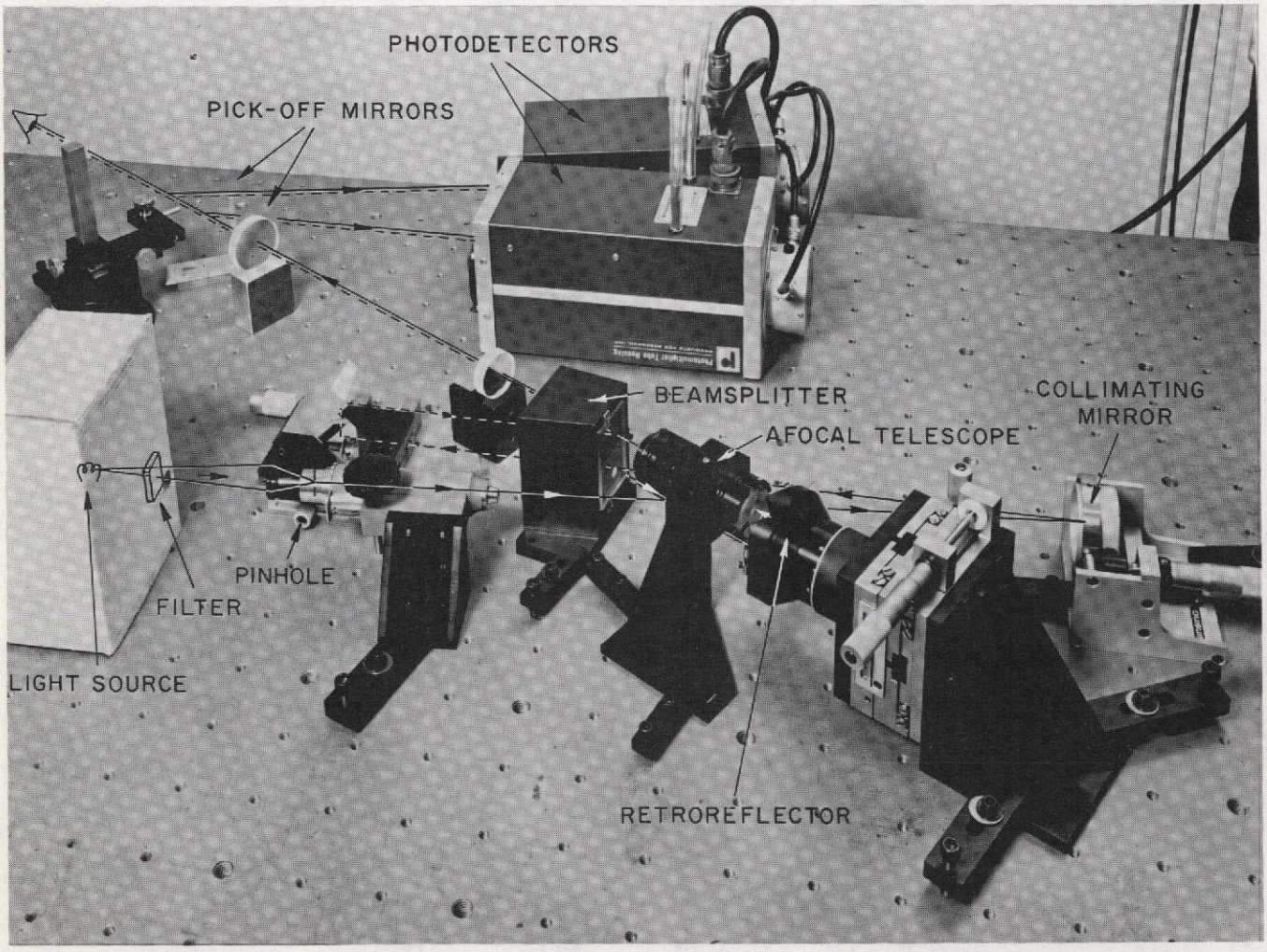

Figure 21. Stellar Figure Sensor Breadboard

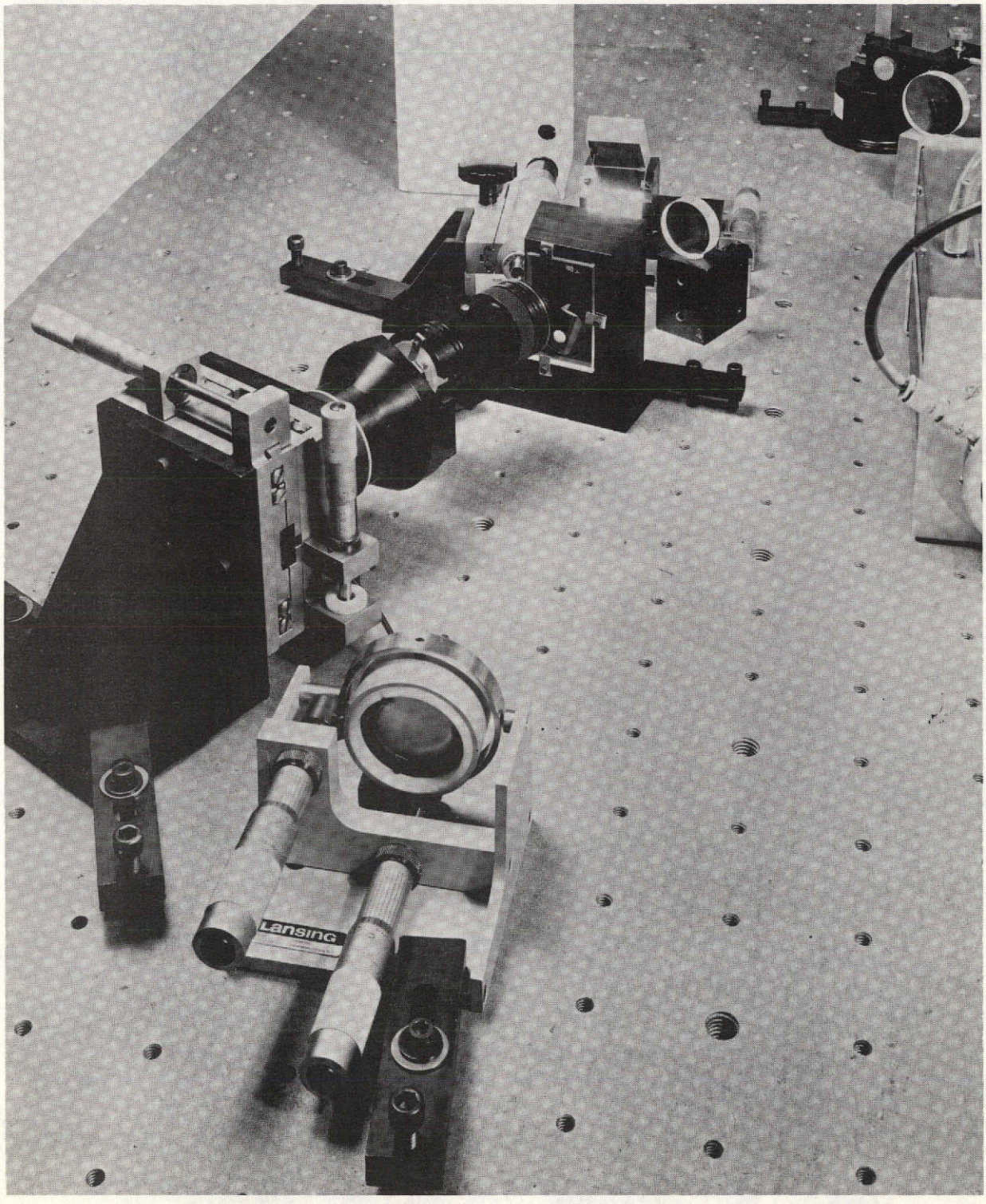

Figure 22. Alternate View of Stellar Figure Sensor Breadboard

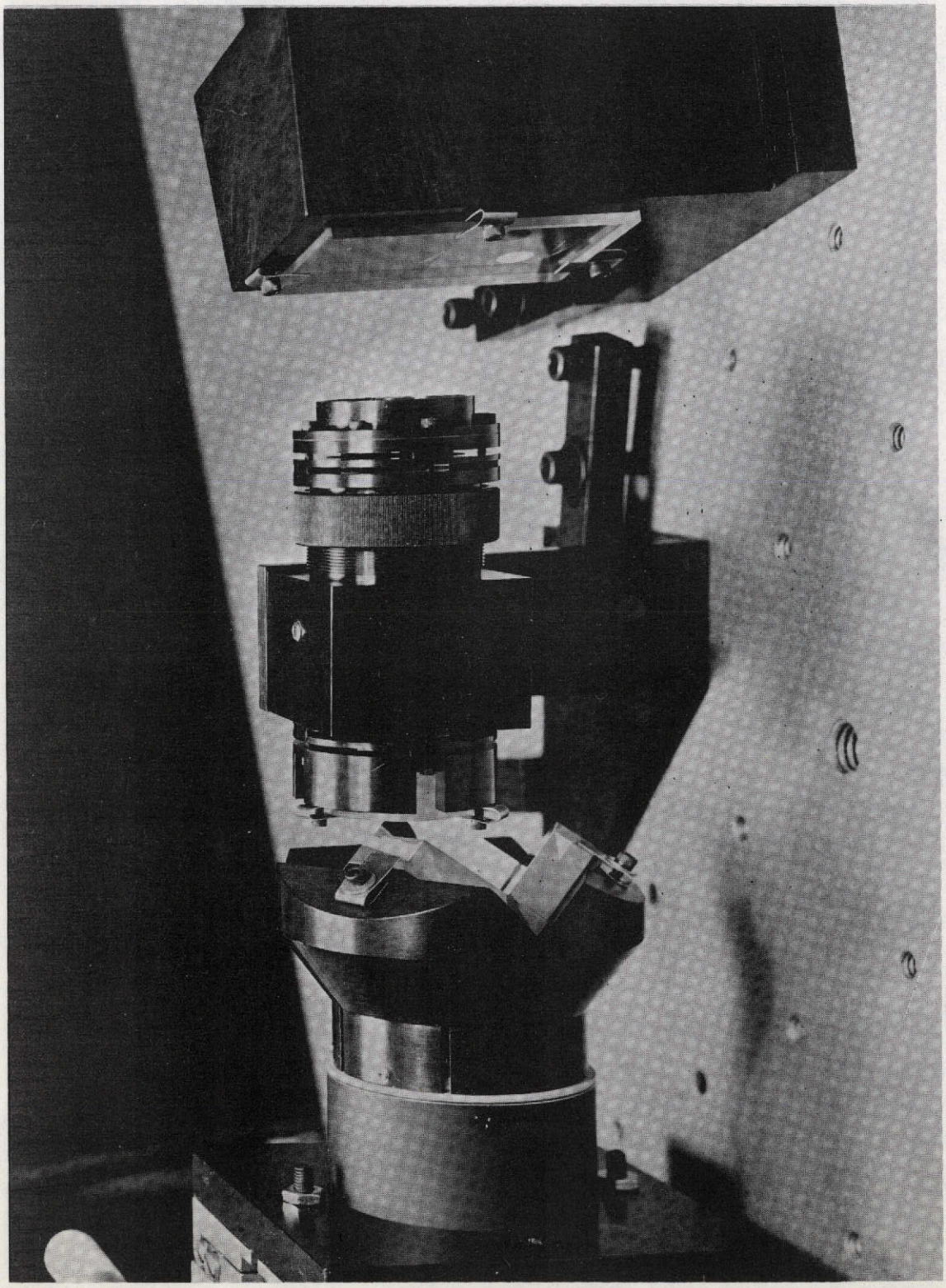

Figure 23. Beamsplitter, Afocal Telescope, and Piezoelectric Translated Retroreflector

photodetectors for the two channels are cooled RCA 31034. This specific tube was chosen because of its large spectral bandwidth and high quantum efficiency, both of which are requirements for the SFS. The factory calibration data for the two tubes is shown in Figure 24. Since the performance of both PMT's was fairly near nominal, the commercial data sheet can be used to estimate the remaining critical parameters. Unfortunately, the ultimate noise performance of the tube is only obtained by cooling, thus requiring the use of two Peltier coolers. Two commercial units, Model TE-104, manufactured by Products for Research were used.

CT# 1014 Date 4/20/72
Tube Type C31034
Serial# 504000
Cathode Sensitivity
Radiant @ _____ Å _____ A/W
Narrow Band @ 8600 Å 97 x 10⁻³ A/W
Luminous @ 2870° K 8.0 x 10⁻⁴ A/lm
Blue @ 2870° K + CS _____ Filter _____ A
Red @ 2870° K + CS _____ Filter _____ A
Anode Sensitivity
Luminous @ 2870° K @ 1500 V 185 A/lm
Blue @ 2870° K + CS _____ Filter @
_____ V _____ A
Anode Dark Current @ 1410 V and/or
100 A/lm 3.5 x 10⁻⁹ A
Pulse Height _____ V
Pulse Height Resolution _____ %
Source _____
Scintillator _____
Dark Pulses $\sum_{-\ell}^{-\ell}$ = _____ CPM
@ _____ V
Others
Ik @ 6943 Å : 82 ma/w
Reference Bulletin Dated _____
TL 3735 7/70 E.F.

(a)

CT# 1014 Date 4/20/72
Tube Type C31034
Serial# 503740
Cathode Sensitivity
Radiant @ _____ Å _____ A/W
Narrow Band @ 8600 Å 44 x 10⁻³ A/W
Luminous @ 2870° K 4.1 x 10⁻⁴ A/lm
Blue @ 2870° K + CS _____ Filter _____ A
Red @ 2870° K + CS _____ Filter _____ A
Anode Sensitivity
Luminous @ 2870° K @ 1500 V 140 A/lm
Blue @ 2870° K + CS _____ Filter @
_____ V _____ A
Anode Dark Current @ 1450 V and/or
100 A/lm 7.2 x 10⁻⁹ A
Pulse Height _____ V
Pulse Height Resolution _____ %
Source _____
Scintillator _____
Dark Pulses $\sum_{-\ell}^{-\ell}$ = _____ CPM
@ _____ V
Others
Ik @ 6943 Å : 45 ma/w
Reference Bulletin Dated _____
TL 3735 7/70 E.F.

(b)

Factory calibration sheet for the breadboard detectors. Unit (a) was used in the scanning channel and unit (b) was used in fixed channel.

Figure 24. RCA 31034 Calibration Data

SECTION VII

LABORATORY EXPERIMENTS

The Stellar Figure Sensor (SFS) Breadboard discussed in the previous section was subjected to an extensive test program which had three objectives:

- Verify the mathematical model.
- Obtain engineering data useful for the design of future operational focal plane figure sensors.
- Demonstrate the viability of the optical, mechanical, and electronic design of the SFS.

The test program obtained data that demonstrated all three objectives were satisfied. The signal-to-noise model and the calculation of expected signal waveforms were verified experimentally. Data reduction of the SFS output signals indicated that the interferometer measurements of the lower spatial frequency wavefront errors had a repeatability of $\lambda/100$ on a root-sum-squares basis. The wavefront errors with a p^3 and p^4 dependance (i.e., coma and spherical) has a somewhat reduced repeatabilty of $\lambda/25$ and $\lambda/11$. This operational accuracy can be improved by increasing the numbers and the positional accuracy of the sample points in SFS output pupil. A measurement of noise sources in the system also indicated that the SFS could be upgraded with a different type of electronic processing of data, thus allowing detection of errors of magnitude of $\lambda/100$, or better.

The test procedure of the SFS breadboard was marked by a number of milestones:

(a) Component and assembly tests

(b) Verify parameters of output signal waveforms

(c) Measure magnitude of SFS noise sources

(d) Calibrate optical system

(e) Test SFS against an aberration plate having a known wavefront error

(f) Determine long-term stability of the interferometer

The procedure for obtaining and reducing the data for the above experiments will be presented in this section.

7.1 PREASSEMBLY TESTS

Since only two elements of the SFS breadboard have optical power, subassembly testing was limited. The two parabolae of the beam expander were aligned by placing the telescope assembly in a laser illuminated interferometer. The interferogram of the aligned telescope is shown in Figure 25.

The off-axis collimating parabola was aligned by illuminating the pinhole with helium-neon laser light and monitoring the collimated output beam. This resultant collimated laser beam was also used to properly adjust the clear apertures of the remaining optics of the interferometer.

7.2 OUTPUT SIGNAL WAVEFORMS

The output signal waveform as measured at the output of the photomultiplier is calculated in Section III and the expected waveforms for a number of special cases are given in Figures 5 and 6. The output signal waveforms for three cases were recorded as shown in Figures 26, 27, and 28. The straight lines in each figure indicate the zero voltage level for the respective trace. The significant operational parameters of the SFS for these cases are tabulated in Table III.

The upper trace of the "white light fringe" signal (Figure 26) is remarkably close to that predicted. However, the bottom trace shows some skewness to the waveform indicating some dispersion at the location in the pupil

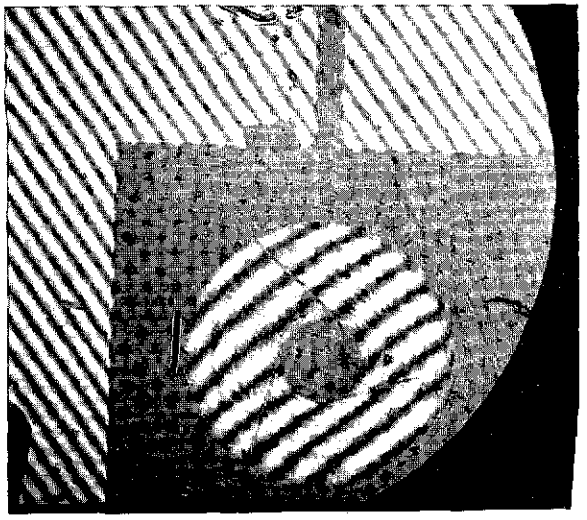

Figure 25. Double-pass Interferogram of the SFS Afocal Telescope

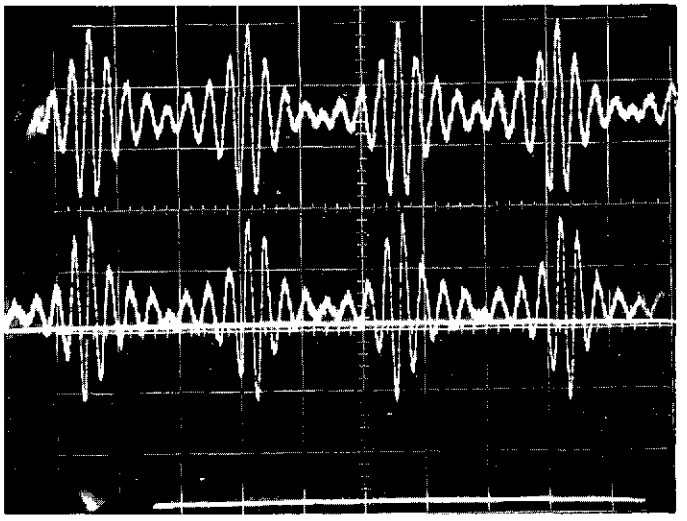

Figure 26. Signal Waveforms of "White Light" Fringes

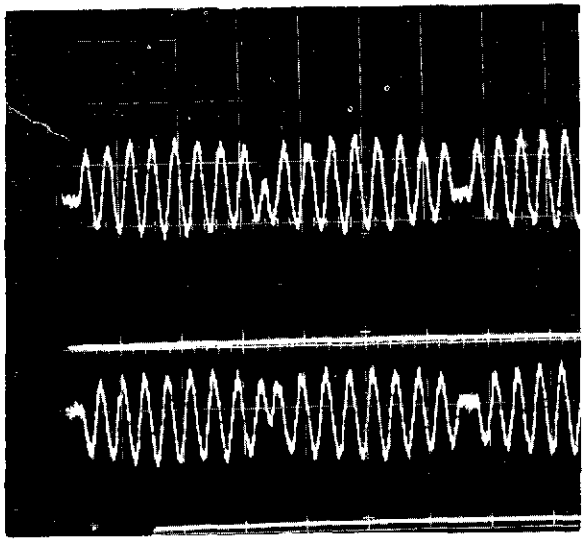

Figure 27. Signal Waveform with IR Bandpass Filter

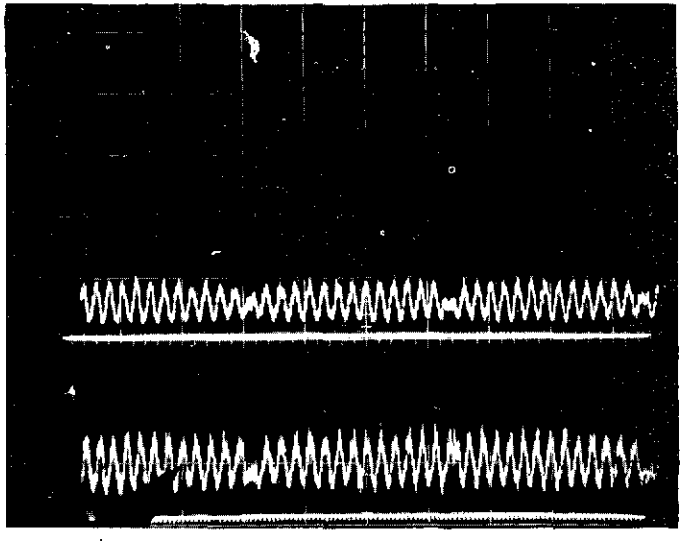

Figure 28. Signal Waveform with Visible Bandpass Filter

TABLE III. SFS OUTPUT PARAMETERS

Case	Signal Waveform in Figure	Spectral Range (μ)	Δλ/λ	Filter Source and Number	Max. Trans.	Nearest Analytically Derived Waveform in Figure	PMT Voltage
White Light	26	0.55 - 0.92				6b	-1450
IR Bandpass	27	0.80 - 0.90	0.12	Schott RG-780	0.92	5c	-1350
Visible Bandpass	28	0.496 - 0.517	0.04	Baird-Atomic 31-16-7	0.61	5b	-1600

The parameters for all oscilloscope traces are:

upper trace: scanning detector
lower trace: fixed detector
vertical scope scale: 100 mv/cm
horizontal scope scale: 0.25 sec/cm
polarizer: horizontal plane

being interrogated. This dispersion is thought to arise from a residual wedge in the substrate of the beamsplitter. This misfortune indicates that dispersion must be considered when a focal plane figure sensor is to be operated in white light. Note also, that the dispersion does not visibly affect the two remaining cases utilizing bandpass filters.

Figure 27 shows the output signal waveform obtained when the Schott RG-780 infrared filter is inserted into the figure sensor. Notice that the signal is minimally perturbed by noise and envelope modulation that result from coherence effects. The cusps in the waveform occur at the reversal points of the piezoelectric drive of the retroreflector. Thus, each consecutive group of eight cycles of the sinusoid is a mirror image of the previous group. The short horizontal portion of the waveform resulted from a limiting on one end of the retroreflector piezoelectric drive voltage.

Figure 28 indicates the signal waveform that results when a 21.0 nanometer bandpass green filter is inserted into the interferometer. Referring to Figure 4, note that the breadboard spectral response is significantly reduced at 500 nanometers as a result of the reduced spectral radiance of a 3300°K source in the visible, while the lower trace (fixed detector) shows a significant increase of noise in signal. A check of the RCA 31034 photomultiplier tube calibration data (Figure 24) indicated that the fixed detector had a lower quantum efficiency, but had a higher, and self-compensating internal gain, which thus gave comparable anode sensitivities for both tubes. However, if the signal is shot noise limited, the SNR is determined by the statistics of the photoelectron current from the cathode and is unaffected by the internal gain of the tube. This is one of several indications that the SFS is truly noise-in-signal limited.

After comparing the signal waveforms obtained from the cases described, the decision was made to use the RG-780 filter in the optical system for all succeeding experiments.

7.3 SYSTEM NOISE SOURCES

A simplified signal flow diagram of one detection channel for the SFS is shown in Figure 29. A series of measurements were made on the SFS electronics to determine the relative contributions of the following noise sources:

- preamplifier noise
- photomultiplier dark current
- noise in signal
- absorption in two arms of interferometer

The preamplifier performs the dual functions of a current-to-voltage conversion (1 microamp to 1 volt) and low pass filter of 155 Hz bandwidth. The readings in Table IV were made at the output of the preamplifier. If these values are to be used for calculating the performance of the electronic phase detector, all noise power values should be reduced by 155/66 = 2.3, since the signal is subjected to additional filtering by a 66 Hz bandwidth Bessel filter subsequent to processing by the phase measuring electronics.

Noise measurements were made on the SFS operating in the white light mode (no filter) and with the 0.84μ and the 0.5μ filters. The general conclusions from these results are:

(1) The preamplifier noise is not significant.

(2) The dark current for a cooled PMT is not significant.

(3) The noise-in-signal (mainly photon noise and spurious modulation) is the predominant noise source.

(4) The SFS operating with white light and 0.84μ filter gave a virtually noise-free signal for the parameters chosen in the laboratory breadboard.

(5) Photon noise is the limiting noise source at low power levels and spurious modulation resulting from turbulence and mechanical vibrations limit the SFS for SNR greater than 20.

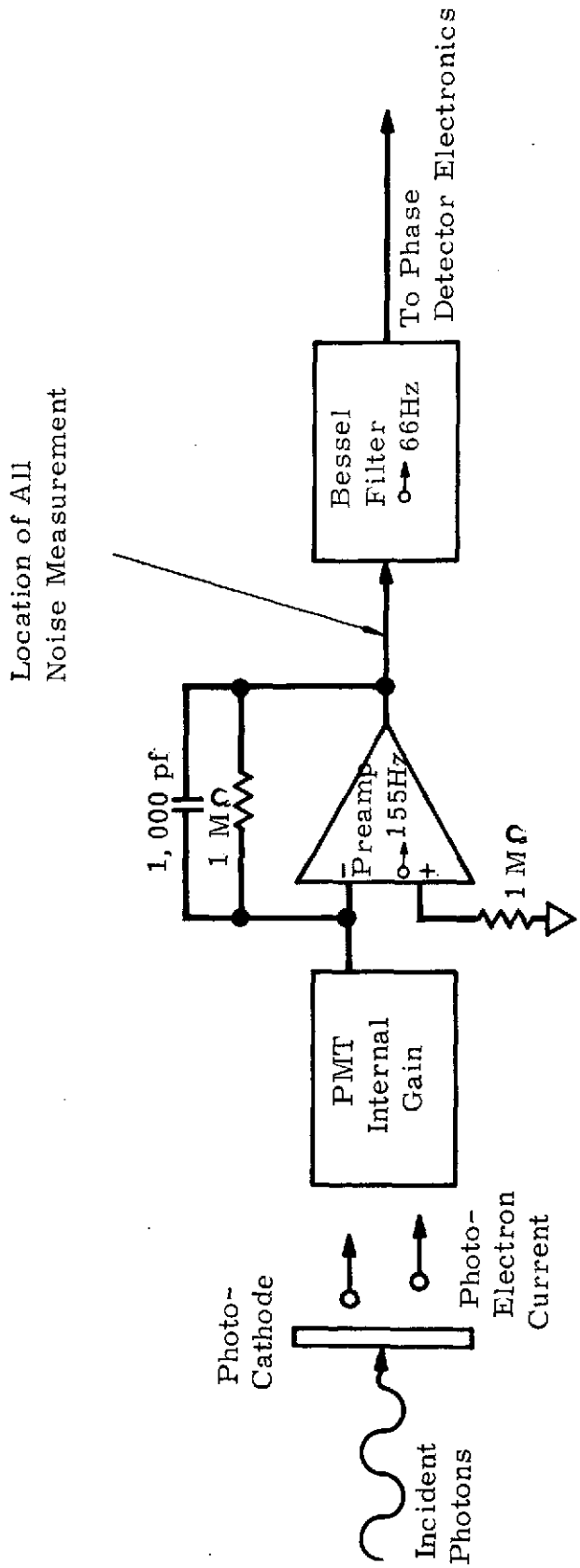

Figure 29. Signal Flow Diagram

The coherence function is varied by translating the porro prism mount and thus changing the length of one interferometer arm relative to the other. If both arms of the interferometer are of identical length, the detectors view the null fringe ($\Gamma \approx 1$). With a difference in length much greater than the coherence length of the light, the two interferometer beams are combined incoherently and $\Gamma = 0$. The readings with $\Gamma = 1$ are used to determine the signal power and the $\Gamma = 0$ readings are used to determine the signal shot noise.

7.4 VERIFICATION OF SIGNAL-TO-NOISE EQUATION

The expression for the system signal-to-noise ratio equation is given in Equation (20). The validity of the equation was verified by substituting the system parameters into Equation (20) and comparing the results with the data of Table IV. Cases 4 through 7 (Table IV) indicate that the RMS noise resulting from the preamplifier and dark current (less than 1.3 mvolt) are all considerably less than the RMS noise component for noise-in-signal (4 mvolt). Omitting the dark current and preamp noise sources from Equation (20) allows the following simplification:

$$SNR = \frac{n\lambda HA\Gamma^2}{hcB_{IF}} \cdot \frac{TR}{M^2 (R + T/M^2)} \tau_i \qquad (20a)$$

The numerical value for each of these parameters for the laboratory breadboard unit is given in Table V. The values τ_i are multiplicative transmission coefficients for the individual optical components in the system.

The optics transmission coefficient is calculated from the estimated transmission of the glass enclosure of the lamp, microscope, off-axis parabola, beamsplitter, and the relay optics in the interferometer output. The transmission coefficients of a flight instrument will be significantly superior to these values as the result of the deletion of many of the relay optics, and the use of more sophisticated reflection and antireflection coatings.

TABLE IV. SYSTEM NOISE MEASUREMENTS

Case No.	Light Source	PMT High Voltage	Optical Filter	Coherence Function	RMS MVolt AC -Coupled	RMS MVolt DC-Coupled	Detector S-Scanning F-Fixed	Optical Bandwidth	Comments
1	Off	0	None		1.3	7	S	White Light	Preamp Noise Negligible
2	On	1250		0	4	420	S		Optical bias measurements
3	On	1250		1	100	450	S		Depth of modulation
4	Off	0	Schott RG-780		1	6.5	S		Preamp Noise
5	Off	0			1.3	8	F		Preamp Noise
6	Off	1350			1	9	S	IR Band Pass	PMT Dark Current + Preamp
7	Off				1.3	8	F		PMT Dark Current + Preamp
8	On			0	4	200	S		Noise on unmodulated light
9	On			0	4.5	160	F		Noise on unmodulated light
10	On			1	33	200	S		Signal + Noise Measurements
11	On			1	31	170	F		Signal + Noise Measurements
12	Off	0	Baird Atomic 31-16-7		1.4	7	S	Visible Band Pass	Preamp Noise
13	Off	0			< 1	7	F		Preamp Noise
14	Off	1600			2.2	40	S		PMT Dark Current + Preamp
15	Off				3	30	F		PMT Dark Current + Preamp
16	On			0	4.3	70	S		Noise on Unmodulated Light
17	On			0	6.5	70	F		Noise on Unmodulated Light
18	On			1	10	80	S		Signal + Noise Measurements
19	On			1	16	70	F		Signal + Noise Measurements
20	On	1350	RG-780	0	7	280	F	IR Band Pass	Reference Reading
21	On			0	6	230	F		Retro-arm blocked
22	On			0	3	45	F		Porro-arm blocked

Comments:

1. Photomultipliers cooled for all measurements
2. Horizontal polarization
3. All measurements made at preamp output
4. All measurements with a B&K RMS meter

The power detected by the photodetector, HA, is given by Equation (31). (These parameters are also included in Table V.) Most of the values inserted into the table are known accurately, the exceptions being the actual (rather than rated) color temperature and the optical system throughput. The calculated SNR, assuming photon-noise limited operation of the SFS, is also given in Table V.

The signal-to-noise ratio measured in the laboratory breadboard will now be computed for the data in Table IV. Cases 8 and 9 give the noise-in-signal, preamp, and dark current noise for the scanned and fixed detection channels. Theoretically, the signal component should be obtainable from Cases 10 and 11. However, the spurious modulation resulting from coherence effects, reversals, and blanking in the retroreflector piezoelectric drive complicates the calculation. The signal voltage was determined by noting the ratio of signal to offset DC bias in Figures 27 and 28. Knowing the numerical value of the DC bias voltage as measured in Cases 8 and 9 permits calculation of the signal component, $I_s(t) = I_s \cos(\omega t + \phi)$. The experimentally determined signal-to-noise ratio is thus

$$\text{SNR} = \frac{\langle I_s^2(t) \rangle}{(\text{RMS Noise})^2} = \frac{I_s^2}{2(\text{RMS Noise})^2}$$

Two factors must be considered when examining the rather wide divergence between the theoretical and the experimentally measured system performance at the high SNR. The calculations required knowledge of over thirty parameters. Some of these parameters (most notably the spectral emittance and optical system throughput) are not known accurately. The other consideration requires a strict definition of "noise-in-signal". Referring to Figure 3, note that mechanical or atmospheric perturbations within the interferometer, incidence of modulated background light, or a modulated light source could modulate the signal in a manner undiscernible from the modulation resulting from the wavefront error. Since these noise sources usually are not a function of intensity, their effect becomes increasingly evident at the high SNR, where the photon noise is small. At this time, the source of the spurious noise at high SNR has not been identified.

TABLE V. BREADBOARD PARAMETERS

Parameter	Definition	Value for λ=0.84μ	Value for λ=0.50μ	Units	Reference
η_S	Quantum efficiency of Scanning Detector	0.143	0.25		Calculated from RCA data sheet, Figure 24
η_F	Same for Fixed Detector	0.068	0.12		Figure 24
λ	Wavelength	0.84×10^{-6}	0.50×10^{-6}	m	Figure 4
h	Planck's Constant	6.62×10^{-34}	6.62×10^{-34}	joule-sec	
c	Speed of light	3×10^{8}	3×10^{8}	m/sec	
B_{1F}	Electronic bandwidth	155	155	Hz	Figure 18
M	Magnification of Afocal Telescope	4	4		
T	Transmission of Beamsplitter, Retro and Telescope $0.5\times(0.85)^6$ or $0.5\times(0.90)^6$	0.189	0.266		
R	Reflection of Beamsplitter and Porro $0.07\times(0.9)^2$ or $0.07\times(0.95)^2$	0.0567	0.063		
HA	Optical power detected by PMT	1.53×10^{-10}	3.47×10^{-12}	watt	
W_λ	Spectral radiant emittance for 3300°K source at 0.84μ	5×10^{2}	78	watts/ cm^2-μm	Radiation Slide rule
$\Delta\lambda$	Optical bandwidth	0.10	0.021	μm	Figure 5
ϵ	Emissivity	0.38	0.43		Physica, 20, p. 690 (1954)
D	Effective pinhole size as demagnified by microscope 50μ/6	8.3	8.3	μm	Spec sheets

TABLE V. BREADBOARD PARAMETERS (Cont)

Parameter	Definition	Value for λ=0.84μ	Value for λ=0.50μ	Units	Reference
A	Area of pick-off mirror	4.45	4.95	mm^2	
f	Effective focal length of collimating optics	308	308	mm	
Γ	Coherence Function	0.9	0.9		
τ_1	Transmission of all relay optics	0.233	0.233		$0.7x(0.98)^8x0.85x(0.96)^2x0.5$
τ_2	Polarizer Transmission	0.4	0.4		Polaroid HN32
I_s	Signal Voltage for Scanned Channel	55	38.5	m volt	Calculated for cases 8, 9, 16 and 17. Figures 27 and 28
I_s'	Signal voltage for Fixed Channel	55	34.4	m volt	
SNR_s	Calculated signal-to-noise ratio for the Scanning Channel	700	24.9		Equation 20a
SNR_F	Same for Fixed Channel	334	12		
SNR_s'	Measured SNR for Scanned Channel	95	40.1		
SNR_F'	Measured SNR for Fixed Channel	75	14		

The close agreement between the theoretical and experimental SNR of the only situation where the RMS noise was significantly greater than 4 millivolts (Case 17 where the theoretical and experimental SNR are 12 and 14, respectively), gives us confidence that the ultimate performance of the SFS can be calculated by using signal shot noise as the limiting noise factor. Also, the difference in the performance of the SFS operating with a SNR of 700 (theoretical) or 95 (measured) becomes academic when we note from Equation (19) that even with the reduced experimental SNR the accuracy of the breadboard can theoretically approach

$$\Delta\lambda = \frac{2\lambda}{8\pi(\mathrm{SNR})} = \frac{\lambda}{1,200}$$

7.5 CALIBRATION AND TEST OF SFS

The most revealing laboratory test of the SFS breadboard is to insert a known aberrated wavefront into the SFS and compare the output of the SFS electronics against the standard error. Performing this test presents two immediate difficulties.

First, the interferometer has intrinsic aberrations resulting from the optical system design (most notably, the third order spherical in the beam expander), optical fabrication figure errors, and errors resulting from misalignment of elements that have power (parabolae of collimator and telescope). The wavefront aberrations of tilt and defocus change in time as a result of thermally induced and manually inserted translation and tilts of critical optical elements. Thus, a calibration of the SFS requires that changes in the OPD resulting from focus and tilt must be deleted from the higher order aberrations.

Second, the method used to insert a known aberration into the SFS input was to generate an aberration plate, which was placed in the collimated space immediately following the off-axis collimating parabola (Figure 30). The calibration of this plate was performed by placing the plate in an interferometer

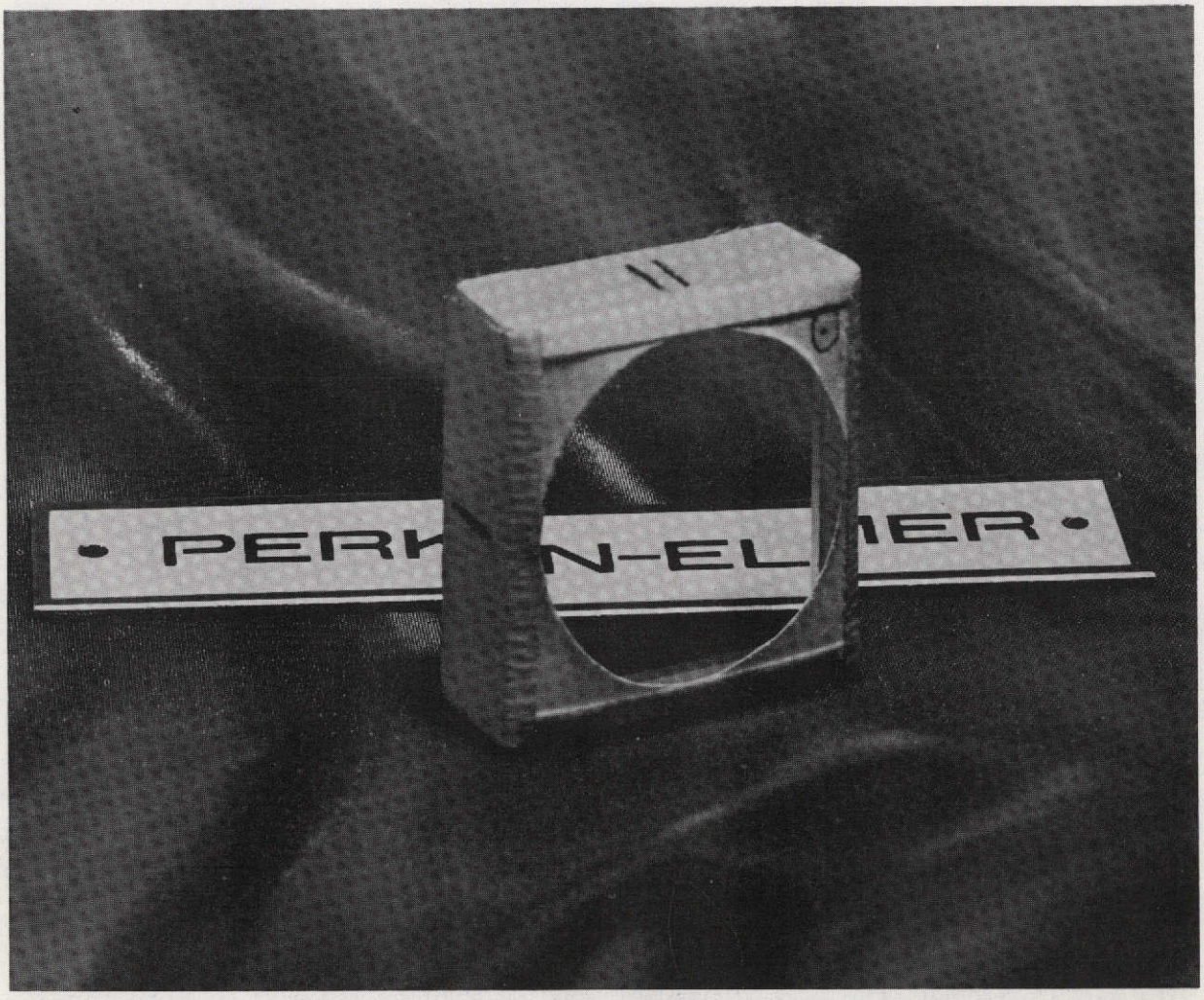

Figure 30. Aberration Plate used to test Accuracy of SFS

and photographing the resultant fringes (Figure 31). Many waves of tilt are intentionally introduced into the interferometer to generate a sufficiently large number of fringes for scanning. Thus, a comparison of the OPD data obtained from the SFS and the reference interferogram requires that the focus and tilt aberration components be reduced from the data.

Both the SFS output data and the aberration plate interferogram were analyzed by the Perkin-Elmer Modular Interferogram Program System. This system consists of a flying spot scanner (for scanning the interferograms), card reader (for input of data obtained from the SFS), and SDS 930 computer. The interferogram of Figure 31 has been "marked up" for the flying spot scanner; the heavy vertical lines showing the demarcation between fringes and the pinholes showing the position of the clear aperture of the SFS input pupil.

The SFS data was prepared for entry into the computer in the following manner. A reticle of the geometry shown in Figure 32 was fabricated and placed in the SFS output. The fixed reference detector occupied one segment of the grid. The remaining segments of the grid are sequentially interrogated by the scanning detector. The voltage output of the electronic phase detector is recorded at each location in the grid. Since the phase detection electronics were designed such that ±90 degree optical phase shift yielded a ±4 volt signal, the resultant electronic signal is simply scaled to yield the OPD in terms of optical waves.

The OPD data from the 32 locations in the grid was properly formatted on IBM cards that were subsequently entered into the SDS 930 computer. The computer program then fitted the aberration polynominals to the OPD data using a least-squared-error procedure.* The computed aberration coefficients, along with the RMS value of the higher unfitted aberration polynomials are then printed out by the computer.

---

*The mathematics and procedure for the aberration polynomial fit are discussed in detail in Section VIII.

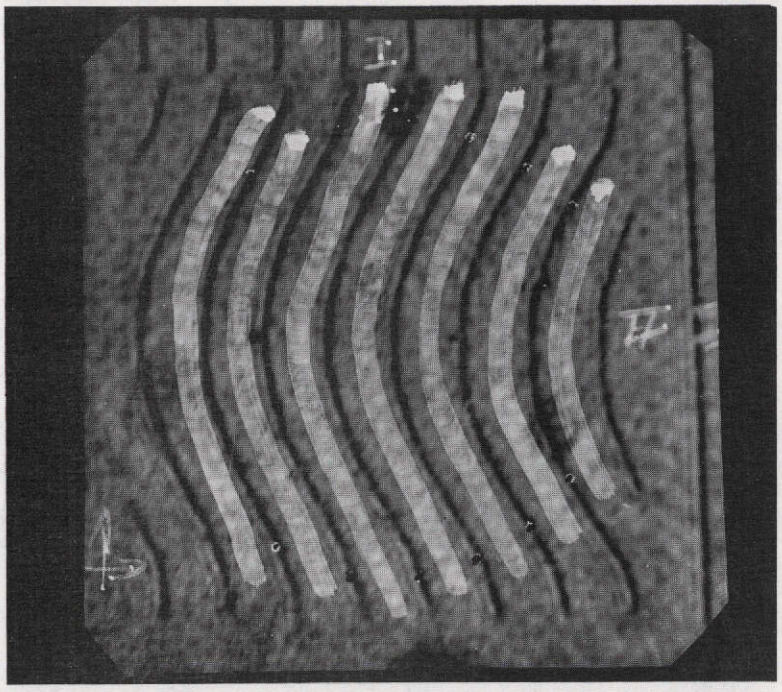

Figure 31. Aberration Plate Interferogram Marked for Scanning and Computer Processing

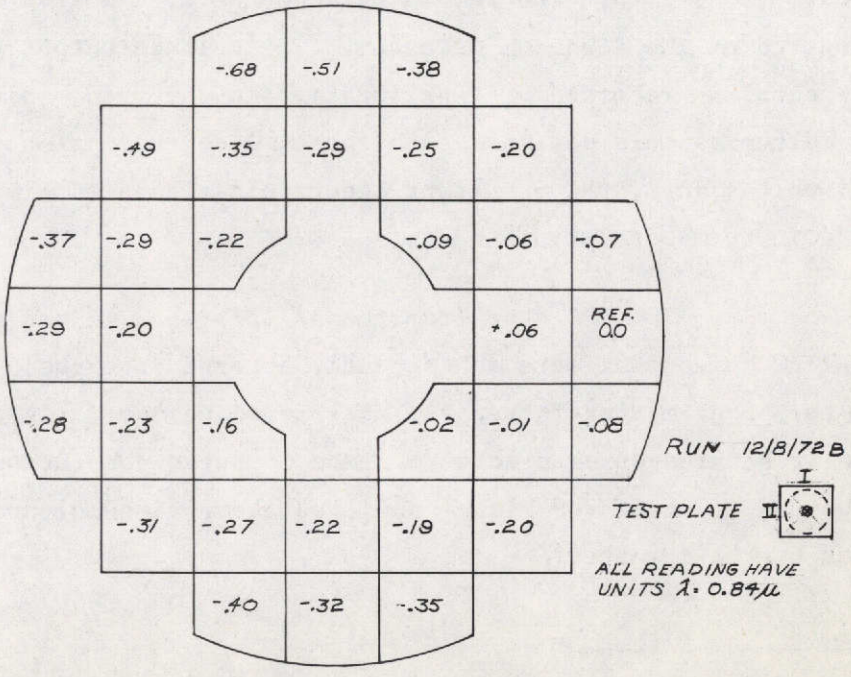

Numbers Represent OPD Readings of the Aberrated Wavefront as Measured by Electronic Phase Detector

Figure 32. Geometry of Reticle in SFS Output

TABLE VI. COMPILATION OF CALIBRATION AND TEST AGAINST ABERRATION PLATE

	FOCUS	0° ASTIG	45° ASTIG	X-COMA	Y-COMA	3RD SPHERICAL	X-CLOVER	Y-CLOVER
AVERAGE OF 4 CALIBRATION RUNS FOR EMPTY SFS	-0.08	-0.04	-0.13	-0.07	-0.03	-0.12	0.02	0.04
STANDARD DEVIATION OF DATA FOR ABOVE RUNS	0.01	0.01	0.01	0.03	0.04	0.09	0.01	0.01
AVERAGE FOR 2 RUNS WITH ABERRATION PLATE AND COMPENSATED FOR SFS ABERRATIONS	-0.28	0.25	0.06	-0.02	0.06	0.23	-0.01	-0.03
INTERFEROGRAM REDUCTION		0.29	0.01	-0.07	0.06	0.22	-0.02	-0.02

ALL ENTRIES HAVE UNITS OF WAVES, $\lambda = 0.84\mu$

The data from six runs — four with the interferometer empty and two with the aberration plate in the SFS input — was reduced with results as tabulated in Table VI. The first six columns represent the well-known Seidel aberrations, while the last two columns represent aberrations of the form $r^3 \cos 3\theta$ and $r^3 \sin 3\theta$, respectively. A visualization of the shape of such a wavefront indicates why this higher order aberration has been given the name, Clover. It has been included in the data reduction to demonstrate that the SFS is capable of measuring aberrations of higher order than the classical Seidel aberrations.

The first row in Table VI gives the average results of four calibration runs of the SFS. The focus, astigmatism, and coma aberrations intrinsic to the SFS are believed to originate primarily from the collimating off-axis parabola. In an operational system, these residual aberrations could be reduced by the use of data similar to that in Table VI to align the SFS collimating optics optimally. A defocus of the expander telescope in the retroreflector arm of the SFS will also give rise to a defocus in the output OPD map. It will be shown in Section VIII that the focus aberration coefficient is utilized when the SFS is used to generate error signals for the alignment of the secondary mirror. Thus, it is important to determine whether the defocus results from the collimating optics or from the expander telescope in any calibration of the SFS.

The third order spherical aberration results predominantly from the secondary mirror of the expander telescope. Because of cost and schedule considerations, the secondary mirror was not aspherized, but was designed to the nearest fitting spherical surface. The residual spherical aberration of 0.12 wave agrees well with that expected from the optical design.

The repeatability of the procedure for obtaining an OPD map of the SFS output and polynomial fitting by the computer is obtained by calculating the standard deviation of the experimental data. The unbiased maximum-likelihood estimation of the variance is (Ref. 8).

$$\sigma^2 = \frac{1}{n-1} \sum_{i=1}^{n} (x_i - \bar{x})^2$$

where x_i = data readings

n = number of data samples

$\bar{x}$ = average of data

The standard deviation is obtained by taking the positive square root of the variance. Note that the standard deviation increases for the higher order aberrations. This results from an undersampling of the SFS exit pupil in the present experiments. An automated and calibrated scan system would permit acquisition of data at more locations in the pupil, thus introducing the required additional data redundancy to increase the accuracy of the SFS data reduction.

The test aberration plate was placed in the interferometer input and the OPD output data was recorded. Two test runs were performed with the aberration plate rotated 180 degrees between the runs. The data was compensated by subtracting the intrinsic aberrations as listed in row 1 of Table VI. The residual aberrations for the two runs are averaged and the resultant number is then assumed to represent the aberrations resulting from the test plate. These computed values are listed in row 3.

An independent check of the aberrations of the test plate was obtained from the interferogram of the test plate (Figure 31). The interferogram was scanned on a flying spot scanner and the resultant data was reduced by the SDS 930 computer to obtain the least square polynomial fit to the data.

A comparison of the last two rows of Table VI gives the accuracy of the SFS when measuring an aberrated wavefront. The focus term was not readily available from the data reduction of the interferogram. However, since we know that the aberration plate was fabricated by polishing a cylindrical surface on one side of an otherwise perfect window, the defocus magnitude should be numerically equal to the magnitude of the induced astigmatism. The data in row 3 verifies the magnitude and the sign of the focus term.

The largest deviation between the SFS output and interferogram is $\lambda/20$. The error is believed to originate from the following considerations:

(a) Undersampling of the exit pupil

(b) Nonlinearities and instabilities of the phase detector

(c) Inaccurate positioning of the pick-off mirrors for the PMT

(d) Ambiguities when OPD reading is near $\pm\lambda/4$ points

These rather minor considerations simply require upgrading of the detection and output processing of the photodetector output electronic signals. The following redesign tasks could easily upgrade the SFS to a performance level where the interferometer sensitivity would approach the target level of $\lambda/100$.

- Automate the exit pupil sampling procedure with the sample coordinates being remotely monitored either in digital or analog form

- Upgrade the present phase measuring electronics or possibly operate the SFS in a white light fringe mode.

7.6 LONG-TERM STABILITY

The stability and accuracy of the SFS optical system is verified by two means. First, the SFS is highly repeatable as seen from the experimental data of row 2, Table VI. The repeatability of the lower order aberrations was typically $\lambda/100$. A second measure of the long-term stability is obtained by noting the phase deviations between the two output electrical channels. This is most easily implemented by using the two electrical sinusoidal signals to drive the X and Y oscilloscope axes and thus generate a Lissajous figure. The figure is always an ellipse whose ellipticity changes as phase errors occur between the two SFS output signals. Figure 33 is a picture of a 20 minute time exposure of the Lissajous figure. The width of the curve results from the small sinusoidal envelope modulation traceable to coherence effects (Figure 5). Instability of the SFS would result in a change in the shape of the ellipse. Thus the laboratory experiments have indicated that the SFS remains stable to typically $\lambda/100$ over periods exceeding twenty minutes.

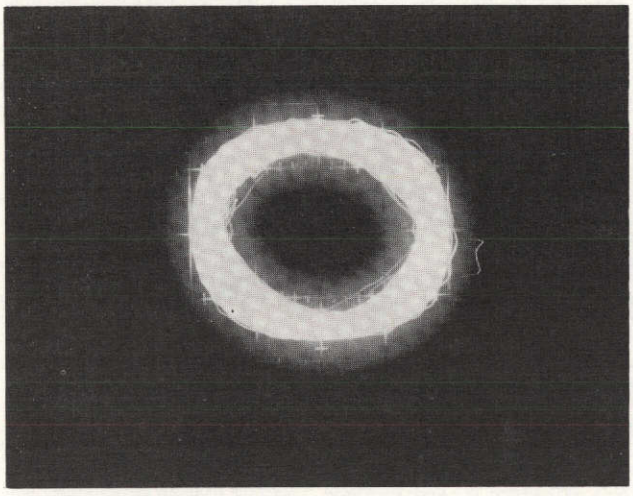

20 minute time exposure of the Lissajous Figure formed between two photodetector sinusoidal outputs.

Figure 33. Lissajous Figure Indicating Long-Term Stability of SFS

SECTION VIII

CONCEPTUAL DESIGN

8.1 INTRODUCTION

The Stellar Figure Sensor (SFS) will be an integral subsystem in a very complex space optical system such as the LST. Thus, it is critical to define at the earliest possible time both the functional requirements of the SFS and the requirements of all other subsystems that must interface with the SFS, the requirements of the telescope optical subsystem (which is the source of the wavefront errors detected by the SFS), and those of the computer subsystem (which reduces the digital data contained in the SFS output). From the functional requirements it is possible to derive the operational requirements for the interferometer.

Before discussing the interfacing of the SFS with the main telescope, a strict definition of the interfaces must be made. The input interface for the figure sensor is located at the focal plane of the telescope and the output interface of the SFS follows the location where the optical path difference (OPD) map is generated, as shown in Figure 34. The hardware activity of the contract was limited to the functions performed between interfaces A and B. In the breadboard experiments, the telescope was simulated by a back-illuminated pinhole at the focus of an off-axis parabola. The introduction of aberrations by the telescope was simulated by inserting an aberration plate containing a known aberration (predominately astigmatism) in the SFS input. The data representing the output OPD Map was entered onto IBM cards which were subsequently processed by the Perkin-Elmer MIP system. (Ref. 9) Thus, most of the functions discussed in this section have been simulated in the processing of the data obtained from the laboratory experiments (although not always on a real-time basis).

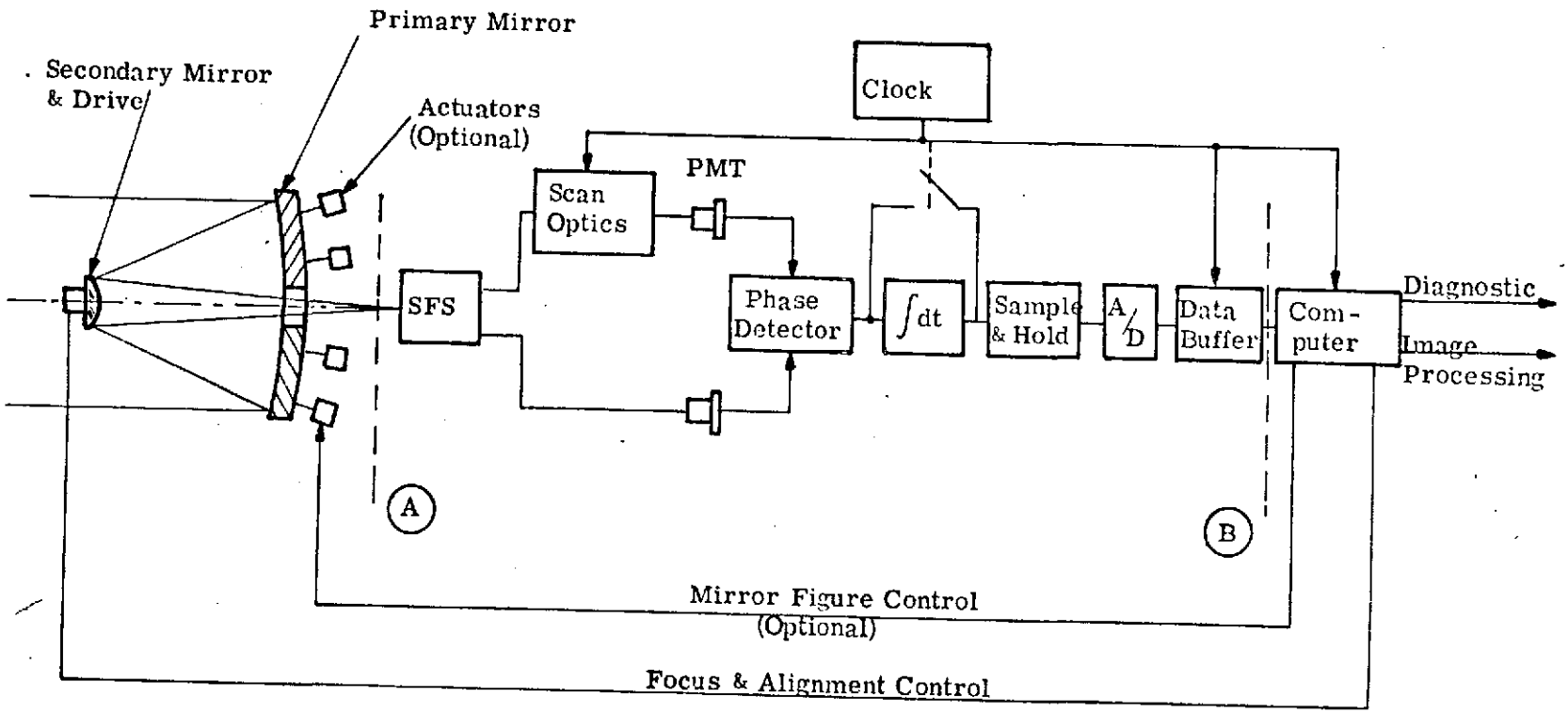

Figure 34. Functional Schematic for LST - Utilizing a Focal Plane Figure Sensor

8.2 FUNCTIONAL REPRESENTATION OF TELESCOPE OPTICAL SYSTEM*

Since the optical and structural designs of the LST Breadboard and the LST are not finalized, it is premature to define the exact alignment requirements of the telescopes. However, careful study of the typical optical characteristics and mechanical degrees of freedom of large telescopes provides considerable insight into the requirements that will probably be imposed upon the SFS. In general, it is expected that the SFS will be required to provide data to control: focus, secondary mirror tilt and translation, and possibly control of the Primary Mirror Optical Figure. To demonstrate the capabilities of the SFS, the amount of information obtainable from a single interferogram generated from starlight at a given position in the field at the focal plane is considered first. This analysis is later extended to include the additional information derived by evaluating interferograms from multiple points in the field.

Wavefront aberration may be described as a function of three variables: h, x, and y or h, r and θ, where h is the field dependent term and the remaining parameters define the location in the pupil in cartesian or cylindrical coordinates.

$$r^2_{max} = (x^2 + y^2)_{max} = 1, \text{ and } h^2_{max} = 1.$$

The pupil coordinates, x and y, form a complete basis:

$$1;\ x,\ y;\ x^2,\ xy,\ y^2;\ x^3,\ x^2y,\ xy^2,\ y^3;\ x^4,\ x^3y,\ x^2y^2,\ xy^3,\ y^4;\ \text{etc.}$$

From symmetry arguments (Ref. 1), for a rotationally symmetric optical system, the field variable h combines with the pupil coordinates as $h^\ell x^m y^n$, such that $\ell + m + n$ is an even number.

From the basis $h^\ell x^m y^n$, various linear combinations may be formed. The classical combination is of the form (h^{2n}, r^{2n}, $h^n r^n \cos^n \theta$). Another common form is (h^{2n}, r^{2n}, $h^n r^n \cos n\theta$) where the functions are now orthogonal in θ. The Zernike polynomial form suppresses the field dependence in the

*Much of the data presented in this section was derived by Dr. R.E. Hufnagel and J.S. Patterson of the Perkin-Elmer Corporation.

functions, and places it implicitly in the coefficients preceding the functions ($f(n,r)\cos n\theta$). These functions are orthogonal both in r and θ. The dependence on h, regardless of whether it is in the functions themselves or in the coefficients, must obey the same rules of symmetry. For instance, the coefficient preceding the functions $(x^2 + y^2)^2$ must be of the form

$$B_0 + B_1 h^2 + B_2 h^4 + \ldots;$$

i.e., it must be an even function of h.

The field dependent relationships for the wavefront aberration thus developed, refers only to wavefront errors intrinsic to the optical system; that is, resulting from the optical design. Next, the field dependence of the aberrations resulting from other sources, such as misalignment of the elements and fabrication errors, are evaluated.

When an optical system is perturbed by tilting or decentering one or more of its elements, it is the exit pupil wavefront, W(x,y,h) (where x,y are exit pupil coordinates and h specifies field position), that is operated upon. The exit wavefront can be written in an expansion of the form

$$W(x,y,h) = \sum_n \sum_i [A_{in}(h)\, P_i(x,y)]$$

where $P_i(x,y)$ is the i'th aberration polynomial, and the $A_{in}(h)$ describes the contribution that the n'th element makes to the i'th polynomial.

The perturbed system wavefront can now be described to the first order as

$$W(x,y,h) = \sum \sum \left\{A_{in}(h) \left[P_i(x,y) + \frac{\partial P_i}{\partial x}(x,y)\, \delta x_n + \frac{\partial P_i}{\partial y}(x,y)\, \delta y_n\right]\right.$$

The aberration associated with an x-perturbation is

$$\delta W = A[x(x^2+y^2)]\,[4\delta x]$$

This represents "x-coma" of magnitude $4A_3x$, but is different from any coma originally in the system in that the field angle dependence is of opposite parity; i.e., the original coma had a dependence of the form $(A_1h_x+A_3h_x^3+...)$, by the symmetry arguments previously presented.

Similarly, the components for all other aberrations attributable to tilts and decenters are of opposite parity to that in the design of the system; or the aberration is one that is not allowed in the design. Therefore, for allowed aberrations, if the perturbation decreases the total magnitude of an aberration at one field angle, it will then increase the magnitude at the opposite field angle. Knowledge of change in the aberration coefficients resulting from the tilt and decenter alignment errors allows calculating the control signals for the secondary mirror from the interferometric data taken at multiple field positions. The data is analyzed into its component aberrations and each component is then separated into its odd and even portions, i.e., its design and its perturbations contributions.

The above discussion demonstrates that a procedure does exist for separating the aberration components resulting from misalignment and the intrinsic aberrations resulting from the optical design of any multielement optical system if the system is circularly symmetric. This allows the SFS to be placed behind field corrector plates or following relay optics of the telescope, if desired.

In a general sense, the number of field positions in the telescope focal plane that must be interrogated is a function of the telescope optical design and the perturbation. The expansion of the field dependence for each aberration is truncated at N terms, as is the orthogonal field dependence. Thus, 2N or 2N-1 points in the field must be interrogated to obtain the field dependence of the given aberration for aberrations that have odd and even field dependence, respectively. For the Cassegrain or Gregorian telescope design, the odd-field dependent coma contributions are known from the optical design. The only significant coma introduced by misalignment is field independent, since all the remaining field dependent coma terms are insignificant, which infers that N=1. Thus, sampling of only 2N-1=1 field position is required to determine the unknown coma field depencence resulting from secondary misalignment.

Aberrations resulting from physical deformation of the optics (for example, the LST primary) will be field independent when the field is suitably small. However, if the aberration component is generated by misalignment of the optics and is also field independent, it is impossible to distinguish the source of the error. This separation of misalignment and primary mirror figure errors is rather pedantic since the aberration could be corrected either by realignment of the optical system (assuming this does not introduce other significant aberrations) or by correcting the figure of the element in question. Thus, there is a limited redundancy in the procedure used to correct some of the lower-order aberrations.

The above analysis is significantly simplified if the optical system is limited to a two-conic reflecting aplanat, such as the classic Cassegrain, Gregorian, and Ritchey-Chretien astronomical telescope designs. The analysis of such two-element systems is sufficiently simplified that a linear relationship between the measured aberrations and the required angular and translational control signals to the secondary mirror alignment actuator can be derived. Also, the minimum number of field positions that must be interrogated is reduced to three. The only "cost" for these advantages is that the SFS must operate in the telescope focal plane at locations in the field that are not operated upon by auxiliary optics such as corrector plates or relay optics. The derivation of these control equations is contained later in this section.

One final point should be considered in defining the operational requirements of the SFS as determined by the telescope optical system; What is the reduction in system performance, as measured by Strehl ratio, when a known amount of a given aberration is introduced into the system? This information is very useful in determining the required sensitivity of the SFS to a given aberration. The three curves of Figure 35 denoted "static" define the loss in Strehl as a given aberration is introduced (Ref. 10). The remaining curves denoted "compensated" define the loss in Strehl <u>if the given aberration</u> is <u>balanced</u> with the named aberration. These curves would be of interest if we were attempting to balance an aberration intrinsic to the primary (say astigmatism) with the best possible refocus. The curves are also of interest because

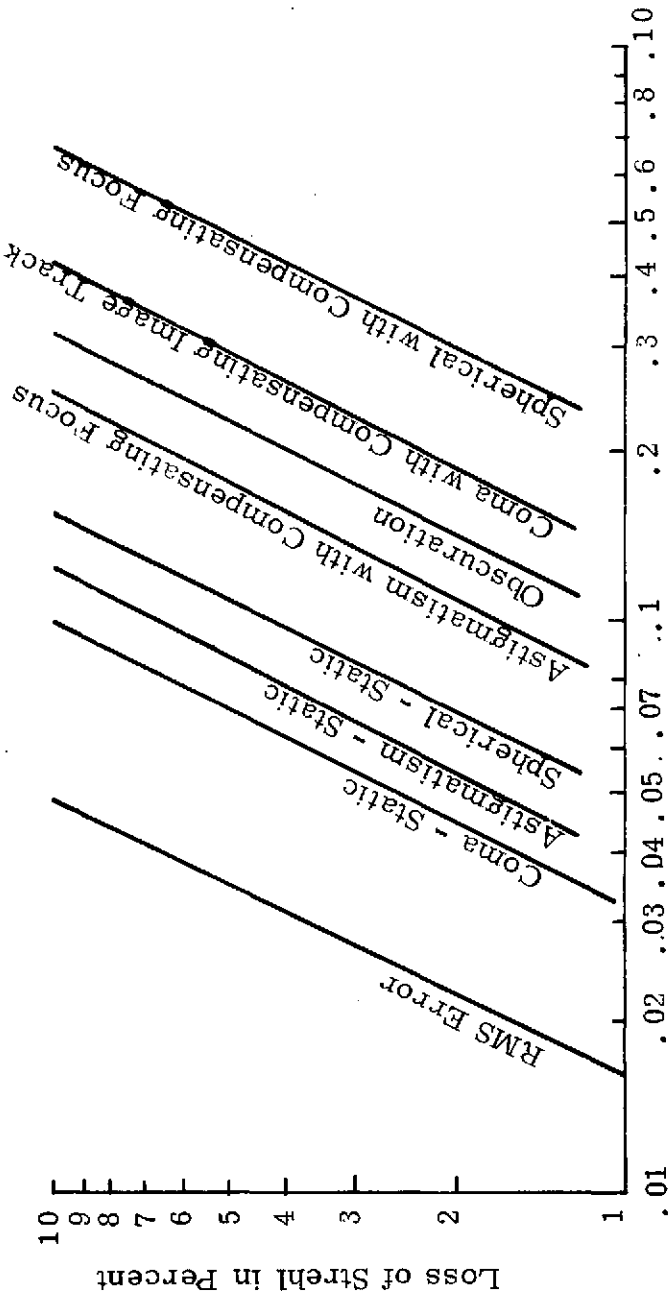

Figure 35. Degradation of Strehl Related to Combinations of Aberrations

they indicate that even 0.2λ of spherical aberration (with best possible refocus) reduces the Strehl ratio by only 1 percent.

8.3 FUNCTIONAL REQUIREMENTS OF COMPUTER PROCESSING

The SFS operates on the data from only a single field position while generating any given OPD map. Thus, the polynomial representation of the aberrated wavefront, as detected by the SFS, can be defined by suppressing the h dependence in Equation (32).

$$W(x,y) = \sum_{i=1}^{\infty} P_i(x,y) \tag{34}$$

The $P_i(x,y)$ are often defined in terms of the Seidel or Zernike polynomials. The Zernike polynomials have the advantage that they are orthogonal over a unit circle. This means that for a clear aperture the aberration coefficients are independent of each other. If the interferogram OPD were known everywhere throughout the aperture, the aberration coefficients would be found by integration in the usual way for orthogonal functions. In practice, OPDs are known only at discrete points. The equivalent of integration is then to best-fit the function to the experimental OPDs in an rms sense, minimizing the sum of squares of the residuals between the function and the OPDs. Sometimes the data points are not equally spaced and often do not extend throughout the aperture. Now, unfortunately, the aberration functions are no longer orthogonal, and therefore not completely independent of each other. This means, for instance, that the amount of coma that can be removed from the set of OPDs is influenced slightly by whether or not some other aberration such as astigmatism is also being removed.

As orthogonality is the exception rather than the rule for interferogram analysis, it is worthwhile to simplify the polynomial expansion for numerical work. One variant of the Zernike expansion consists of a simple series of power terms of the form $r^n \begin{matrix}\cos \\ \sin\end{matrix} m\theta$. This is more convenient for calculation, and if desired, any particular Zernike polynomial can be constructed from a linear combination of terms of the same and lower orders from the modified series. Thus, a simultaneous fit of other lower order terms, as well as the required one, is necessary.

In the computer programs written for the evaluation of optical systems (which includes the programs for interferogram data analysis), the definition of the Zernike polynomials differs slightly from that of Born and Wolf (Ref. 1). The conventional Zernike polynomial is normalized for a peak value of 1, where for the purposes of this report they are redefined for a mean squared average value of 1, and a single subscript notation is used. In this case the wavefront W(x,y) is expanded into the infinite series of modified Zernike polynomials as in Equation (34) where $P_i(x,y)$ are now the modified Zernike polynomials. The first 11 polynomials of this expansion are listed in Table VII. This is the maximum number of polynomials that can be reliably fitted to the wavefront, which has been sampled at a density comparable to Figure 32.

The least-squares criterion requires the quantity E to be minimized, where

$$E = \sum_{m=1}^{M} \left[W_m(x,y)_m - \sum_{i=1}^{I} A_i P_i(x,y)_m \right]^2 \qquad (35)$$

where $W_m(x,y)_m$ is the optical path difference at the m'th data point $(x,y)_m$, and the P_i are the polynomials describing the aberrations.

The minimization of E requires the solution of I simultaneous equations:

$$\frac{\partial E}{\partial A_i} = 0 \qquad (36)$$

The equation may be expressed in matrix form:

$$B_{ki} \; A_i = q_k \qquad (37)$$

where

$$B_{ki} = \sum_{m=1}^{M} P_k(x,y)_m \; P_i(x,y)_m = B_{ik}$$

and

$$q_k = \sum_{m=1}^{M} W_m(x,y)_m \; P_k(x,y)_m$$

TABLE VII. MODIFIED ZERNIKE POLYNOMIAL

Modified Polynomial	Polar Coordinates	Rectangular Coordinates	Aberration Designation
A_1	1	1	Constant
A_2	$2r \cos \theta$	$2x$	x-tilt
A_3	$2r \sin \theta$	$2y$	y-tilt
A_4	$3 (2r^2-1)$	$3 (2r^2-1)$	Focus
A_5	$6\ r^2 \sin 2\theta$	$6\ 2xy$	45° astigmatism
A_6	$6\ r^2 \cos 2\theta$	$6 (x^2-y^2)$	0° astigmatism
A_7	$8 (3r^2-2r) \sin \theta$	$8\ y (3r^2-2)$	y-coma
A_8	$8 (3r^2-2r) \cos \theta$	$8\ x (3r^2-2)$	x-coma
A_9	$8\ r^3 \sin 3\theta$	$8\ y (3x^2-y^2)$	y-clover
A_{10}	$8\ r^3 \cos 3\theta$	$8\ x (x^2-3y^2)$	x-clover
A_{11}	$5 (6r^4-6r^2+1)$	$5 (6r^4-6r^2+1)$	3rd-order spherical aberration

The solution is $A_i = (B_{ki})^{-1} q_k$ and the resulting analytic wavefront is described by

$$\tilde{W}(x,y) = \sum_{i=1}^{I} A_i P_i (x,y) \tag{38}$$

The definition of $P_1 = 1$ allows E to be correctly optimized about the mean value.

Empirically, for typical high quality, large aperture telescopes it has been found that the polynomials of Table VII are able to reduce the maximum (residual) difference at any point between the input wavefront and the analytic wavefront to about 0.001λ for the class of systems with $\lambda/10$ rms wavefront variations.

A given value A_i gives the magnitude of its associated aberration resulting from misalignment, intrinsic optical design aberrations, and distortion of the optics at a single field position. Reintroducing the field dependence that was suppressed in the preceding analysis, the analytic wavefront at field position h_j is

$$\tilde{W}(x,y,h_j) = \sum_{i=1}^{I} A_i(h_j) P_i (x,y) \tag{39}$$

In general, the control equations for tilt (ϕ_x and ϕ_y) and translation (Δx, Δy) correction of the secondary are written functionally in terms of $A_i(h_j)$, all i and j. However, experience has shown that even many-element systems, when perturbed by misalignment, have a wavefront degradation that is closely expressible by coma, astigmatism, and defocus. Knowledge of the optical design permits an analytical or numerical derivation of the required functional relationships between Δx, Δy, ϕ_x, ϕ_y and the aberration coefficients $A_i(h_j)$. This relationship is easily derived for a telescope consisting of two reflecting conics such as the Cassegrain or Gregorian Telescope.

The wavefront error introduced by a lateral displacement Δy of the secondary is (from Ref. 11)

$$\delta W_{dy} = 2c_s \Delta y \{y - A\rho^2 y/2\} = 2c_s \rho \sin\theta \Delta y - Ac_s \rho^3 \sin\theta \Delta y \quad (40)$$

where c_s = vertex curvature of the secondary mirror

$$A = (1/d - c_s)^2 + (1-k) c_s^2$$

d = focal plane to secondary vertex distance

k = conic constant

Similarly, the orthogonal displacement yields

$$\delta W_{dx} = 2c_s \rho \cos\theta \Delta x - Ac_s \rho^3 \cos\theta \Delta x$$

These equations, derived from third-order aberration theory, state that lateral translation of the secondary yields both coma and a wavefront tilt which is linear with the perturbation. The wavefront error resulting from both a Δx and Δy translation is computed by the addition of the two components.

$$\delta W_d = 2c_s \rho [\sin\theta \Delta\rho \sin\Theta + \cos\theta \Delta\rho \cos\Theta] \quad (41)$$

$$- Ac_s\rho^3 [\sin\theta \Delta\rho \sin\Theta + \cos\theta \Delta\rho \cos\Theta]$$

$$= 2 c_s\rho \Delta\rho \cos(\theta - \Theta) - Ac_s\rho^3 \Delta\rho \cos(\theta - \Theta)$$

where

$$\Delta\rho^2 = \Delta x^2 + \Delta y^2$$

$$\tan\Theta = \Delta y/\Delta x$$

The tilt term of equation (41) causes a translation of the image. If some absolute reference were available, the resultant mispointing could be measured and the data used to generate the required control signals. However, since no absolute reference exists (i.e., it is not known whether the image translation resulted from mispointing or secondary mirror tranlation) only the coma term is of interest.

The data lost by not having available the absolute pointing information is still required. This information can be obtained by measuring the tilt of the best focus image plane at the Cassegrain focus as the misalignment of the telescope causes the image plane to tilt as well as to translate.

As an analytic aid, the tilt of the secondary mirror may be defined as a rotation about any convenient point along the telescope optic axis. This choice naturally will affect the measure of translation in a given misaligned condition. The most convenient point of rotation for this analysis is the secondary mirrors "neutral point", defined as the point of rotation about which the coma contributions from all sources cancel for the axial image point resulting in a coma-free image (ref: 11).

A tilt of the secondary mirror through an angle ϕ_x about the neutral point gives rise to a tilt of the Cassegrain focal plane of $m\phi_x$, where m is the magnification of the secondary. Assuming an arrangement of focus sensors as shown in Figure 36 this tilt of the focal plane will be measured as the shift of the best focused image from the nominal or design location, Z_o, as;

$$m\varphi_x = \frac{\Delta Z(X_o,0) - \Delta Z(-X_o, 0)}{2X_o} \tag{42}$$

Stating the focus shift in terms of wavefront curvature, W_{20}, (Ref: 11)

$$\Delta Z = 8\lambda N^2 W_{20}, \tag{43}$$

which infers

$$\varphi_x = \frac{\Delta\lambda N^2}{mX_o}\left[W_{20}(X_o,0) - W_{20}(-X_o,0)\right] \tag{44}$$

Since rotation about the neutral point does not introduce coma, equation (41) may be used directly to calculate the relation between the secondary translation ΔX and the coma coefficient, W_{31} (assuming an aplanatic system) which is simply

$$\Delta X = W_{31X} \Big/ (Ac_s) \tag{45}$$

The equations for the y component follow by inspection,

$$\varphi_y = \frac{\Delta\lambda N^2}{my_o} \left[W_{20}(0, y_o) - W_{20}(0, -y_o) \right] \tag{46}$$

$$\Delta_y = W_{31y} \Big/ (Ac_s) \tag{47}$$

The aberration coefficients Wijk must be related to the coefficients of the Modified Zernike Coefficients A_1 to A_{11} of Table VII if the secondary mirror control loop is to be implemented. The coefficients A_I to A_{II} obtained by the computer operation on the OPD map generated by the SFS contain the wavefront error contributions resulting from misalignment as well as the intrinsic optical design aberrations.

For the case of the Ritchey-Chretien telescope (which we recall is corrected for coma at all points in the field),

$$W_{31x} = A_8/24 \tag{48}$$

$$W_{31y} = A_7/24 \tag{49}$$

An additional complication is that the image plane of the Ritchey-Chretien telescope has curvature. This did not affect us in the previous calculation since we were examining the tilt of the focal plane, and contributions to defocus resulting from image plane curvatures are self compensated. Thus, even when the telescope is at optimum focus and alignment, a typical height in the field (h) will have a defocus component which we define as W_{20} (h). Recalling equation (43), the shift in the focal plane as sensed by the focus sensors is

$$\Delta Z = 4\lambda N^2 \left[\frac{W_{20}(X_o,0) + W_{20}(-X_o, 0)}{X_o} - 2W_{20}(h) \right] \tag{50}$$

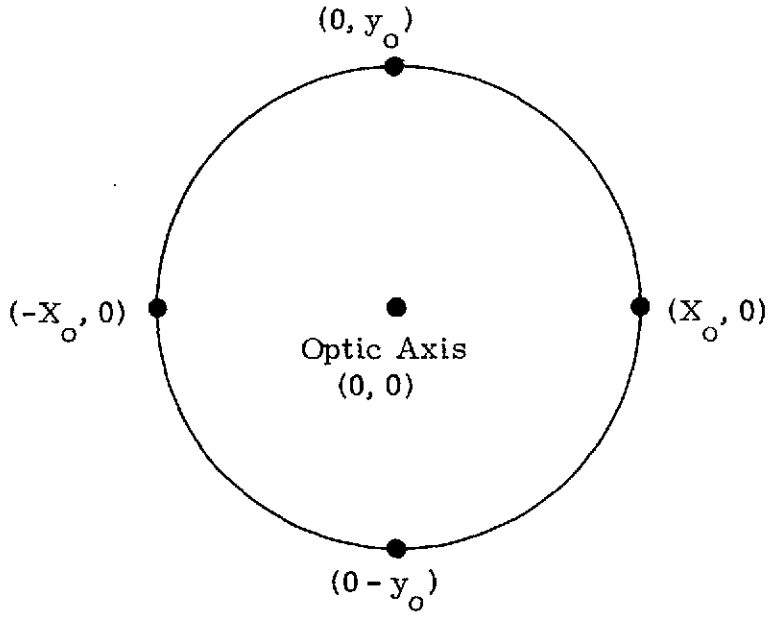

Figure 36. Possible Location of Focus Sensors in Field

The control signal for the secondary mirror focus is

$$\Delta S = -\Delta Z/m^2 \tag{50}$$

where

ΔS = axial displacement of the secondary and is positive as the mirror separation increases

ΔZ = shift of principal focus paraxial image

m = secondary magnification

the control equations for the secondary mirror focus motion, thus, is

$$\Delta S = 4\lambda N^2 \left[\frac{W_{20}(X_o, 0) + W_{20}(-X_o, 0)}{X_o} - 2W_{20}(h) \right] \Big/ m^2 \tag{51}$$

8.4 IMPLEMENTATION OF CONTROL EQUATIONS

The flow diagram showing the procedure for converting the SFS output OPD map into the secondary mirror control signals, as well as the method for generating the control signals for an Active Optics deformable primary mirror, is shown in Figure 37. The breadboard developed during this program generates a voltage at the output of the phase detector that is proportional to the wavefront error at the given pupil position. A method for automating the acquisition of the OPD data is shown in Figure 34. The "integrate, sample and hold" circuit generates a voltage proportional to the average voltage of the phase detector output over the integration period. This operation is equivalent to a low-pass filtering of the phase detector output. This signal is converted to a digital signal that, along with the digitized pupil position, is stored in a data buffer in the computer input/output interface logic. The interface between the SFS and computer subsystem is located at the output of this data buffer.

The computer processing may be performed by a slaved special purpose minicomputer or by a larger time-shared computer, either of which would probably be located in the telescope. On command, the OPD map array would be read from the buffer. The matrix operations on this array of data to generate the required polynomial coefficients A_1 through A_{11}, are stated in Equation (38). These coefficients are then corrected for the minor errors resulting from the geometric sizes of the SFS reference beam and detectors. (See Table I and Figure 9.) The next function is the removal of the optical design aberration effects from the aberration coefficients, which requires access to a read-only memory containing a table of the telescope design aberrations for the field position(s) that is interrogated.

The resultant polynomial coefficients state the telescope wavefront error arising from misalignment of the secondary mirror or by deformation of the optics. For Cassegrain and Gregorian Telescopes, the field independent coma, defocus and wavefront tilt can be completely corrected by motion of the secondary. All other aberration coefficients are only correctable (at least partially) by an Active Optics deformable primary.

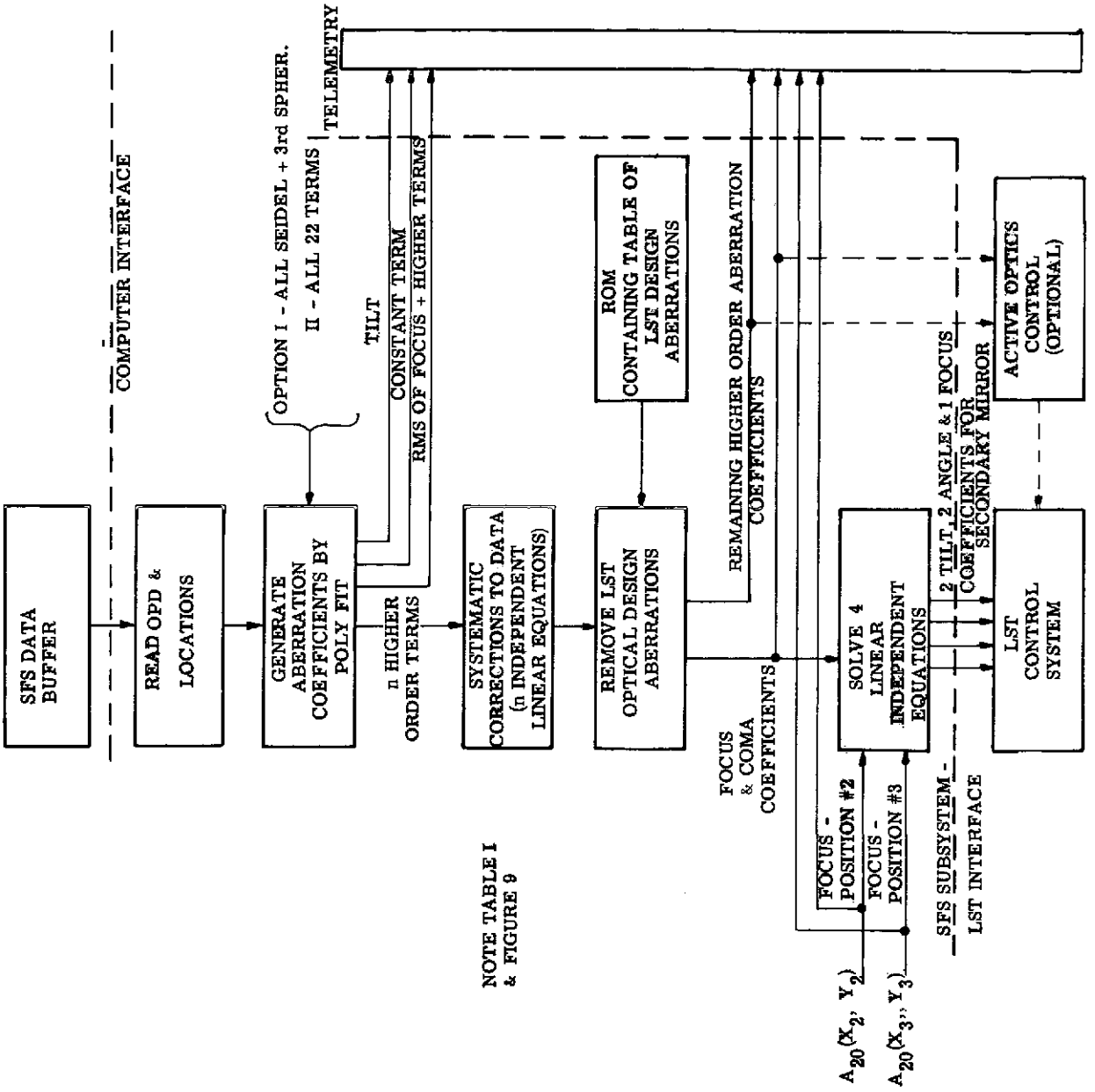

Figure 37. Secondary Mirror and Active Optics Control Logic

The last function to be performed by the computer program is to solve the focus, tilt, and lateral translation control equations stated in Equations (47) and (53). Note that focus information from at least two other field positions is required for this function, as shown by the control equations.

To estimate the computational time and complexity of computer, each function of Figure 37 is listed along with the mathematical calculations, storage requirements, and number of computer operations (typically multiply or divide). Refer to Table VIII. Note that the compute time is strongly influenced by the number of polynomials to be fitted to the wavefront. If the SFS is to be used only as an alignment tool, only focus and coma information would be required, thus permitting a minimum value of $n = 8$. A value of $N = 11$ will yield all the Seidel aberrations as well as third order spherical observation. For the case $n = 11$, all computer calculations could be performed in a period of approximately 0.2 second, if a typical multiplication required 200 μseconds and $M = 35$. Thus, we see that a slaved special purpose mini-computer or a time-shared general purpose digital computer should be adequate at least for the computations necessary to obtain the secondary focus, translation, and tilt error control signals. Further study is required to consider the impact on the computer processing if the computer is also to be used to generate the error signals for an active control of the primary mirror.

TABLE VIII. COMPENDIUM OF COMPUTER OPERATIONS

M = Number of points in pupil
n = Number of polynomials fitted to wavefront

Function	Calculation	Reference	Storage Locations	No. of Computer Operations
Generate Aberration Coefficients	Read OPD Array and Locations	3M	3M	
	Calculate Aberration Polynomials for each point			31 for n=23 polynomials 12 for Seidel Aberrations plus 3rd order spherical (n=11)
	Accumulate to form Matrix B_{ki} and vector A_i	Equation (37)	$1/2n\ (n+1) + n$	Mn
	Solve for A_i by Cholesky Method	Equation (38)		$\frac{n^3}{6} + \frac{3n^2}{2} + \frac{n}{3}$ multiply/divide n square roots error $\leq a\ 10^{1-t}(2n^2+3n^3)$ $a = \max \lvert b_{ki} \rvert$ t = number of digits
Systematic and optical design aberrations removed	Correct Aberration Coefficients	Figure 9 Table I	2n	n subtractions
Generate Control Signals	Solve 5 linear independent equations	Equations (47) (53)	5	Subtractions Trig. functions

SECTION IX

SCIENTIFIC USES OF SFS

The primary function of the Stellar Figure Sensor is to interrogate the stellar wavefront at the LST focal plane in order to determine the control signals for positioning the secondary mirror and deforming the primary mirror figure. The preceding eight sections presented analytical and experimental verification that the SFS fulfills this functional requirement. This section will present a number of scientific experiments which may be performed that utilize the SFS with no change in the interferometer optical design and only minor modifications of the output data handling. We wish to thank John Mangus, Dr. Ken Hallum, and Ed Chin of Goddard Space Flight Center for initially suggesting the idea of using the SFS for applications other than the primary role of wavefront interferometry.

The alternate scientific applications of the SFS identified to date are:

(1) Coherence measurements on nearly resolvable sources.

(2) Generation of optical spectra of the source by operating the SFS as a Fourier Spectrometer.

(3) LST Optical Transfer Function Sensor which generates input for post exposure image processing.

(4) Extended source interferometry.

(5) Absolute photometry.

(6) Operation in an earth observing mode using a ground based laser as a source to obtain coherence measurements of atmosphere.

(7) Utilize SFS in ground based telescopes for alignment and atmospheric experiments.

Each of these peripheral applications will be briefly discussed in this section. The authors welcome any comments or suggestions from interested parties on extensions of the above or other new applications.

9.1 COHERENCE MEASUREMENTS

The envelope modulation of the PMT output sinusoidal electrical signal is influenced by both the relationship of the optical filter-optical path difference between the interferometer arms and the spatial coherence of the source. Earlier discussions have primarily been concerned with the effects of the envelope modulation, resulting from the translation of the corner cube (e.g., Figures 6 and 7) and has ignored the importance of the spatial coherence factor resulting from the source apparent size. This is expected since the great majority of source stars have a subtense significantly smaller than λ/D, where D is the diameter of the primary mirror. However, there is a small class of stars (predominately belonging to the K and M spectral class) having a sufficiently large angular subtense to be resolvable by the LST in the near UV.

The large radial shear performed by the SFS optics can be used to advantage in mapping the spatial coherence of the wavefront incident on the telescope entrance pupil. Figure 38 defines a number of points in the telescope entrance pupil. The retroreflector arm of the SFS optics maps the points in the reference beam as shown. The Porro Prism arm of the interferometer maps the points in the pupil as shown by comparison of (a) and (b). Note in these figures that the two rays incident at location I in the SFS exit pupil originate from points in the pupil that are separated by a distance somewhat less than the diameter of the reference beam as projected into the telescope entrance pupil. In the other extreme, points A and F originate from points that are separated by nearly the diameter of the telescope.

Equations (7b) and (11) are combined in a slightly simplified form,

$$I(x,y) = \text{D.C. Bias} + \Gamma(\Delta L)\ \Gamma(\xi)\ \text{Cos}\left[\varphi(x,y,t)\right] \qquad (54)$$

Where

$I(x,y)$ = Light intensity at point x,y in SFS output

$\Gamma(\Delta L)$ = Temporal coherence

$\Gamma(\xi)$ = Spatial coherence of two points separated by a distance ξ in the telescope entrance pupil.

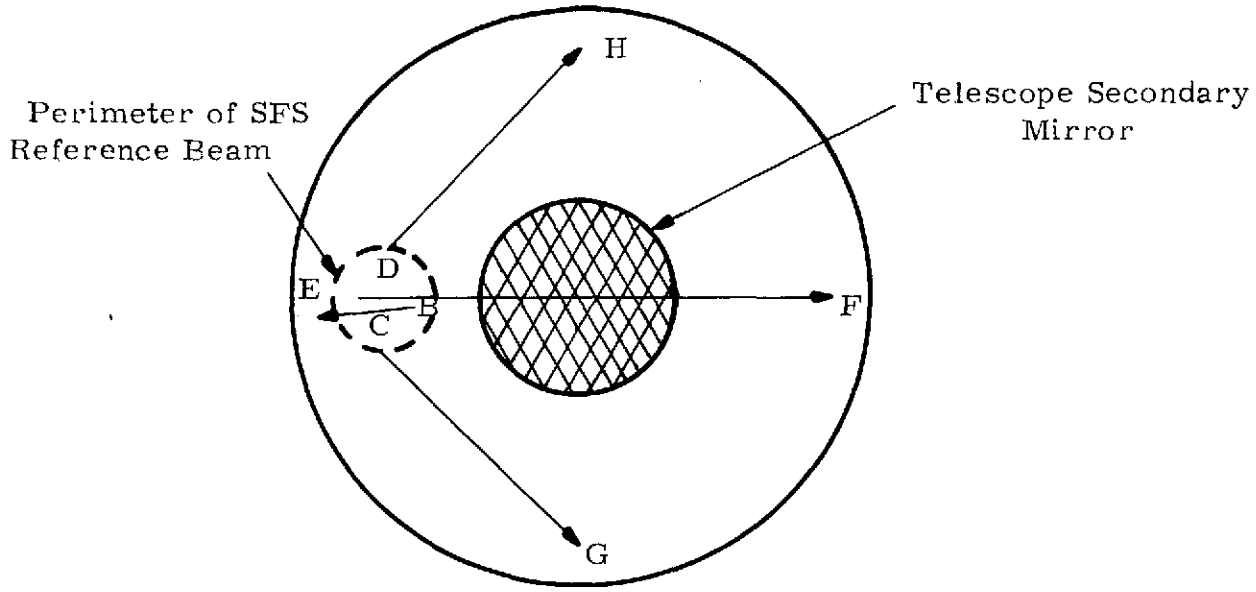

(a) Telescope Entrance Pupil

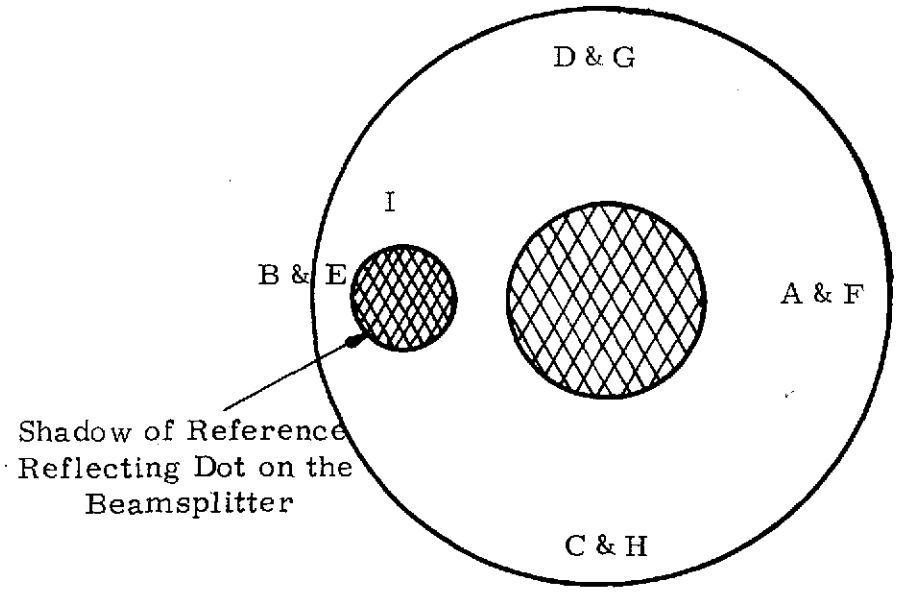

(b) SFS Exit Pupil

Figure 38. Mapping of Points During the Radial Shear Operation of the SFS

Since $\Gamma(\Delta L)$ for the given source star is constant for all points in the telescope pupil and can be easily calculated from the total system spectral response (as in Figure 4), the value of $\Gamma(\xi)$ can be determined by measuring the magnitude of the AC modulation for the signal detected at various points in the SFS output pupil. From this data we determine the spatial coherence function for two points separated by a distance of ξ in the entrance pupil.

The VanCittert-Zernike theorem states that $\Gamma(\xi)$ is related to the absolute value of the normalized Fourier transform of the intensity function of the source. Thus it is possible to use the SFS to verify the star diameters that have been previously measured by the earth-based Michelson Stellar interferometers. (Ref. 1).

Michelson (Ref. 12) and subsequent investigators were limited to measurements on only the largest stars since they used the eye as the detector. Since the eye can best measure the location where the fringe contrast disappears, all measurements of stellar diameters had a maximum resolution of approximately λ/D, where D is 50 feet and λ is a visible wavelength. However, the SFS can photometrically determine the shape of the spatial coherence function for wavelengths as short as 0.2μ and infer the location where the fringe contrast disappears. Thus, the SFS can obtain scientifically meaningful data by measuring the coherence function over a baseline of 3 meters, the entrance pupil diameter of the LST.

More importantly, it is possible to calculate any apparent variations in the luminosity across the disk of the stellar source (limb darkening) by using a more sophisticated data reduction (Ref. 13). W.I. Beavers has designed and fabricated a stellar interferometer which was attached to the Morgan Telescope at the Lowell Observatory where such an experiment was performed. The resultant interference patterns were photographed and later analyzed to determine fringe contrast. Using the SFS in a similar mode would have significant improvements over the Beaver's method:

- Elimination of atmospheric perturbations
- Measurements made directly on output signal rather than using the intermediate (and nonlinear) film medium.

- Demonstrate high SNR in detection channel in the SFS (limited only by photon noise).
- Well defined signal waveform, allowing measurment of small variations in the coherence function.

The SFS is similar to the "coherence interferometer" described by Currie, Breckinridge, and Mertz (Refs. 14, 15, and 16). In addition to performing a wavefront reversal, the SFS provides a temporal modulation of the resulting interference pattern, thus permitting a simplified linear method for measuring the fringe visibility and spatial coherence. Although Gezari (Ref. 17) obtained coherence data from analysis of the speckle pattern of the enlarged stellar image rather than from a coherence interferometer, the success of his experimental efforts encourage the use of the SFS in coherence experiments.

Harvey (Ref. 18) has recently demonstrated that similar coherence measurements can be performed on extended sources. In experiments using the sun as a source, he was able to make qualitative statements about the angular subtense of fine structure in the sun. The experiment involved placing a mask containing two diametrically opposed openings in the Kitt Peak McMath Solar Telescope and monitoring the fringe patterns in the focal plane by a procedure not unlike that of the Michelson stellar interferometer. Admittedly, the primary motivation was to negate the deleterious effect of the atmosphere. However, the technique could be easily implemented with the SFS by inserting a field stop of several resolution elements in diameter in the LST focal plane (such a stop will undoubtedly be in the final design for background noise considerations) and determining the coherence function as previously discussed.

Performing coherence measurements with the LST opens a new "dimension" to the classical measurements of astronomy. Theoretically, all measurements can be performed in the LST focal plane because of the transform relationships between the source, coherence function, and image. Further mathematical modeling is required to determine the performance of the competitive techniques in the

"real world". It is expected that the use of the very quantitative measurements permitted by the SFS optics and detection electronics can be used to advantage in these comparisons. Such coherence measurements could be used to determine the following physical effects:

- Angular diameters of stars and quasi-stellar sources
- Limb darkening
- Surface features of "point" and extended sources
- Oblateness
- Separation of binaries

9.2 FOURIER SPECTROMETER

Fourier Spectroscopy has two recognized advantages that make it an increasingly used analytical test. First, each sample of data gives information about the entire spectral scan (the Fellgett advantage). Secondly, the Fourier Spectrometer has a relatively large energy throughput or entendu, (the Jacquinot advangate). This allows the comparative source size of the interferometer to be larger than the sources for competitive dispersive type spectrometers. These advantages are effectively utilized in the IR region of the spectrum, as indicated by the choice of an IR Fourier Spectrometer in the present LST experiment package.

The optical design of the SFS satisfies all the operational requirements of a Fourier Spectrometer operating in the visible. The SFS is a dispersionless two-beam interferometer with the capability of modulating the fringe pattern by moving one mirror. In several respects, the SFS is an ideal Fourier Spectrometer since the resulting interferogram is insensitive to unwanted small tilts of corner cube as it is translated. Also, the choice of the RCA 31034 photodetectors is ideal for Fourier Spectroscopy because of their almost flat response for 1-1/2 octaves from UV to IR (Figure 4) and the photon counting capability of the photodetector.

The utility of the SFS used as a Fourier Spectrometer is not well defined. Both Albergotti and Berkey (Refs. 19 and 20) have shown that scientifically useful and accurate data may be obtained from Fourier spectrometers operating in the visible. However, the advantages that made Fourier Spectroscopy such a powerful tool in the infrared are not fully realized in the visible. Namely, the Fellgett advantage is compromised by the predominating effect of photon noise. Also, the Jacquinot advantage is affected by the added spatial coherence constraints (i.e., small apparent source size) of the SFS. This is not a serious limitation of the instrument when interrogating a "point source". The constraints for operating with an extended source can be satisfied by operating at a point in the SFS exit pupil where the spatial coherence is nearly 1 (typically point I, Figure 38), then the Jacquinot advantage can be at least partially regained. Further study is required to determine the utility of the SFS used as a Fourier Spectrometer.

9.3 IMAGE PROCESSING

Danielson has recently demonstrated that the scientific information in diffraction limited images of Uranus can be significantly increased through the use of image processing (Ref. 21). The recent successful flight of Stratoscope II obtained 48 photographs of Uranus. Of these photographs, 17 were chosen as being at best focus and subsequently subjected to image processing. Danielson computed the telescope Optical Transfer Function (OTF) by taking the discrete Fourier transform of the point spread function, thus permitting the averaging and deconvolution of the original slightly aberrated images. A resultant increase in the SNR in excess of 4 was obtained in this procedure which allowed Danielson to measure the existance of large belts on Uranus if they had a contrast of 5 percent or greater. Several simplifying assumptions as to the form of the OTF were made during the procedure (See p. 893 of referenced paper).

The availability of the SFS in the LST permits the application of a more sophisticated image processing, Figure 37 demonstrates that the residual aberration coefficients (i.e., all aberrations that can not be removed by secondary realignment) can be obtained during the processing of the SFS output

data. Using the method of H. H. Hopkins, (Ref. 22), the exact OTF of the LST can be calculated from knowledge of the aberration coefficients. The requirements of post-exposure image processing will be an important design constraint upon the figure sensor data processing.

9.4 ATMOSPHERIC EXPERIMENTS

The earth observing and ground based telescope scientific applications of the SFS, while operating in completely different environments, have similar data reduction requirements. Figure 39 shows a simplified block diagram as well as the experiment geometry for the performance of atmospheric experiments. Note that the SFS has the capability of introducing the required frequency shift by translation of the retroreflector phase detector, which is insensitive to intensity fluctuations, and by the method of comparing signals from two points in the pupil separated by a distance ξ. (See Figure 38.) The phase detector output, $\varphi(t,\xi)$ is related to the phase structure function $D_s(\xi)$ by

$$D_s(\xi) = \langle [\varphi(t,\xi)]^2 \rangle \qquad \text{(from Ref. 23)}$$

In practice, this quantity is exceedingly difficult to measure. Also, the added operational constraints placed on the LST for viewing a ground beacon all but eliminate such an experiment from the LST sceanario. The concept of the SFS used in a similar mode on an earth resources satellite or ground based telescope may very well hold merit and should be further investigated.

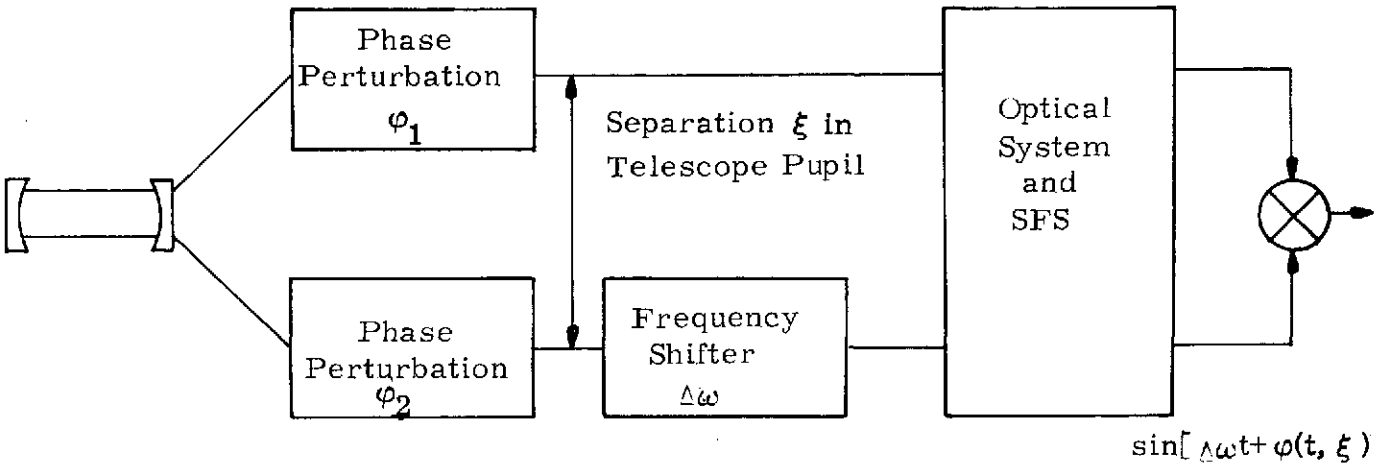

(a)

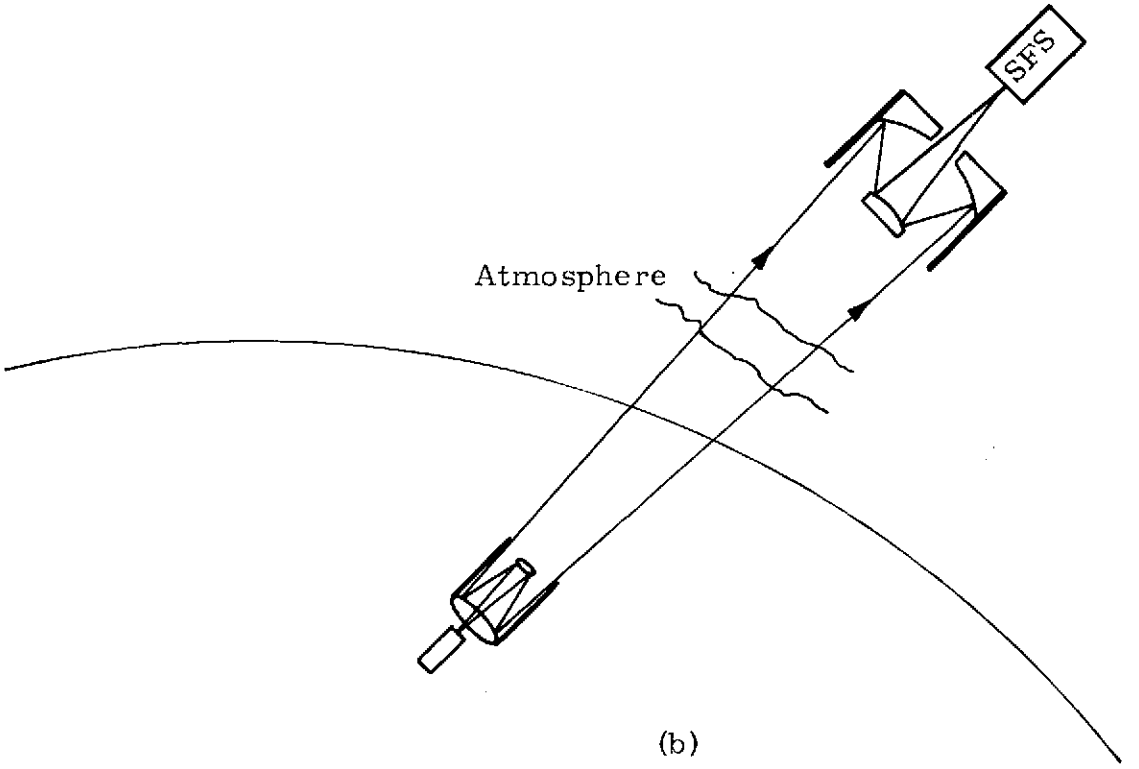

(b)

Figure 39. Atmospheric Experiment

SECTION X

CONCLUSIONS

The three objectives of the Stellar Figure Sensor (SFS) Contract are:

- Generate an analytical model of the SFS
- Design, fabricate, and test a laboratory breadboard of SFS
- Conceptual design defining the integration of the SFS into an orbiting telescope such as the LST.

All three objectives were surpassed during the contractual period. The experiments performed on the laboratory breadboard confirmed that interferometry can be performed on thermally generated light such that the Optical Path Difference Map (i.e., exact knowledge of the shape of the wavefront exiting the telescope) is typically known to within $\lambda/100$. Also, the validity of the analytical model was verified by measurements on the breadboard.

The investigations performed during the conceptual design yielded several unexpected, but engaging, capabilities of the SFS. First, the SFS output data, when operated upon by standard aberration polynomial fitting computer programs, yields the coefficients for 5 linear independent control equations for the 5 degrees of freedom for the secondary. This data processing also yields all the required information for an Active Optics Control of the primary mirror figure. Secondly, the SFS has the capability of performing several meaningful coherence oriented scientific experiments, among them measurement of stellar diameters and limb darkening, Fourier Spectroscopy, and atmospheric experiments.

To maintain the momentum of the present program as well as provide an instrument in the time scale required for the Large Space Telescope,

several activities on the present laboratory breadboard are suggested.

- The phase detection electronics should be upgraded.
- The SFS breadboard should be converted to operate in a white light mode.
- Additional experiments to confirm the analytical model and to investigate the performance of the SFS for use in Fourier Spectroscopy and coherence measurements.

The concept of a focal plane figure sensor has been proven and is awaiting its integration into the control system and scientific experiments of the LST.

REFERENCES

1. M. Born and E. Wolf. Principles of Optics. Second Rev. Edition Macmillan, 1964

2. H.J. Robertson. Development of An Active Optics Concept Using a Thin, Deformable Mirror. NASA Contract Report NASA CR-1593.

3. W.J. Bates. Proc. Phys. Soc. 59, Part 6, Series B, 1947, pg. 940. A Wavefront Shearing Interferometer.

4. F.A. Jenkins and H.F. White. Fundamental of Optics. McGraw-Hill Book Company, Third Edition, 1957, pg. 174.

5. W.H. Steel. Interferometry. Cambridge University Press, 1967, pg. 76.

6. J.B. Johnson. Phys. Rev. 32, pgs. 97-109, (1928).

7. C.H. Papas. Theory of Electromagnetic Wave Propagation. McGraw-Hill Book Company, New York (1965).

8. A.M. Mood and F.A. Graybill. Introduction to the Theory of Statistics, 2nd Ed. 1963, McGraw-Hill Book Company, pg. 86.

9. E. Roberts. A Modular Interferogram Program System. JOSA, 61 1586(A), 1971.

10. A.B. Wissinger, et al. Three Meter Telescope Study Final Report. NASA/GSFC, Contract NAS5-21540 (Aug. 1971).

11. W.B. Wetherell and M.P. Rimmer. Appl. Opt., 11, pgs. 2817-2832, General Analysis of Aplanatic Cassegrain, Gregorian and Schwarzschild Telescopes. (1972).

12. A.A. Michelson and F.G. Pease. Astrophysics J. 53, 249 (1921). Measurement of Diameter of a Orionis with the Interferometer.

13. W. Dunnweber. Zeit Fur Astrophysik 13 104, pg. 510 (1937).

14. D.G. Currie. Private Communication.

15. J.B. Breckinbridge. Appl. Opt. 11, p. 2996 (1972). Coherence Interferometer and Astronomical Applications.

16. L. Mertz. Transformations in Optics, Chapt. 4. Wiley Press, New York (1965).

17. D.Y. Gezari et al., Astrophysical Journal 173: No. 1, Part 2, Pg L1-L5 (1972). Speckle Interferometry.

18. J.W. Harvey. Nature Physical Science 235, pg. 90, (Jan. 31, 1972). Interferometry Applied to Visible Solar Features.

19. J.C. Albergotti. Amer. J. Physics 40, pg. 1070 (Aug. 1972). Fourier Transform.

20. D.K. Berkey, et al., Amer. J. Physics 40, pg. 267 (Feb. 1972). An Undergraduate Experiment in Fourier-transform Spectrometry.

21. R.E. Danielson, et al. Astrophysical Journal 178, No. 3, Part 1, pgs. 887-900 (1972). High Resolution Imagery of Uranus Obtained by Stratoscope II.

22. H.H. Hopkins. Proc. Phys. Soc. B 70, pg. 449-470 (1957). Aberration Permissible in Optical Systems.

23. R.S. Lawrence, J.W. Strohbehn. IEEE 58 10, pg. 1523 (1970). Survey of Clear Air Propagation Effects Relevant to Optical Communications.